Universidade Federal de Goiás
Instututo de Química
Programa de Pós-Graduação em Química

Mateus Rodrigues Barbosa

Development of Quantum Methods for Invisible Catalysts:

External Electric Fields and Solvation Effects in Hurd-Claisen Rearrangements

GOIÂNIA
2025

UNIVERSIDADE FEDERAL DE GOIÁS
INSTITUTO DE QUÍMICA

TERMO DE CIÊNCIA E DE AUTORIZAÇÃO (TECA) PARA DISPONIBILIZAR VERSÕES ELETRÔNICAS DE TESES

E DISSERTAÇÕES NA BIBLIOTECA DIGITAL DA UFG

Na qualidade de titular dos direitos de autor, autorizo a Universidade Federal de Goiás (UFG) a disponibilizar, gratuitamente, por meio da Biblioteca Digital de Teses e Dissertações (BDTD/UFG), regulamentada pela Resolução CEPEC nº 832/2007, sem ressarcimento dos direitos autorais, de acordo com a Lei 9.610/98, o documento conforme permissões assinaladas abaixo, para fins de leitura, impressão e/ou download, a título de divulgação da produção científica brasileira, a partir desta data.

O conteúdo das Teses e Dissertações disponibilizado na BDTD/UFG é de responsabilidade exclusiva do autor. Ao encaminhar o produto final, o autor(a) e o(a) orientador(a) firmam o compromisso de que o trabalho não contém nenhuma violação de quaisquer direitos autorais ou outro direito de terceiros.

1. Identificação do material bibliográfico

[ ] Dissertação [X] Tese [ ] Outro*:_____________

*No caso de mestrado/doutorado profissional, indique o formato do Trabalho de Conclusão de Curso, permitido no documento de área, correspondente ao programa de pós-graduação, orientado pela legislação vigente da CAPES.

Exemplos: Estudo de caso ou Revisão sistemática ou outros formatos.

2. Nome completo do autor

Mateus Rodrigues Barbosa

3. Título do trabalho

Development of Quantum Methods for Invisible Catalysts: External Electric Fields and Solvation Effects in Hurd-Claisen Rearrangements

4. Informações de acesso ao documento (este campo deve ser preenchido pelo orientador)

Concorda com a liberação total do documento [X] SIM [ ] NÃO[1]

[1] Neste caso o documento será embargado por até um ano a partir da data de defesa. Após esse período, a possível disponibilização ocorrerá apenas mediante:
a) consulta ao(à) autor(a) e ao(à) orientador(a);
b) novo Termo de Ciência e de Autorização (TECA) assinado e inserido no arquivo da tese ou dissertação.
O documento não será disponibilizado durante o período de embargo.
Casos de embargo:
- Solicitação de registro de patente;
- Submissão de artigo em revista científica;
- Publicação como capítulo de livro;
- Publicação da dissertação/tese em livro.

Obs. Este termo deverá ser assinado no SEI pelo orientador e pelo autor.

Documento assinado eletronicamente por **Heibbe Cristhian Benedito De Oliveira**, **Professor do Magistério Superior**, em 27/07/2025, às 21:52, conforme horário oficial de Brasília, com fundamento no § 3º do art. 4º do Decreto nº 10.543, de 13 de novembro de 2020 .

Documento assinado eletronicamente por **Mateus Rodrigues Barbosa**, **Discente**, em 28/07/2025, às 12:35, conforme horário oficial de Brasília, com fundamento no § 3º do art. 4º do Decreto nº 10.543, de 13 de novembro de 2020.

A autenticidade deste documento pode ser conferida no site https://sei.ufg.br/sei/controlador_externo.php?acao=documento_conferir&id_orgao_acesso_externo=0, informando o código verificador **5506495** e o código CRC **5D7FAF1D**.

Mateus Rodrigues Barbosa

Desenvolvimento de Métodos Quânticos para Catalisadores Invisíveis

Campos Elétricos Externos e Efeitos de Solvatação nas Rearranjos de Hurd–Claisen

Thesis presented to the Postgraduate Program in Chemistry (PPGQ) at the Institute of Chemistry (IQ) of the Federal University of Goiás (UFG) as a requirement for the qualification examination.
Field of study: Chemistry.
Research line: Computational Chemistry

Advisor: Prof. PhD. Heibbe Cristhian Benedito de Oliveira

GOIÂNIA
2025

Ficha de identificação da obra elaborada pelo autor, através do
Programa de Geração Automática do Sistema de Bibliotecas da UFG.

Rodrigues Barbosa, Mateus
Development of Quantum Methods for Invisible Catalysts: [manuscrito] : External Electric Fields and Solvation Effects in Hurd Claisen Rearrangements / Mateus Rodrigues Barbosa. - 2025.
xix, 123 f.: il.

Orientador: Prof. Dr. Heibbe Cristhian B. de Oliveira.
Tese (Doutorado) - Universidade Federal de Goiás, Instituto de Química (IQ), Programa de Pós-Graduação em Química, Goiânia, 2025.
Bibliografia. Apêndice.
Inclui abreviaturas, gráfico, tabelas, algoritmos, lista de figuras, lista de tabelas.

1. Oriented Electric Field. 2. Hurd-Claisen. 3. Transition State. 4. S QM/MM. 5. MoleKing. I. Cristhian B. de Oliveira, Heibbe, orient. II. Título.

CDU 54

UNIVERSIDADE FEDERAL DE GOIÁS

INSTITUTO DE QUÍMICA

ATA DE DEFESA DE TESE

Ata Nº **198** da sessão de Defesa de Tese de **Mateus Rodrigues Barbosa** que confere o título de **Doutor em Química**, na área de concentração em **Química.**

Aos **nove dias do mês de julho de dois mil e vinte e cinco**, a partir das **14h:00m**, por **Videoconferência**, realizou-se a sessão pública de Defesa de Tese intitulada ***"Development of Quantum Methods for Invisible Catalysts: External Electric Fields and Solvation Effects in Hurd-Claisen Rearrangements"***. Os trabalhos foram instalados pelo Orientador, Professor Doutor **Heibbe Cristhian Benedito de Oliveira (IQ – UFG)** com a participação dos demais membros da Banca Examinadora: Professora Doutora **Lilian Tatiane Ferreira de Melo Camargo (IFG - Anápolis)**; Professor Doutor **Martin Schwellberger Barbosa (IQ – UFG)**, Professor Doutor **Renato Borges Pontes (IF – UFG)**, Professor Doutor **Leonardo Giordano Paterno (IQ - UNB)**. Durante a arguição, os membros da banca não fizeram sugestão de alteração do título do **trabalho**. A Banca Examinadora reuniu-se em sessão secreta a fim de concluir o julgamento da Tese, tendo sido o candidato aprovado pelos seus membros. Proclamados os resultados pelo Professor Doutor **Heibbe Cristhian Benedito de Oliveira**, Presidente da Banca Examinadora, foram encerrados os trabalhos e, para constar, lavrou-se a presente ata que é assinada pelos Membros da Banca Examinadora, aos **nove dias do mês de julho de dois mil e vinte e cinco.**

TÍTULO SUGERIDO PELA BANCA

Documento assinado eletronicamente por **Heibbe Cristhian Benedito De Oliveira**, **Professor do Magistério Superior**, em 14/07/2025, às 10:48, conforme horário oficial de Brasília, com fundamento no § 3º do art. 4º do Decreto nº 10.543, de 13 de novembro de 2020 .

Documento assinado eletronicamente por **Martin Schwellberger Barbosa**, **Professor do Magistério Superior**, em 14/07/2025, às 16:25, conforme horário oficial de Brasília, com fundamento no § 3º do art. 4º do Decreto nº 10.543, de 13 de novembro de 2020 .

Documento assinado eletronicamente por **Leonardo Giordano Paterno**, **Usuário Externo**, em 15/07/2025, às 09:41, conforme horário oficial de Brasília, com fundamento no § 3º do art. 4º do Decreto nº 10.543, de 13 de novembro de 2020 .

Documento assinado eletronicamente por **Lilian Tatiane Ferreira de Melo Camargo**, **Usuário Externo**, em 15/07/2025, às 15:25, conforme horário oficial de Brasília, com fundamento no § 3º do art. 4º do Decreto nº 10.543, de 13 de novembro de 2020 .

Documento assinado eletronicamente por **Renato Borges Pontes**, **Professor do Magistério Superior**, em 16/07/2025, às 10:21, conforme horário oficial de Brasília, com fundamento no § 3º do art. 4º do Decreto nº 10.543, de 13 de novembro de 2020 .

A autenticidade deste documento pode ser conferida no site https://sei.ufg.br/sei/controlador_externo.php?acao=documento_conferir&id_orgao_acesso_externo=0, informando o código verificador **5452685** e o código CRC **D2A2D30B**.

“ *All that is gold does not*
glitter, not all those who
wander are lost.”

J.R.R. Tolkien

Acknowledgements

First and foremost, I would like not only to express my gratitude but also to dedicate this work to my parents, Roni Darros Barbosa and Leticia Lofego Rodrigues, whose unwavering support and encouragement have been the foundation of my academic journey. Their belief in my potential has been a constant source of motivation.

I also extend my heartfelt thanks to my family—my brothers, sister, and grandparents—who have always stood by me, offering love and support throughout my life. To my friends, from childhood to university, thank you for the laughter, joy, and companionship. And to my colleagues, who have shared this journey with me: I am certain that this work would not have been possible without your support and collaboration.

Next, I can express nothing but deep gratitude to my advisor, Professor Heibbe Cristhian Benedito de Oliveira, who has guided me throughout my entire academic path. Your mentorship, patience, and expertise have been invaluable in shaping both my research and my personal growth as a scientist.

Finally, I acknowledge the support of the *Fundação de Amparo à Pesquisa do Estado de Goiás* (FAPEG) and all those at the *Universidade Federal de Goiás* (UFG) who have made this project possible.

I know that a simple “thank you” is not enough to fully express my appreciation, but I hope this work serves as a small token of gratitude for all the support and encouragement I have received throughout my life.

Resumo

Este trabalho apresenta o desenvolvimento de protocolos computacionais para investigar os efeitos catalíticos de campos elétricos externos orientados e da solvatação no rearranjo de Hurd-Claisen. O estudo integra cálculos de teoria do funcional da densidade com simulações de Mecânica Quântica / Mecânica Molecular Sequencial, incorporando a aproximação da configuração eletrostática média do solvente juntamente com a aproximação do gradiente de energia livre. Esses protocolos computacionais permitem modelar com precisão as interações com o solvente e as perturbações induzidas por campos elétricos, fornecendo elucidações sobre a cinética da reação e a estereosseletividade. Uma inovação fundamental desta pesquisa é o módulo Python *MoleKing*, desenvolvido para automatizar fluxos de trabalho computacionais, incluindo manipulação de geometria molecular, rotação e alinhamento com campos elétricos. Escrito em C++, o *MoleKing* simplifica a preparação de cálculos de química quântica ao reorientar automaticamente as moléculas ao longo dos eixos da reação ou moleculares, facilitando a aplicação eficiente dos campos elétricos. Além disso, o módulo lida com a leitura e a geração de arquivos de entrada/saída para softwares como *Gaussian* e *PSI4*, reduzindo significativamente a intervenção manual e a ocorrência de erros computacionais. A metodologia desenvolvida foi aplicada a uma série de rearranjos de Hurd-Claisen com diferentes substituintes, dada a conhecida sensibilidade desse rearranjo a interações de caráter eletrostático, avaliando-se sistematicamente a influência de campos elétricos externos orientados ao longo do eixo da reação e do eixo molecular. Os efeitos da solvatação foram modelados utilizando etil-vinil eter dentro da Mecânica Quântica / Mecânica Molecular Sequencial, revelando a interação entre o solvente e os campos externos na modulação dos momentos de dipolo e das propriedades geométricas do estado de transição. As simulações computacionais demonstram que campos externos podem alterar significativamente a estereosseletividade ao estabilizar seletivamente estados de transição específicos, enquanto a solvatação introduz efeitos de polarização não negligenciáveis que influenciam as barreiras de ativação. Esses achados destacam o potencial da catálise invisível como uma ferramenta precisa para o controle estereoquímico.

Palavras-chave: Campo Elétrico Orientado, Hurd-Claisen, S-QM/MM, Estado de Transição, Estereosseletividade, MoleKing

Abstract

This work presents the development of computational protocols to investigate the catalytic effects of oriented external electric fields and solvation on the Hurd-Claisen rearrangement. The study integrates density functional theory calculations with sequential Quantum Mechanics / Molecular Mechanics simulations, incorporating the average electrostatic configuration approximation of the solvent together with the free energy gradient approximation. These computational protocols allow for accurate modeling of solvent interactions and field-induced perturbations, providing insights into reaction kinetics and stereoselectivity. A key innovation of this research is the Python module *MoleKing*, developed to automate computational workflows, including molecular geometry manipulation, rotation, and alignment with electric fields. Written in C++, *MoleKing* streamlines the preparation of quantum chemical calculations by automatically reorienting molecules along the reaction or molecular axes, facilitating the efficient application of electric fields. Furthermore, the module handles input/output file processing for software such as *Gaussian* and *PSI4*, significantly reducing manual intervention and computational errors. The developed methodology was applied to a series of Hurd-Claisen rearrangements with different substituents, given the well-known sensitivity of this reaction to electrostatic interactions, systematically evaluating the influence of oriented external electric fields along the reaction and molecular axes. Solvation effects were modeled using ethyl vinyl ether within the Quantum Mechanics / Molecular Mechanics Sequential framework, revealing the interaction between the solvent and external fields in modulating dipole moments and transition state geometries. Computational simulations demonstrate that external fields can significantly alter stereoselectivity by selectively stabilizing specific transition states, while solvation introduces non-negligible polarization effects that influence activation barriers. These findings highlight the potential of invisible catalysis as a precise tool for stereochemical control.

Keywords: Oriented Electric Field, Hurd-Claisen, Transition State, S-QM/MM, Stereoselectivity, MoleKing

Contents

List of Figures

List of Tables

List of Abbreviations

STM	**S**caning **T**unneling **M**icroscopy
MBH	**M**orita-**B**aylis-**H**ilmamn
TS	**T**ransition **S**tate
TST	**T**ransition **S**tate **T**heory
OEEF	**O**riented **E**xternal **E**lectric **F**ield
PCM	**P**olarizable **C**ontinum **M**odel
QM/MM	**Q**uantum **M**echamics/**M**olecular **M**echamics
S-QM/MM	**S**equantial-**Q**uantum **M**echamics/**M**olecular **M**echamics
ASEC	**A**verage **S**olvent **E**lectrostatic **C**onfiguration
FEG	**F**ree **E**nergy **G**radient
PES	**P**otential **E**nergy **S**urface
DFT	**D**ensity **F**unctional **T**heory
HF	**H**artree **F**ock
MP	**M**øller-**P**lesset
HK	**H**ohenberg-**K**ohn
KS	**K**ohn-**S**ham
LDA	**L**ocal **D**ensity **A**pproximation
GGA	**G**eneralized **G**radient **A**pproximation
MC	**M**onte-**C**arlo
PCA	**P**rincipal **C**omponent **A**nalysis
MK	**M**erz-**K**ollman
EVE	**E**thyl-**V**enyl **E**ther
OEEF	**O**riented **E**xternal **E**lectric **F**ield
EEF	**E**xternal **E**lectric **F**ield
IRC	**I**nternal **R**eaction **C**oordinate
ax	**ax**ial
eq	**eq**uatorial
a.u.	**a**tomic **u**nits
EWG	**E**lectron **W**ithdrawing **G**roup
EDG	**E**lectron **D**onating **G**roup

Chapter 1

Introduction

The development or improvement of catalysts is of recognized importance in chemical reactivity, since these systems are capable of binding to reactive molecular units, thereby reducing the energetic activation barrier that triggers chemical transformations. A direct consequence of this is the acceleration of chemical processes, without being consumed in the process of these the resulting transformation. Currently, this effect can be achieved in a myriad of distinct ways, the most widely disseminated being the use of catalysts with different levels of molecular complexity, having chemical elements as catalytic centers, such as transition metals of high abundance,[1–3] precious metals,[4,5] rare earth elements,[6–8] or even alkali metals.[9]

A relatively old idea in physics and theoretical chemistry, inspired by fundamental concepts from classical electrodynamics, is the use of external electric fields to rationally manipulate the synthesis of chemical compounds.[10] Many reagents employed in organic and inorganic synthesis exhibit a permanent dipole moment at different stages of the reaction pathway—reactants, transition states, and products—whose relative energies can be altered in the presence of an external electric field. Depending on the orientation of the field, this interaction can generate stabilizing or destabilizing forces, enabling controlled formation of reactive species throughout the reaction.

In recent years, experimental advances have successfully translated these theoretical ideas into practice.[11] For instance, Aragonés and collaborators[12] utilized scanning tunneling microscopy (STM) to catalyze the classical Diels–Alder reaction between a norbornene derivative immobilized on a gold surface and a furan molecule attached to the STM probe tip. Their experimental results aligned with quantum mechanical predictions regarding the influence of external electric fields on the reaction.

However, a major limitation arises when scaling this approach to bulk synthesis.[10] One proposed strategy to address this challenge involves controlling electric fields using parallel charged plates covered with an insulating film.[13,14] When combined with flow chemistry techniques, this method can effectively scale the catalytic process.[10] These findings have reinforced the potential of electric fields to modulate activation energy barriers, solidifying their role in “invisible catalysis” as a promising alternative to metal-centered catalysis. This approach is sometimes referred to as “electrocatalysis” due to the role of electric fields in modulating reactivity.[10,11,15] However, this differs from the conventional electrochemical use of the term, which typically involves redox processes at electrodes.

Another point to highlight is the use of “invisible catalysis” as a means of controlling stereoselectivity. For example, the investigation by Wang and collaborators,[16] studied the enantio- and stereoselectivity of a series of Diels-Alder reactions between cyclopentadiene and a variety of dienophiles under the influence of an external electric field (see Figure 1.1). In Figure 1.1, one of the results obtained is presented, where the application of an electric field with a magnitude of 5.00×10^{-3}a.u. (atomic units) in appropriate orientations generates differentiation in the degenerate kinetic profile of the reaction. Even more important is that if the electric field is reversed, this is sufficient for the R pathway (blue in Figure 1.1) to be preferred over the S pathway (red in Figure 1.1); that is, enantioselectivity can be manipulated relatively easily using external electric fields.[16]

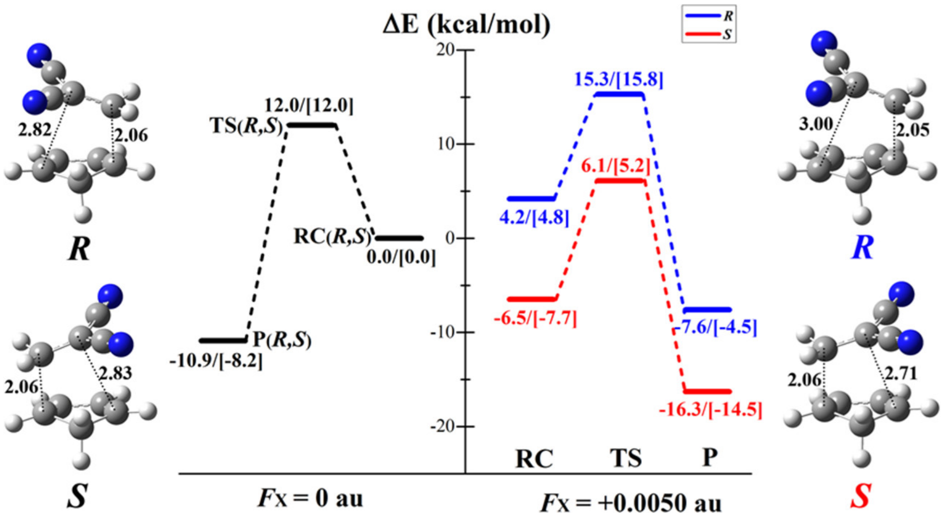

Figure 1.1: Effect of the application of an external electric field on the energy barriers of Diels-Alder cycloadditions calculated by Wang and collaborators.[16] The Field was perpendicularly aligned with the reaction axis, with a magnitude of 5.00×10^{-3} a.u. The blue and red lines represent the R and S pathways, respectively.

Competitive chemical reactions, particularly those involving stereoselective differentiation between reaction products, can greatly benefit from control via externally oriented electric fields. Such fields not only alter conversion rates but also direct the preferential formation of specific stereoisomers. A notable example of a reaction fitting this scope is the work by Silva and collaborators, who recently investigated a transvinylation reaction catalyzed by mercury(II) acetate, followed by a Hurd-Claisen rearrangement of Morita-Baylis-Hillman

(MBH) adducts derived from alkyl acrylates.[17] Their experimental results indicated an inversion of stereoselectivity compared to models established in the literature.

The most widely accepted model for stereoisomeric control in this class of reactions is based on the transition state (TS) proposal by Basavaiah and collaborators (see Figure 1.2).[18] According to Basavaiah's model, the favored product is the one in which steric repulsions are minimized in the TS step. Specifically, steric interactions between the substituent R and the methoxycarbonyl fragment (R_1O_2C- in Figure 1.2) dictate the diastereoselectivity of this rearrangement.

For example, between an alkyl substituent (metil, CH_3) and an aryl substituent (phenyl, Ph), the trend follows Basavaiah's model, with the E isomer being predominantly favored when $R = CH_3$. However, in the presence of bulkier aryl groups such as pNO_2Ph, the two isomers become more competitive, leading to a prominent decrease in the E/Z ratio. This deviation cannot be fully explained by Basavaiah's steric model alone. To address this unexpected behavior, Silva and collaborators conducted a detailed investigation using first-principles theoretical calculations to elucidate the underlying mechanistic factors.

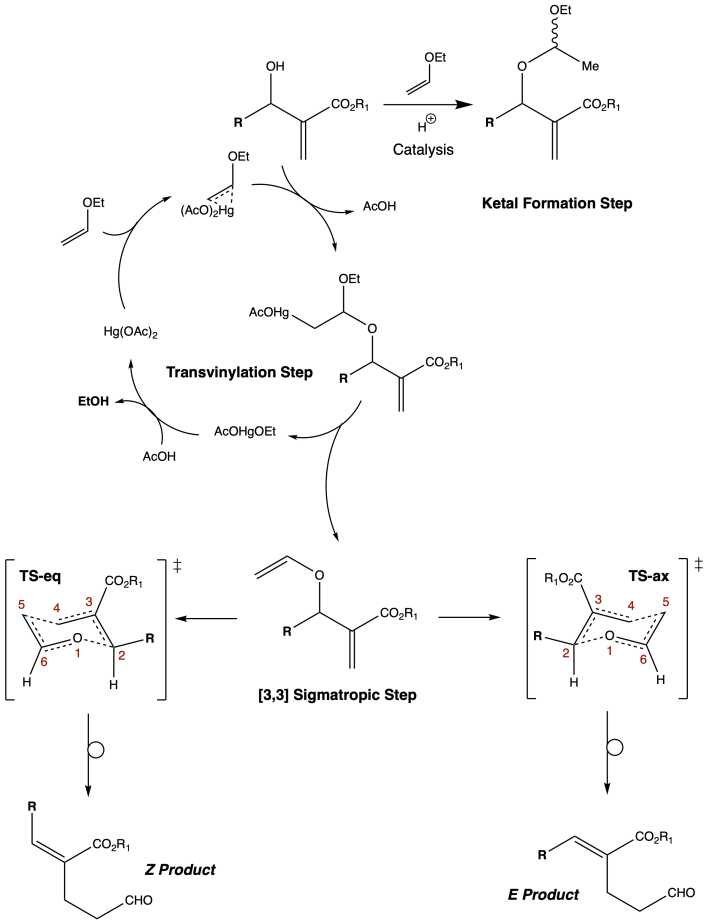

Figure 1.2: Proposed transition state for the Hurd-Claisen rearrangement studied by Silva and collaborators[17], and proportions of the E and Z diastereoisomers as a function of the substituent. Extracted from[17]. Substituent $R = CH_3$, Ph, and pNO_2Ph, with experimental E/Z ratios of 3:1, 24:1, and 6:1, respectively.

Oliveira and collaborators further extended this study by applying the Shubin energy decomposition method to a series of Hurd-Claisen rearrangements, focusing on the influence of two electron-withdrawing groups and eight diverse substituents (CH_3, Et, s-Prop, t-Bu, i-Bu, NH_2Ph, NO_2Ph, Ph).[19] By applying Principal Component Analysis (PCA) to the energy decomposition results, the authors were able to identify that steric and quantum effects exhibit a strong inverse relationship, making electrostatic forces the main factor behind the differentiation of the stereoisomers. The studies also highlighted additional influential factors within the central structure of the transition state, mainly the difference in the dipole moments of the central group in both stereoisomers.[19,20]. These electrostatic effects indicate that this class of reactions can be carried out with the assistance of external electric fields to achieve full control over the possible diastereoisomers of this reaction.

Considering that chemical reactions are often carried out in the presence of solvents, they can act as a medium that assists the activation complexes, possibly creating a solvation effect that stabilizes the dipole in the transition state geometry, which is intrinsically connected to the stabilization achieved by the interaction with oriented electric fields[21], potentially further reducing the activation energy barrier of the reaction. Zhang and collaborators[22] demonstrated in a theoretical study that this is exactly the case in hydroboration reactions of aldehydes and ketones, where not only the external electric field is capable of lowering the activation energy of the reactions, but the presence of solvation effects also plays a non-negligible role in such reactions. However, the solvent treatment generally employed in theoretical studies on catalysis via oriented electric fields uses Polarizable Continuum Models (PCM),[16,22] which, although intrinsically valuable as a preliminary low-cost computational estimate, are not capable of including atomistic effects that play an important role in the solution.

This effect, originating from the chemical environment—specifically solvatochromic effects—modifies the interaction between the molecule and the electric field. The dielectric medium can either attenuate or amplify the polarization induced by the external field while also promoting the solvent screening effect. In this phenomenon, the external electric field induces the alignment of solvent molecules, thereby reducing the total oriented external electric field (OEEF) magnitude experienced by the central molecule.[23] The presence of multiple dipole moments from solvent molecules leads to variations in the partial charges of the solute atoms and, consequently, alters its electrical properties.

The sequential QM/MM solvation methodology proposed by Kaline Coutinho and collaborators in 1997,[24,25] along with the ASEC (Average Solvent Electrostatic Configuration) approximation,[26,27] provides low-cost computational alternatives for studying the effects arising from such dipole moments while incorporating some atomistic interactions, primarily those stemming from Coulombic forces.

By applying the Free Energy Gradient approximation,[28,29] this study aims to develop a computational protocol for investigating solvation effects on the activation complex structure of organic reactions. The perturbation of the one-electron integrals in the Hamiltonian can be used to emulate solvent effects in the presence of oriented electric fields, ultimately aiding in the understanding of solvent influence on catalytic processes mediated by OEEFs (oriented external electric fields).

Given that electric-field-based catalysis at preparative scales may be enabled by flow

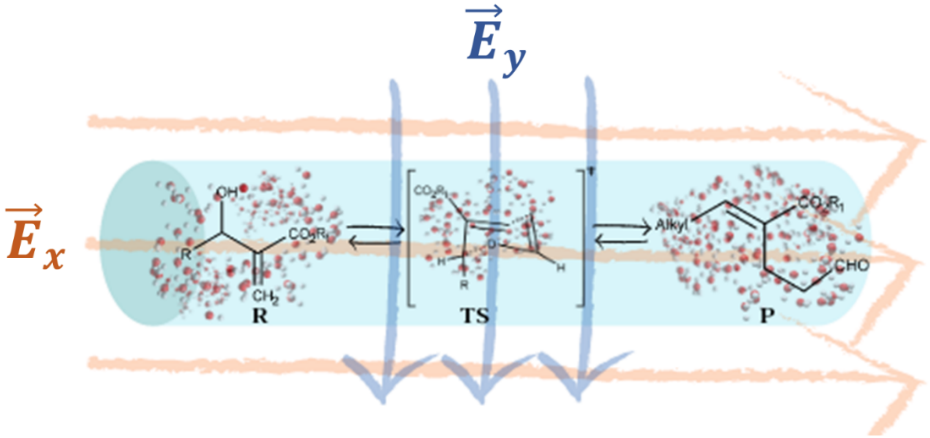

Figure 1.3: Proposed model for the simultaneous treatment of oriented external electric fields and solvation effects in the study of organic reactions.

chemistry—where solvent choice plays a crucial role—we developed a model that simultaneously accounts for oriented external electric fields and solvation effects under these conditions, as shown in Figure 1.3.

Since applying electric fields in large-scale synthesis may rely on solvent-dependent flow chemistry techniques, this work developed a systematic model that includes both OEEF and solvent effects to capture the full influence of external conditions on reaction stereochemistry, as shown in Figure 1.3. With the S-QM/MM treatment of the solvent, quantum mechanical calculations in the presence of electric fields in various orientations are able to capture the anisotropic orientational effects of the field in the liquid phase, as this model accounts for the rotational mobility of the solute. In this way, the external electric field will act as a filter along the reaction pathway, favoring either the E or Z product by increasing or decreasing the energy of these stereoisomers.

As stated by Shaik, the experimental study of oriented external electric fields in mechanistic interpretation should be accompanied by quantum chemical calculations,[15] in order to avoid potential pitfalls. Moreover, the experimental application of OEEFs presents significant challenges, particularly in achieving precise field orientation, as evidenced by previous studies[10,12,15], especially when coupled with the solvent perturbation[23]. This raises two key questions: Given the pronounced electrostatic sensitivity of the Hurd-Claisen rearrangement, could a non-oriented external electric field effectively influence the stereoselectivity of reactions, thereby circumventing the need for strict field alignment? And, can the well established gold thiolate model[12,30] be adapted to the Hurd-Claisen rearrangement, allowing for the application of oriented external electric fields in a more practical manner?

Chapter 2

Objectives

- Investigate the influence of solvent effects (included through the S-QM/MM - ASEC-FEG methodology) and the presence of an oriented external electric field acting as an "invisible catalyst" on organic reactions. As a case study, and based on the known sensitivity of the Hurd-Claisen rearrangement to electrostatic interactions[19], the protocol was implemented for the rearrangement described by Silva et al.[17], aiming to understand changes in stereoselectivity resulting from geometric and electronic modifications in the transition state structure induced by interactions with solvent molecules and the external electric field.

    1. Determine the reaction axis, following the reaction axis rule, as well as the transition state structures of various Hurd-Claisen rearrangements under an OEEF with varying field strengths.
    2. Apply principal component analysis to identify the molecular axis and evaluate the influence of the OEEF when applied parallel and perpendicular to this axis.
    3. Develop a Python version of *DicePlayer*, originally created by Georg and collaborators,[31] aiming to port all functionalities of the original program to Python 3, including support for electric field simulations and transition state analysis.
    4. Study the influence of ethyl vinyl ether on the geometric and electronic properties of the transition state structure of the Hurd-Claisen rearrangement proposed by Silva and collaborators, using the S-QM/MM - ASEC-FEG methodology.
    5. Investigate the combined effect of the OEEF and the presence of ethyl vinyl ether on the geometric and electronic properties of the transition state structure of the Hurd-Claisen rearrangement proposed by Silva and collaborators, using a combination of the aforementioned methodologies.

- Develop a module for the Python 3 programming language, written in C++, capable of performing rotation, translation, and modification operations on the geometric parameters of a new computational variable type called *Molecule*, designed to represent molecular structures in a Cartesian coordinate system.

1. Implement this module in the Python-based version of the *DicePlayer* software.
2. Add parsing and writing functions to the module, enabling integration with the Gaussian software used to perform quantum mechanical calculations.
3. Extend the module to include full support for point charges and external electric fields, allowing it to handle external perturbations in the context of molecular simulations.

- Building upon the preceding objectives, carry out systematic studies with the aim of formulating experimentally accessible protocols for probing the influence of electric fields on organic reaction mechanisms, thereby contributing to the development of more practical and reproducible approaches for electric field-assisted catalysis.

Chapter 3

Theoretical Fundamentals

This section presents an overview of the main theories addressed in this study. Initially, the focus will be on Transition State Theory, which forms the fundamental basis for the chemical kinetics calculations. This will be followed by a discussion on Density Functional Theory, as it underpins the theoretical calculations performed in this work. To evaluate the effect of the chemical environment on transition state geometries, as well as its impact on stereoselectivity, the two subsequent sections will address S-QM/MM and the role of oriented electric fields in chemistry. The latter is the central focus of this dissertation, as it serves as the primary tool for assessing the application of 'invisible catalysis' in the Hurd-Claisen rearrangement.

3.1 Transition State Theory

In chemistry, one of the most sought-after questions is how a reaction takes place.[32] The goal of studying reaction mechanisms is to provide a detailed description of the process that leads from reactants to products. This includes a comprehensive characterization of the composition, structure, and energy changes involved, consistent with the reaction stoichiometry, electronic motions, and reaction rates[33]. The study of reaction mechanisms is a fundamental part of chemistry and is essential for understanding the chemical processes that occur in nature.

Computational studies play a key role in understanding reaction mechanisms by enabling the characterization of energy profiles and electronic motions that are often inaccessible through experimental methods[17,19,34]. The analysis of reaction kinetics provides the most informative insights for delineating a reaction mechanism. However, knowledge of the stability of the initial and final stages of a chemical transformation, as provided by thermodynamics, should not be overlooked. In this light, a complete study of a reaction mechanism should include both the thermodynamics and the kinetics of the process[35,36]. The transition State Theory (TST) is a powerful tool for studying the kinetics of chemical reactions, providing a theoretical framework for understanding the rates reactions from a thermodynamic perspective[33].

TST was first introduced by Eyring, in the characterization of the saddle points of the potential energy surface (PES) of the $H_2 + H$ reaction. The theory was later developed by Wigner[37], Polanyi, and Evans[38], and has since become a cornerstone of chemical kinetics. TST is based on the concept of a transition state (TS), which is a hypothetical structure that represents the highest energy point along the reaction coordinate[36]. The TS is a saddle point on the PES, where the reaction is neither in the reactant nor in the product state, but in a state of transition between the two. The rate of a reaction is determined by the energy barrier that must be overcome to reach the transition state, which is known as the activation energy.

Assuming a generic chemical reaction, $AB + C \rightleftharpoons A + BC$, in which an $A - B$ bond is broken in favor of a $B - C$ bond. From an energetic standpoint, both the initial and final stages of this reaction are stable molecular organizations, represented as valleys in a PES. Figure 3.1, adapted from[35], presents a representation of the PES containing this reaction. From a quantum standpoint, the breaking of the $A - B$ bond represents the gradual increase in the distance between the two groups, while the $B - C$ bond is formed, meaning that the B group gradually approaches the C group. For this to happen, the system's overall conformation needs to pass through a higher energy state.

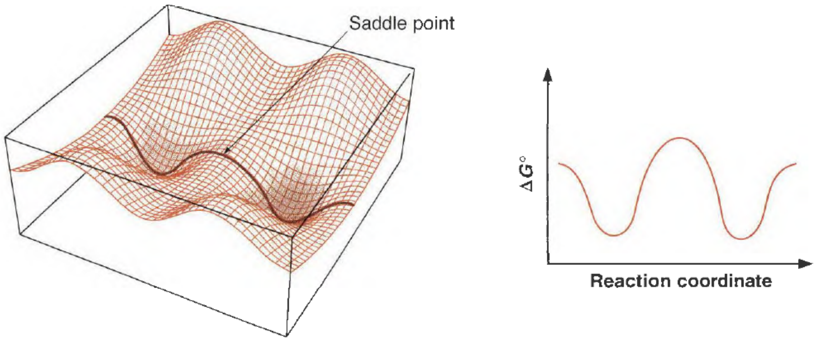

Figure 3.1: Representation of the potential energy surface of the hypotetical reaction $AB + C \rightleftharpoons A + BC$.[35]

Among all the higher energy points that conect the reactants and products, the saddle point corresponds to the one with the lowest increase in energy, hance the most probable path for the reaction to take place. This saddle point connecting both sides of the trasformation is the transition state.[35] The TS is a structure that is not stable, as it is a point of inflection in the PES, where the forces acting on the system are null. Thus, according to TST, the generic reaction previously mentioned can be described as a sequence of steps in which the reactants,

$AB+C$, reach the TS, and then the products, $A+BC$, are formed.

$$AB + C \rightleftharpoons ABC^{\ddagger} \rightarrow A + BC \tag{3.1}$$

The ‡ therm represents the saddle point structure. A good note on the workings of TST is that an average reaction in a system containing N atoms will have $3N-6$ vibrational modes for non-linear molecules. In order to describe this system's PES, we would need one axis for the energy and $3N$ axes for the degrees of freedom of each atom. This kind of surface is called a hypersurface. Additionally, the increase in vibrational modes in complex systems leads to an exponential increase in the number of possible states, not all of which are minimum energy states. Therefore, the properties evaluated by TST need to be weighted by the partition function of the system.[36] From here on, the discussion will focus on the minimum energy path, which is the path that connects the reactants and products through the TS—the reaction coordinate.

The rate at which a reaction takes place is proportional to the concentration of its reactants. Therefore, in TST, the rate of product formation for our hypothetical reaction is given by the equation:

$$\frac{d[CB]}{dt} = k^{\ddagger}[ABC^{\ddagger}] = k^{\ddagger}K^{\ddagger}[AB][C] = k[AB][C], \tag{3.2}$$

Thus, the rate constant k is given by the product of the rate constant $k^{\ddagger}$ of the transition state (TS) and the equilibrium constant $K^{\ddagger}$. Knowing that, in TST, the reaction is driven by vibrations[35,36], we can state that the rate constant of a TS-mediated reaction is proportional to the vibrational frequency that facilitates the conversion of the activated complex into products, expressed as:

$$k^{\ddagger} = \kappa\nu. \tag{3.3}$$

Where κ measures the frequency in which such vibrations happen. This propose the fact that the lifetime of a activation complex is in the order of a vibration period. To better describe such a short live phenomena we applied a statistical mechanics analisys, defining a new way top describe the rate constant, as:

$$k = \kappa\frac{k_B T}{h}e^{-\frac{\Delta G^{\ddagger}}{RT}} \tag{3.4}$$

where k_B is the Boltzmann constant, T is the temperature, h is the Planck constant, R is the ideal gas constant, and $\Delta G^{\ddagger}$ is the Gibbs free energy of activation, figure 3.2.[35,36] By applying the definition of ΔG it is possible the rearranged equation 3.4 as:

$$k = \kappa \frac{k_B T}{h} e^{\frac{\Delta S^{\ddagger}}{R}} e^{-\frac{\Delta H^{\ddagger}}{RT}}. \tag{3.5}$$

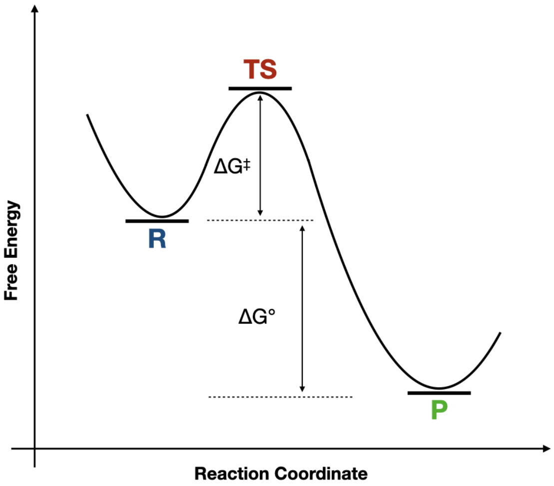

Figure 3.2: Reaction path for the hypotetical reaction $AB + C \rightleftharpoons A + BC$.[35]

3.1.1 TST in Stereocontrol

The stereoselectivity of chemical reactions refers to the tendency of a reactive process to produce stereisomeric products in a preferential manner, such as the $(E)-$ or $(Z)-$alkenes[20]. In chemistry the mechanisms behind the stereocontrol of a reaction are of great importance, as they can be used to predict the outcome of a reaction, and even to design new reactions. Stereoisomers are characterized by the spatial arrangement of their atoms, and can be divided into two main groups: enantiomers and diastereomers. Enantiomers are non-superimposable mirror images of each other, while diastereomers are stereoisomers that are not mirror images of each other. TST can used in studies of stereocontrol to predict the stereochemistry of a reaction, by analyzing the energy barrier that must be overcome to reach the desired TS.

On a energetic stand point, the stereoselectivity of a reaction can be determined by thermodinamic control, the overall stability of the final produc, and kinetic control, the overall stability of the transition state geometry[20]. In the case of a reaction that produces two stereoisomers, the stereoselectivity can be determined by the energy difference between the two TSs or by the energetic gain in product stability. Figure 3.3 represents the reaction path a hypothetical reaction that produces two stereoisomers, A and B.

In general, the faster-formed product will be the preferred one, especially in reactions with a high energy barrier. This is due to the fact that the TS leading to the faster product is more stable and, therefore, more likely to be formed[19,20,39]. The Curtin-Hammett principle

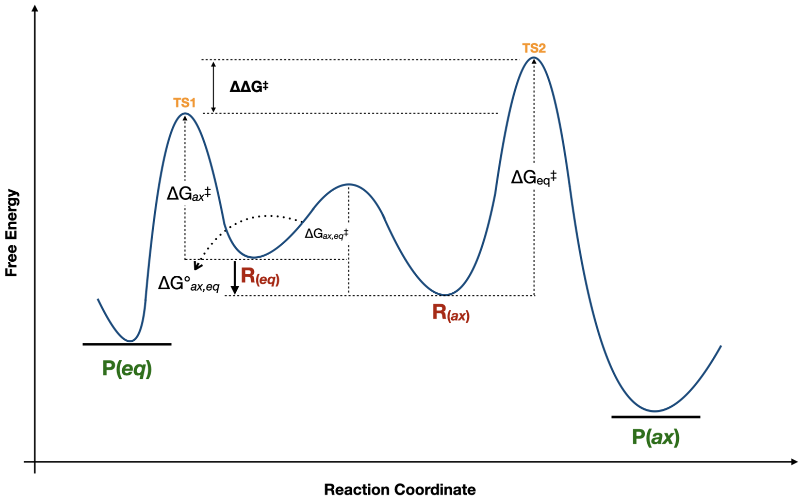

Figure 3.3: Energy difference between two TSs for a reaction that produces two stereoisomers, A and B.[20]

states that under kinetic control conditions, the conformational isomer with the lower activation barrier will determine the product ratio, even if the thermodynamic product is more stable[40].

Therefore, we can calculate the reaction rate constants by applying Equation 3.4 to each TS:

$$k_A = \kappa_A \frac{k_B T}{h} e^{-\frac{\Delta G_A^\ddagger}{RT}} \tag{3.6}$$

$$k_B = \kappa_B \frac{k_B T}{h} e^{-\frac{\Delta G_B^\ddagger}{RT}} \tag{3.7}$$

Assuming that the interconversion between reactants A and B is rapid and that the transmission coefficients are equal, the product ratio can be calculated by dividing the rate constants of both reactions. Since the faster reaction will lead to more product, we obtain:

$$\frac{k_A}{k_B} = \frac{\kappa_A \frac{k_B T}{h} e^{-\frac{\Delta G_A^\ddagger}{RT}}}{\kappa_B \frac{k_B T}{h} e^{-\frac{\Delta G_B^\ddagger}{RT}}} = e^{\frac{\Delta G_B^\ddagger - \Delta G_A^\ddagger}{RT}} \tag{3.8}$$

Thus, under these conditions, the difference in activation free ($\Delta G^\ddagger$) will determine which stereoisomer is preferred. In this work, we will mainly use TST to study the solvent effect and the electric field effect on the stereocontrol of a Hurd–Claisen rearrangement, following the work of Silva[17] and Oliveira[19]. The barrier heights will be calculated using density functional theory (DFT) with the Berny optimization protocol, while the independent and coupled effects of solvation and electric fields will be considered.

3.2 Methods on Electronic Structure

Considering that the electronic structure of a system with N electrons and M nuclei, depends on the spatial coordinates of the electrons and the orientations of the nuclei, it is possible to define a complex-valued wave function ($\psi(\vec{r},\omega)$) that contains all the information about the electronic state of the system. This wave function is a solution of the Schrödinger equation, which can be written as:

$$\hat{H}\psi(\vec{r},\omega) = E\psi(\vec{r},\omega), \tag{3.9}$$

where ω represents the coordinates of all N electrons and the orientations of all M nuclei, $\hat{H}$ is the Hamiltonian operator of the system, and E is the energy eigenvalue associated with the wave function $\psi(\vec{r},\omega)$. The Hamiltonian operator contains information about the kinetic energy of the electrons, the potential energy due to their interactions with each other and with the nuclei, and the potential energy of the nuclei themselves, and can be explicitly written as[41]:

$$\hat{H} = -\frac{1}{2}\sum_{i=1}^{N}\nabla_i^2 - \frac{1}{2}\sum_{A=1}^{M}\frac{\nabla_A^2}{M_A} - \sum_{i=1}^{N}\sum_{A=1}^{M}\frac{Z_A}{r_{iA}} + \sum_{i=1}^{N}\sum_{j>i}^{N}\frac{1}{r_{ij}} + \sum_{A=1}^{M}\sum_{B>A}^{M}\frac{Z_A Z_B}{r_{AB}}, \tag{3.10}$$

here the two first terms represent the kinetic energy of the electrons and nuclei, respectively, the third term represents the interaction between the electrons and the nuclei, the fourth term the electron-electron interaction, and the last term the interaction between the nuclei.

However, while the solution of such an equation is possible in principle, it is not feasible due to the complexity of a system with moving nuclei and electrons. Knowing that any nuclei is a lot heavier than a electron, it is sensible to assume that such nuclei is stationary in relation to the electrons, this is known as the Born-Oppenheimer approximation[41]. Under the Born-Oppenheimer approximation, the electronic Hamiltonian of such a system, in atomic units ($e = m_e = 1/4\pi\varepsilon_0 = 1$), is given by:

$$\hat{H} = -\frac{1}{2}\sum_{i=1}^{N}\nabla_i^2 - \sum_{i=1}^{N}\sum_{A=1}^{M}\frac{Z_A}{r_{ij}} + \sum_{i=1}^{N}\sum_{j>i}^{N}\frac{1}{r_{ij}}, \tag{3.11}$$

as the kinetic energy of a given nuclei can be neglected. The action of the above operator on a wave function (quantum state) allows for the calculation of the energy of a system with N electrons and M nuclei. While this formulation of the hamiltonian operator is more manageable, it still presents a challenge due to the presence of the electron-electron interaction term, which makes the problem non-linear and non-separable. This means that the wave function cannot be expressed as a product of single-electron wave functions, and thus the Schrödinger equation cannot be solved analytically for systems with more than one electron.

One of the first approaches widely adopted in the scientific community to solve the above limitation was the Hartree-Fock[42,43] (HF) approximation. Here the electron-electron potential is assumed to be a mean potential, and the wave function is approximated by a single Slater determinant[44], effectively reducing the problem of a Schrödinger equation for N electrons to N Schrödinger equations for a single electron systems. The HF method is a variational method, and so the energy obtained is an upper bound to the exact ground state energy of the system, thus:

$$E_0^{HF} \geq E_0. \tag{3.12}$$

While the HF approximation successfully describes many systems, it fails to describe the correlation energy, which represents the energy associated with electron-electron interactions, being defined as the difference between the exact ground state energy and the HF ground state energy

$$E_{corr} := E_0 - E_0^{HF}, \tag{3.13}$$

as such, numerous studies have been conducted in search of new approaches to solving equation 3.11 or ways to improve the HF method. Among these works, Møller-Plesset perturbation theory (MP) has stood out.

Being a perturbative approach, MP assumes that the total electronic Hamiltonian can be partitioned into a zeroth-order term, $\hat{H}_0$, and a perturbation, Γ, defined as the difference between the full Hamiltonian and the reference operator, as shown in Equation 3.14:

$$\hat{H} = \hat{H}_0 + \lambda\Gamma, \tag{3.14}$$

where λ is a formal perturbation parameter introduced to facilitate the expansion. In principle, the exact energy of the system can be obtained by expanding the total energy in a power series in λ, according to the Rayleigh-Schrödinger perturbation theory[41,45].

Christian Møller and Milton S. Plesset[46] proposed using the HF solution as the zeroth-order reference. In this formulation, the perturbation operator is defined as the difference between the full electronic Hamiltonian and the HF Fock operator:

$$\Gamma = \hat{H} - \hat{H}_{\mathrm{HF}} = \sum_{i<j}^{N} \frac{1}{r_{ij}} - \sum_{i=1}^{N} \upsilon^{\mathrm{HF}}(\mathbf{r}_i), \tag{3.15}$$

where $\upsilon^{\mathrm{HF}}(\mathbf{r}_i)$ is the mean-field HF potential acting on electron i. The MP method then defines the total energy as the sum of the HF energy and a series of correlation energy corrections at increasing orders.

3.2.1 Density Functional Theory

The high computational cost of post-HF methods, resulting from the excess of information and the lack of physical interpretation of the wave function, led to a search for alternative approaches for obtaining energy and other electronic properties. The electronic density, given by equation 3.16, was used by Thomas[47] and Fermi[48] in 1927 in the model that became known as the Thomas-Fermi model[49]. However, this model was unsuccessful in electronic structure calculations and fell into obscurity until the mid-1960s.

$$\rho(\vec{r}) = N \int \cdots \int |\Psi(\vec{x}_1, \vec{x}_2, \cdots, \vec{x}_n)|^2 d\vec{x}_1 d\vec{x}_2 \cdots d\vec{x}_n = N. \tag{3.16}$$

It was in 1964 that Pierre Hohenberg and Walter Kohn published the work that laid the foundation for Density Functional Theory (DFT). In which, they proved that the energy of a non-degenerate ground-state molecule, its wave function, and consequently all its electronic properties, are uniquely determined by the ground-state electronic density $\rho_0(x,y,z)$[50]. In other words, the ground-state energy is a functional of the electron density (ρ_0), $E[\rho(\vec{r})]$.

Hohenberg and Kohn introduced two theorems, known as the Hohenberg-Kohn theorems (HK), which formed the basis of DFT. The first HK theorem states that, in non-degenerate ground-state systems, the external potential $\upsilon_{ext}(\vec{r})$ is a unique functional of $\rho(\vec{r})$, meaning that different external potentials cannot produce the same electronic density. This potential corresponds to the electron-nucleus interaction[50]. Adopting the Born-Oppenheimer approximation and the Hartree atomic units ($\hbar = m_e = e = 1/4\pi\varepsilon_0 = 1$), the proof goes as follows:

Assuming two external potentials $\hat{V}^{A}_{ext}$ and $\hat{V}^{B}_{ext}$, differing by more than one additive constant, the Hamiltonians generated by these potentials are given by equations 3.17 and 3.18, respectively.

$$\hat{H}^{A} = \hat{T} + \hat{V}_{ee} + \hat{V}^{A}_{ext}, \tag{3.17}$$

$$\hat{H}^B = \hat{T} + \hat{V}_{ee} + \hat{V}^B_{ext}, \tag{3.18}$$

Here, both equations differ only in the external potential, $\hat{V}_{ext}$. $\hat{T}$ represents the kinetic energy of the system, while $\hat{V}_{ee}$ represents the electron-electron potential energy. The Hamiltonians generate two different ground-state wave functions, Ψ^A_0 and Ψ^B_0, corresponding to E^A_0 and E^B_0, respectively.

Assume, for contradiction, that these two distinct ground-state wave functions generate the same electron density, $\rho(\vec{r})$. Since Ψ^B_0 is not an eigenfunction of the ground-state Hamiltonian $\hat{H}^A$, we can use Ψ^B_0 as a trial function for $\hat{H}^A$, applying the variational principle, which states that the expectation value of the Hamiltonian for a trial wave function is always greater than or equal to the true ground-state energy of the system:

$$E^A_0 = \frac{\int \Psi^{A*} H^A \Psi^A d\tau}{\int \Psi^{A*} \Psi^A d\tau = 1} < \frac{\int \Psi^{B*} H^A \Psi^B d\tau}{\int \Psi^{B*} \Psi^B d\tau = 1} = E^B_0, \tag{3.19}$$

Because the Hamiltonians $\hat{H}^A$ and $\hat{H}^B$ differ only in the external potential, we can rewrite the above equation as:

$$E^A_0 < \frac{\int \Psi^{B*} [H^B + \hat{V}^A_{ext} - \hat{V}^B_{ext}] \Psi^B d\tau}{\int \Psi^{B*} \Psi^B d\tau = 1} = E^B_0 + \int [V^A_{ext}(\vec{r}) - V^B_{ext}(\vec{r})] \rho(\vec{r}) d^3 r, \tag{3.20}$$

Aplying the same logic to E^B_0 we get:

$$E^B_0 < E^A_0 + \int [V^B_{ext}(\vec{r}) - V^A_{ext}(\vec{r})] \rho(\vec{r}) d^3 r, \tag{3.21}$$

Finally, adding the two inequalities, we obtain:

$$E^A_0 + E^B_0 < E^A_0 + E^B_0 + \int [V^B_{ext}(\vec{r}) - V^A_{ext}(\vec{r})] \rho(\vec{r}) d^3 r + \int [V^A_{ext}(\vec{r}) - V^B_{ext}(\vec{r})] \rho(\vec{r}) d^3 r = E^A_0 + E^B_0, \tag{3.22}$$

which is a contradiction. Therefore, our initial assumption that two distinct external potentials could produce the same ground-state electron density must be false. This proves that the ground-state electron density uniquely determines the external potential, up to an additive constant. Consequently, all density-dependent properties are uniquely determined by the electron density[51].

The second HK theorem states that if ρ_q is a physically valid electronic probability density, it follows the variational principle. To better understand this theorem, we must first define the energy functional $E[\rho(\vec{r})]$. As shown by the first HK theorem, we can write the ground-state energy as a functional of the electron density,

$$E_0 = E_0[\rho_0] = \bar{T}[\rho_0] + \bar{V}_{ee}[\rho_0] + \bar{V}_{Ne}[\rho_0], \tag{3.23}$$

where the bars above are the expectation values determined by Ψ_0, which can be determined by $\rho_0(\vec{r})$. The eigenvalue for the electron-nucleus interaction operator, $\hat{V}_{Ne}$, is given by equation 3.24,[52]

$$\bar{V}_{Ne}[\rho_0] = \int \rho_0(\vec{r}) v_{ext}(\vec{r}) d\vec{r}. \tag{3.24}$$

The demonstration of this theorem starts by assuming ground state system with electronic density $\rho_{gs}(\vec{r})$ associated with an external potential V_{ext} that leads to the ground state energy E_{gs}. Assuming a trial electronic density $\rho_T(\vec{r})$ that leads to energy E_T.

$$E_{gs} = \frac{\int \Psi_{gs}^* H_{gs} \Psi_{gs} d\tau}{\int \Psi_{gs}^* \Psi_{gs} d\tau} < \frac{\int \Psi_T^* H_{gs} \Psi_T d\tau}{\int \Psi_T^* \Psi_T d\tau} = E_T, \tag{3.25}$$

Analogous to the first theorem, the inequality above leads to:

$$E_{gs} < E^T + \int [V_{ext}^{eg}(\vec{r}) - V_{ext}^T(\vec{r})] \rho(\vec{r}) d^3 r. \tag{3.26}$$

Thus, since the variational principle applies to wave functions, the energy of the system with a trial electronic density is always greater than or equal to the energy of the system at the ground-state electronic density. This establishes the variational principle in the context of DFT[53].

The HK formalism for DFT provides only an existence condition for an electronic density that yields all molecular properties exactly, based on the external potential and a functional that describes kinetic and potential energy. However, neither of its two theorems provides a protocol for determining the exact electronic density nor the explicit form of the electron-electron interaction functional that accounts for correlation effects.

To determine the electronic density without using the wave function, Walter Kohn and Lu Jeu Sham, developed a protocol known as the Kohn-Sham Method (KS method)[54], which, when used in conjunction with equation 3.27,

$$E_0 = E[\rho_0] = \bar{V}_{Ne}[\rho_0] + F[\rho_0], \tag{3.27}$$

is capable of calculating the ground-state energy, as well as the electronic properties, of a molecular system. Given a system with N electrons and M nuclei that satisfies the conditions of the HK theorems, the KS method considers a fictitious system (s) composed of N non-interacting electrons under the same external potential as the original system. According to the first HK theorem, both systems will have the same electronic density, $\rho_o(\vec{r}) = \rho_s(\vec{r})$. The Hamiltonian for an electron i in this fictitious system, denoted as $\hat{H}_i^{KS}$, is the one-electron Hamiltonian given by the kinetic energy of the electron plus the external potential acting on it:

$$\hat{H}_i^{KS} = -\frac{1}{2}\nabla_i^2 + \upsilon_s(\vec{r}_i). \tag{3.28}$$

since the electrons do not interact, the Hamiltonian of the fictitious system can be written as:

$$\hat{H}_s = \sum_{i=1}^{N}\left[-\frac{1}{2}\nabla_i^2 + \upsilon_s(\vec{r}_i)\right] = \sum_{i=1}^{N}\hat{H}_i^{KS}. \tag{3.29}$$

To separate the universal functional $F[\rho_0]$ into a classical and a quantum term, the energy functional is rewritten as:

$$\bar{T}[\rho_0] = \Delta\bar{T}[\rho] + \bar{T}_s[\rho], \tag{3.30}$$

$$\bar{V}_{ee}[\rho_0] = \Delta\bar{V}_{ee}[\rho] + \frac{1}{2}\int\int\frac{\rho(\vec{r}_1)\rho(\vec{r}_2)}{r_{12}}d\vec{r}_1 d\vec{r}_2, \tag{3.31}$$

here, the terms with Δ represent the difference between the original and the fictitious system, while the integral in the second equation corresponds to the classical (Coulombic) interaction of the fictitious system. Substituting these terms in equation 3.23:

$$E[\rho_0] = \bar{T}_s[\rho_s] + \bar{V}_{Ne}[\rho_0] + \frac{1}{2}\int\int\frac{\rho(\vec{r}_1)\rho(\vec{r}_2)}{r_{12}}d\vec{r}_1 d\vec{r}_2 + \Delta\bar{T}[\rho] + \Delta\bar{V}_{ee}[\rho]. \tag{3.32}$$

To determine $\bar{T}_s[\rho]$, the KS method refers back to equation 3.29, as the N non-interacting electrons in the fictitious system have a ground-state wave function given by a Slater determinant[55] in the form:

$$\Psi_{s,0} = \frac{1}{\sqrt{N!}}det\left|\phi_1(\vec{r}_1)\sigma_1\cdots\phi_N(\vec{r}_N)\sigma_N\right|. \tag{3.33}$$

The product $\phi_i(\vec{r}_i)\sigma_i$ is known as a Kohn-Sham spin-orbital, where the spatial part $\phi_i(\vec{r}_i)$ is the eigenfunction of the operator in equation 3.28[56]. Thus, the term $\bar{T}_s[\rho]$ is determined analogously to the kinetic energy in single-determinant HF theory by applying the Slater-Condon rules[45], since the determinants do not differ in any spin-orbital.

$$\bar{T}_s[\rho] = -\frac{1}{2}\sum_{i=1}^{N}\langle\phi_i(1)\left|\nabla_i^2\right|\phi_i(1)\rangle. \tag{3.34}$$

The $\bar{V}_{Ne}[\rho_0]$ is previously described by Hohenberg and Kohn, as the nuclei-electron interaction energy[50]:

$$\bar{V}_{Ne}[\rho_0] = \langle\Phi_0\left|\sum_{i=1}^{N}\upsilon(\vec{r}_i)\right|\Phi_0\rangle = \int\rho_0(\vec{r})\upsilon(\vec{r})d\vec{r}, \tag{3.35}$$

the above equation can be rewritten based on the ideia that the electron densities of both system are the same,

$$\int\rho_0(\vec{r})\upsilon(\vec{r})d\vec{r} = \bar{V}_{Ne}[\rho_0] = -\sum_{j=1}^{M}Z_j\int\frac{\rho_s(\vec{r}_1)}{r_{1j}}d\vec{r}_1. \tag{3.36}$$

Lastly, Kohn and Sham proposed a exchange correlation functional $E_{xc}[\rho]$ to account for the correlation energy, which is the difference between the exact ground-state energy and the sum of the kinetic and potential energies of the non-interacting system. The exchange-correlation functional is a universal functional that depends only on the electron density, and its form is unknown. The total energy functional is then given by:

$$E[\rho] = -\frac{1}{2}\sum_{i=1}^{N}\langle\phi_i(1)\left|\nabla_i^2\right|\phi_i(1)\rangle - \sum_{j=1}^{M}Z_j\int\frac{\rho(\vec{r}_1)}{r_{1j}}d\vec{r}_1 + \frac{1}{2}\int\int\frac{\rho(\vec{r}_1)\rho(\vec{r}_2)}{r_{12}}d\vec{r}_1 d\vec{r}_2 + E_{xc}[\rho], \tag{3.37}$$

note that the tree first terms of equation 3.37 are the kinetic energy, the electron-nucleus interaction energy and the electron-electron interaction energy, respectively, all of which are easily evaluated. Up until this point the DFT is an exact theory, the only approximation is form of the exchange-correlation functional, which is the subject of many studies in the scientific community[57–60].

It is worth noting that the exchange-correlation functional $E_{xc}[\rho]$ contains all quantum-mechanical effects not captured by the first three terms[61], such as the influence of electron-electron interactions on the kinetic energy of each electron in the system. To obtain $E[\rho]$ in equation 3.37, one must determine the electronic density that minimizes the system's energy by applying the variational method. This requires finding the Kohn-Sham orbitals ϕ_i that minimize the functional $E[\rho]$. However, the KS orbitals must remain orthonormal during the minimization process ($\int \phi_i^(1)\phi_i(1)d\vec{r} = \delta_{ij}$). This is achieved by simultaneously minimizing the KS orbital-dependent functional while enforcing the constraint using the method of Lagrange multipliers.

$$\delta\left(E[\rho] - \varepsilon_i \int |\phi_i|^2 d\vec{r}_1\right) = \frac{\partial E}{\partial \phi_i^*} - \varepsilon_i \frac{\partial}{\partial \phi_i^*} \int |\phi_i|^2 d\vec{r}_1 = 0, \tag{3.38}$$

where ε_i is the lagrange multiplier representing the chemical potential of a system[62], finaly we obtain the energy functional in terms of the KS orbitals:

$$\begin{gathered} E[\rho] = E[\phi_i] = -\sum_{i=1}^{N} \int \left(\sum_{j=1}^{M} \frac{Z_j}{r_{1j}} |\phi_i(1)|^2 d\vec{r}_1\right) - \frac{1}{2}\sum_{i=1}^{N} \langle \phi_i(1) \left|\nabla_1^2\right| \phi_i(1) \rangle + \\ \frac{1}{2}\sum_{i=1}^{N}\sum_{k=1}^{N} \int\int |\phi_i(1)|^2 \frac{1}{r_{12}} |\phi_k(2)|^2 d\vec{r}_1 d\vec{r}_2 + E_{xc}[\rho] \end{gathered} \tag{3.39}$$

Theese orbitals follow the following psudo-eigenvalue equation[56]:

$$\left[-\frac{1}{2}\nabla_1^2 - \sum_{j=1}^{M} \frac{Z_j}{r_{1j}} + \int \frac{\rho(\vec{r}_2)}{r_{12}} d\vec{r}_2 + \frac{\partial E_{xc}}{\partial \rho}\right] \phi_i(1) = \varepsilon_i^{KS} \phi_i(1), \tag{3.40}$$

where $\frac{\partial E_{xc}}{\partial \rho}$ is the exchange-correlation potential $\upsilon_{xc}(\vec{r})$, hance we can rewrite the equation external potential by comparing it with the equation 3.28:

$$\upsilon_s(1) = \sum_{j=1}^{M} \frac{Z_j}{r_{1j}} + \int \frac{\rho(\vec{r}_2)}{r_{12}} d\vec{r}_2 + \frac{\partial E_{xc}}{\partial \rho}, \tag{3.41}$$

The KS operator is simply the Fock operator minus the exchange-correlation potential, and thus both can be solved using self-consistent methods, since the exchange-correlation potential depends on the electronic density.

The only part of equation 3.40 that does not have a well-defined expression is the exchange -correlation potential, which contains all the corrections to the energy functional of the non-interacting fictitious system. If the exact potential were known, Kohn-Sham DFT would yield exact results. However, to this day, no universal form for this potential has been found. Research in DFT aims to approximate this functional as accurately as possible[63], developing approximate functionals that better account for exchange effects.

Among the many DFT approximations we can highlight the Local Density Approximation (LDA), which is based on the electron gas model, the Generalized Gradient Approximation (GGA), that includes the gradient of the electron density in the exchange-correlation functional, the hybrid functionals, which combine the Hartree-Fock method with DFT to better account to exchange effects, and lastly the range separeted hybrids which are a variation of the hybrid functionals that include a range separation parameter to better account for long range interactions.[53,64]

In this work DFT was applied as the main method for the calculation of the electronic structure of the systems studied. The good balance between computational cost and accuracy of the results makes DFT a good choice for the study of the electronic structure of the transition state systems. The M062X functional was chosen for the calculations, as it is a hybrid functional that has been shown to be effective in the study of the Hurd-Claisen rearrangement transition states[17,19,65].

3.3 Solvatochromic Efects

While the advent of DFT greatly improved the accuracy and usability of theoretical methods, discrepancies between theoretical and experimental results still persist. These differences may arise from both intrinsic limitations of DFT and also from the differing conditions under which systems are modeled (e.g., in vacuum vs. in solution)[66].

In chemistry, it is well known that solvent effects play a critical role. Solute-solvent interactions can influence various physicochemical properties, such as molecular structure[67], spectroscopic characteristics[68], and nonlinear optical responses[69]. Another key aspect of solvent importance is its impact on organic synthesis. The solvent can affect the reactivity and stability of the solute, as well as its conformational preferences. Therefore, an accurate description of these interactions is essential for a deeper understanding of the system under study[34,40]

When it comes to modeling solute-solvent interactions, there are two ways to model such interactions: explicit, which takes into account each solvent interaction with the solute, and implicit, which evaluates the influence of the solvent by indirect means, usually surrounding the solute through a cavity modeling some aspects of the solvent. In general, implicit methods are the most used solvation methods in computational chemistry, due to their low computational cost. One of the most widespread implicit methods is the polarizable continuum model[70] (PCM), that treats the solvent as a dielectric continuum and just takes into account the solvation-free energy and the electrostatic solute-solvent interaction[71]. However, they are not the most accurate methods, as they do not take into account the atomistic interactions between the solvent molecules and the solute[64].

Due to this work focus on modeling all external environmental effects on transition states, the explicit method is the most suitable. Conventional explicit solvent treatment methods solve the system's equations of motion recursively. That is, perturbations in one region of the system propagate throughout it, starting from an initial configuration of solvent and solute molecules in space. After a sufficient amount of time, the system's trajectory is obtained, from which the property of interest is determined as a time average over this trajectory.

Methodologies that use classical equations are called molecular mechanics simulations (*Molecular Mechanics, MM*), those that employ quantum mechanics equations are quantum mechanical simulations (*Quantum Mechanics, QM*), and simulations that treat part of the system quantum mechanically and another part classically are known as QM/MM simulations.

The Sequential Quantum Mechanics/Molecular Mechanics (S-QM/MM) model, proposed by Kaline Coutinho and Sylvio Canuto in 1997[25], is a low-cost and highly flexible alternative for treating solvent effects in organic systems. The S-QM/MM model first performs a classical stochastic simulation using the Monte Carlo (MC) method with Metropolis sampling to generate a set of solute-solvent configurations. The uncorrelated configurations are then used to calculate the quantum-mechanical properties of interest. A key feature of this methodology is the use of charge points instead of solvent molecules, during the QM portion, significantly reducing the computational cost of the simulation. This approach to modeling chemical environments has gained prominence in recent research, both in the solid state[72,73] and in solution[28,34].

3.3.1 Sequential Quantum Mechanics Molecular Mechanics Aproach

The S-QM/MM approach evaluates the solute-solvent interaction energy using:

$$E = \sum_{A,B} \sum_{ij} U(r_{ij}), \tag{3.42}$$

the first summation runs over all molecules in the system, while the second over all atoms within each molecule. The pair potential $U(r_{ij})$ is defined as the sum of the Coulomb and the Lennard-Jones potentials between atoms i and j.

$$U(r_{ij}) = 4\sqrt{\varepsilon_i \varepsilon_j}\left[\left(\frac{\sqrt{\sigma_i \sigma_j}}{r_{ij}}\right)^{12} - \left(\frac{\sqrt{\sigma_i \sigma_j}}{r_{ij}}\right)^{6}\right] + \left(\frac{q_i q_j}{r_{ij}}\right), \tag{3.43}$$

where q, σ and ε represent the partial charges and OPLS parameters of atoms i and j respectively. The distance between atoms i and j is given by r_{ij}.

For a system containing N molecules, the S-QM/MM methodology generates an initial random configuration of solvent molecules around the solute. The Monte Carlo method is then used to generate a new configuration by varying the spatial positions of all solvent molecules. This process utilizes the energy calculated by equation 3.42 and follows the Metropolis sampling criterion. To evaluate the property (η) of a system with many interacting molecules, we need to solve the expected value integral for a space X:

$$\langle \eta \rangle_{ens} = \frac{\int_X \eta\,(X)\,\rho\,(X)\,dX}{\int_X \rho\,(X)\,dX}, \tag{3.44}$$

Here, ρ represents a non-normalized probability distribution inside a given ensemble. Nicolas Metropolis[74] showed that the integral 3.44 can be replaced by a much simpler mean of C distant positions of all the molecules in the system:

$$\langle \eta \rangle_{ens} = \frac{1}{C}\left[\eta(X_1) + \eta(X_2) + \cdots + \eta(X_C)\right] = \frac{1}{C}\sum_{i=1}^{C} \eta(X_i) \tag{3.45}$$

Thus, the uncorrelated positions are obtained by means of a Markovian chain, generated by a transition matrix defined as[74,75]:

$$\begin{aligned} \Pi_{i,i+1} &= 1, & \rho_{i+1} \geq \rho_i \\ \Pi_{i,i+1} &= \frac{\rho_{i+1}}{\rho_i}, & \rho_{i+1} < \rho_i \end{aligned} \tag{3.46}$$

where $\Pi_{i,i+1}$ represents the probability of the system transitioning from state i to $i+1$. Equation 3.46 can be modified depending on the desired ensemble. For the canonical (NVT) the probability of occurrence of a state is given by Boltzman distribution, while the test property is the total potential energy, the Metropolis criterion for the NVT ensemble becomes as follows:

$$\begin{aligned} \Pi_{i,i+1} &= 1, & E_{i+1} < E_i \\ \Pi_{i,i+1} &= \frac{e^{E_i/\kappa T}}{e^{E_{i+1}/\kappa T}}, & E_{i+1} \geq E_i \end{aligned} \tag{3.47}$$

After the Monte Carlo simulation is completed, most of the generated configurations are similar, so only a smaller subset is selected. These are referred to as uncorrelated configurations due to their low similarities. To identify them, the method employs the temporal correlation function, given by[25]:

$$\chi = \frac{1}{2} \lim_{l_b \to \infty} \frac{l_b \langle \partial E^2 \rangle_b}{\langle \partial E^2 \rangle}, \tag{3.48}$$

Thus, instead of calculating the desired property for all accepted solvent configurations, only a small group of $1/\chi$ configurations need evaluation using quantum methods. For the sake of simplicity, it is common to select one every 250 accepted solvent configurations[29,76,77].

3.3.1.1 Average Solvent Electrostatic Configuration

The S-QM/MM methodology can model the solvent effect at a lower computational cost compared to conventional QM/MM methodologies. However, as elucidated by Canuto[78], an adequate S-QM/MM simulation requires a minimum of 80 uncorrelated configurations, meaning 80 expensive QM calculations. Thus, although this methodology is faster than conventional explicit solvation approaches, it still presents a significant computational cost compared to implicit solvation methods. For this reason, in their 2007 work[27], Coutinho and collaborators proposed the ASEC (Average Solvent Electrostatic Configuration) approach to reduce the computational burden of the S-QM/MM methodology.

At its core, ASEC aims to minimize the number of quantum calculations required to just a single quantum calculation. To achieve this, the protocol overlays the uncorrelated configurations of the solvent molecules. In this approach, the entire solvent system is treated as charge points, limiting superposition erros, generating a single quantum calculation of a solute molecule surrounded by this super-configuration of solvent molecules (as schematized in Figure 3.4[64]).

For example, given an S-QM/MM simulation that results in η uncorrelated configurations of N solvent molecules surrounding a solute molecule, these η configurations are centered at the origin. Then, the solvent molecules from all uncorrelated configurations are overlaid, resulting in a single configuration containing $\eta \cdot N$ solvent molecules surrounding the solute. The partial charges of the solvent atoms are scaled by a factor of $1/\eta$, and this normalized configuration is used for the QM calculations.

This approach leads to a significant reduction in the computational time of an S-QM/MM solvation. As such, Georg et al. proposed in 2006 an electrostatic relaxation of the solute

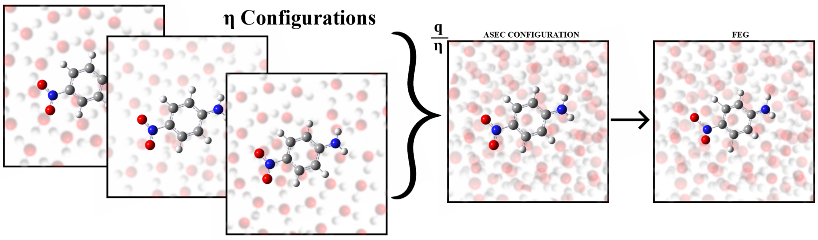

Figure 3.4: Schematic representation of the ASEC approximation[64], coupled with the FEG optimizaition. η uncorrelated solute-solvent configurations are overlaid into a single ASEC configuration, and the charges from all charge points are then averaged over the number of overlaid configurations.

charges[26]. The electric field generated by the solvent charges (here represented by an ASEC configuration of charge points) induces notable changes in the electronic distribution of the solute molecule, consequently leading to a reorientation of its multipole moment[25,26,64]. This reorientation alters the partial charges of the solute, and as stated by Coutinho[24,25], the S-QM/MM methodology is highly dependent on the partial charges of the aforementioned solute, thus the positioning of the solvent molecules will change following the perturbation of tho solut charges.

Note that, once again, the solvent conformation will lead to changes in the atomic charges of the solute molecule, creating a recursive interaction between the two. The methodology proposed by Georg allows the solute electrostatic relaxation to take place by performing a series of consecutive S-QM/MM simulations. Each time, the solute atomic charges are updated, and a new MC simulation is carried out, allowing a new solvent positioning to take place. This interaction is repeated until the convergence of the solute atomic charges is detected, usually based on the magnitude of the molecule's dipole moment. Coupling the S-QM/MM methodology with the ASEC approximation allows the evaluation of solvatochromic effects that account for electrostatic changes in the solute molecule. However, this methodology cannot account for geometric changes in the solute molecule. The overlaying of multiple statistically relevant configurations requires that the solute molecule remains in the same conformation, and electrostatic relaxation does not lead to changes in the solute's geometry.

The solute-solvent interaction in the QM portion of the simulation is incorporated by changes in the one-electron term of the solute's Hamiltonian[27,34]. Consequently, if the solute geometry is allowed to relax, it would change based on the electric field generated by the charge points. To account for such geometric changes, the ASEC-FEG variation was proposed in 2012[67,79], introducing an additional QM step wherein the solute geometry is allowed to be slightly altered by means of a free energy gradient.

3.3.1.2 Free Energy Gradient

Assuming tree dimensional single particle, the potential energy of a system can be expressed as a function of the position x, y and z of the particle as $U(x,y,z)$. By taking the gradient of this function, we can obtain the force acting on the particle at a given position:

$$\vec{F} = -\nabla U(x,y,z) = -\left(\frac{\partial U}{\partial x}\hat{i} + \frac{\partial U}{\partial y}\hat{j} + \frac{\partial U}{\partial z}\hat{k}\right). \tag{3.49}$$

So, based on the potential energy that a particle is subjected to, we can calculate the force acting on it. The force acting on a particle can then be used to calculate the work done by the particle when it moves from a position A to a position B. Assuming a molecular system with N nuclei, the potential energy of the system can be expressed as a function of the position of each nucleus, $U(\vec{R}_1, \vec{R}_2, \cdots, \vec{R}_N)$, and thus, by taking the gradient of this function, we can obtain the force acting on each nucleus. The force acting on a nucleus can be used to calculate the work done by the nucleus when it moves from position A to position B, as illustrated in Figure 3.5.

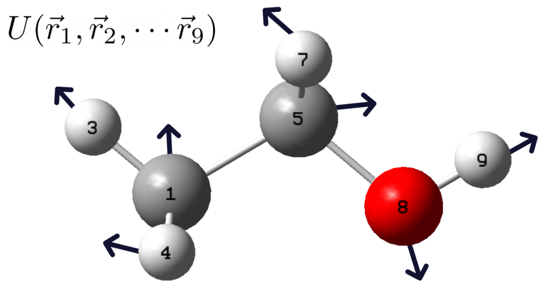

Figure 3.5: Schematic representation of the forces acting on each nucleus as it moves from configuration A to configuration B. The point charges of the solvent exert forces on the solute nuclei, which can be calculated from the gradient of the system's free energy.

By calculating the force and the Hessian matrix during each step of the iterative S-QM/MM simulation (QM steps), the position of each solute nucleus can be slightly adjusted based on the solute-solute and solute-solvent potential. The force acting on the solute atoms can be calculated, considering the solvent influence, as follows[80]:

$$F^{FE}(\vec{r}) = -\left\langle \frac{\partial (V^{solt} + V^{solv})}{\partial \vec{r}} \right\rangle, \tag{3.50}$$

where V^{solt} represents the solute-solute interaction energy and V^{solv} represents the solute-solvent interaction energy. The brackets denote the average over the uncorrelated configurations. The Hessian matrix is computed as[80]:

$$H_{ij} = \left\langle \frac{\partial^2 (V^{solt} + V^{solv})}{\partial \vec{r}_i \partial \vec{r}_j} \right\rangle, \tag{3.51}$$

assuming that the geometry changes are small.

Effectively, by using Gaussian[81] to calculate the force constants of the perturbed solute molecule, it is possible to determine the geometry relaxation of the solute molecule[28,67]. In this work the S-QM/MM methodology coupled with the ASEC-FEG approximation is used to evaluate the influence of the solvent on the geometry of the transition state of Hurd-Claisen rearrangement, this aproach can be easily extended to Electric Field calculation due to the sequential nature of the S-QM/MM methodology.

3.4 Electric Fields in Chemistry

The field generated by a charge Q can be evaluated using Coulomb's law:

$$\vec{F} = \frac{1}{4\pi\varepsilon_0} \frac{Q}{r^2} \hat{r}, \tag{3.52}$$

where $\vec{F}$ is the electric field, ε_0 is the vacuum permittivity, r is the distance from the charge, and $\hat{r}$ is the unit vector in the direction of the charge. In chemistry, the polarizing capabilities of an electric field have long been a subject of curiosity in theoretical physical-chemistry[10,82], but in recent years, the advent of complex experimental techniques has brought this concept to new light. Researchers, including Aragonés[12], have utilized scanning tunneling microscopy (STM) to catalyze the classic Diels-Alder reaction between a norbornene derivative fixed on a gold surface and a furan molecule attached to the STM probe tip.

These applications have originated a new field of study, named electrocatalysis, which uses oriented electric fields (OEEFs) to accelerate and control the stereochemistry of chemical reactions[15,21]. To better understand how electric fields can influence chemical reactions, we need to understand how an OEEF interacts with chemical bonds. As peer the valence bond theory, a covalent bond is the superposition of orbitals, forming a region with relatively high electron density[33]. As such, the covalent bond can be polarized by the presence of an electric field. The polarization of the bond can be described by the following equation:

$$\Delta E = Q\vec{F} \cdot \vec{r}, \tag{3.53}$$

where ΔE is the energy of interaction between the OEEF and the bond electrons, $\vec{F}$ is the electric field, Q is the charge of the bond, and $\vec{r}$ is the distance from the bond to the electric field. The ingenious idea is that the OEEF will increase the ionic character of the bond, making it more reactive. Figure 3.6 shows the effect of an electric field on a covalent bond.

Figure 3.6: Effect of an electric field in a covalent bond.

This process leads to the lengthening of homopolar bonds, caused by the increase in the ionic character of the atoms, which will align with the electric field. Heteropolar bonds, like $C-O$, will follow the same principle if the field is oriented towards the more electronegative atom of the bond, or the bond will be shortened if the field is oriented towards the more electropositive one.[21]

Most of the reagents used in organic or inorganic synthesis exhibit a permanent dipole moment at various stages of the reaction pathway (reagents, transition state, and products). Therefore, the OEEF can interact with the dipole moment of the activation complex, which is significantly higher than that of stable molecules[21,36]. This energitic change between the TS and reactant is described by[21]:

$$\Delta\Delta E = \frac{\vec{F} \cdot \Delta\vec{\mu}}{4.8}, \tag{3.54}$$

where $\Delta\vec{\mu}$ is the variation of the dipole moment of the activation complex and the reactant. Equation 3.54 shows that an alignment of the OEEF with the dipole moment of the activation complex will lower the energy of the reaction, while an anti-alignment will increase it.

The above-mentioned interaction is the basis of electrocatalysis. Shaik, in an overview of the practice, proposed the axis rule[15], which states that aligning the OEEF with the path of electronic movement accelerates the reaction. Thus, the present work aims to investigate the influence of the OEEF on the Hurd-Claisen rearrangement, using the axis rule as a guide for the orientation of the electric field during the reaction, as well as evaluating the influence of the field on the transition state and the reactant, assessing its use as a stereocontrol agent.

Chapter 4

Methodology

The work of Oliveira and collaborators[19] observed the influence of non-covalent effects on the Hurd-Claisen rearrangement reaction, and it became clear that the intramolecular interactions responsible for the reaction are predominantly electrostatic in nature, shedding light on the unprecedented stereoselectivity reported by Silva.[17] The present work aims to study the catalytic effect provided by external electric fields, as well as the influence of solvent effects, in the Hurd-Claisen rearrangement.

In this section, we will present a more detailed description of the studied systems, paying close attention to the reaction axis rule.[15] Next, the computational details of the calculations will be discussed in detail. Lastly, a comprehensive description of the functionalities of *MoleKing* will be presented, highlighting its usefulness in OEEF calculations. To maintain comparability with the previous work, all geometry optimizations and frequency calculation were performed in the M062X/6-311+g(d, p) level of theory with a following single point correction at the M062X/def2-tvpp level of theory.

4.1 The Hurd-Claisen Rearrangement

The Claisen rearrangement is a powerful tool in organic synthesis for forming new carbon-carbon bonds.[83,84] Owing to the concerted pericyclic mechanism of this reaction, a new $C = C$ bond is stereoselectively installed in the product. Its Hurd variant proceeds through a two-step process in which an allylic alcohol is converted *in situ* into its corresponding allyl enol ether, which subsequently rearranges to form the final product. Oliveira previously evaluated the impact of various functional and electron-withdrawing groups on product selectivity. In order to expand upon this study by including the effects of external electric fields (EEFs) and solvation, two variants of the Hurd-Claisen rearrangement were analyzed: one containing an ester group (Hurd-Est) and another containing a nitrile group (Hurd-Nit). A series of organic substituents were investigated for each system, including *para*-aminophenyl (NH_2Ph), *para*-nitrophenyl (NO_2Ph), phenyl (Ph), methyl (CH_3), ethyl (Et), isopropyl (SProp), isobutyl (IsoBut), and tert-butyl (TBut).

This array substituents constitute a sample of diverse competitive factors in the stabilization of transition states, ranging from bulky fragments (to assess the steric impact on the

E/Z ratios of the rearrangement) to electronic effects by employing electron-donating and electron-withdrawing groups (to evaluate the electrostatic impact on the E/Z ratios). Both variations of the Hurd-Claisen rearrangement were studied, with the substituent group in the axial position and in the equatorial position. The reaction coordinate diagram for the Hurd-Claisen rearrangement is shown in Figure 3.3.

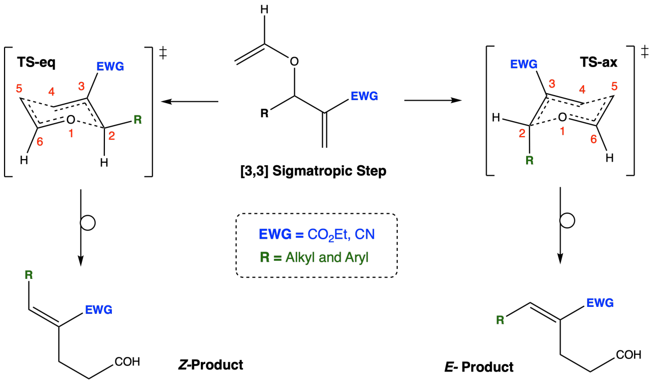

Figure 4.1: Sigmatropic step of the for the Hurd-Claisen Rearrangement using CO_2Et and CN as the electron-withdrawing groups. For better visualization, the aryl and alkyl substituents are represented separately and the Axial (E) and Equatorial (Z) Activation Complexes are shown inside square brackets. This image was taken from[20].

During the evaluation of the reaction kinetics, the Curtin-Hammett principle was considered, inspired by the works of Peng[20,85]. Equation 3.8 can be readily used to describe the stereoselectivity ratio E/Z of the Hurd-Claisen rearrangement. In this context, the activation barrier difference, denoted as $\Delta\Delta G^{\ddagger}$, is defined as:

$$\Delta\Delta G^{\ddagger} = \Delta G^{\ddagger}_{\text{eq}} - \Delta G^{\ddagger}_{\text{ax}} \tag{4.1}$$

where $\Delta G^{\ddagger}_{\text{eq}}$ corresponds to the activation free energy associated with the equatorial position (eq - isomer Z), and $\Delta G^{\ddagger}_{\text{ax}}$ corresponds to the axial position (ax - isomer E). In Figure 3.3, the reaction coordinate diagram illustrates the pathways for the formation of both isomers via their respective transition states (TS1 and TS2). The basic assumption of the Curtin-Hammett principle is that the interconversion of the E/Z reactants is fast compared to the rate of the reaction, and the product distribution is determined by the relative stability of the transition states, allowing the simplification of the evaluation of the stereoselectivity of the reaction by accounting for the interconversion of the reactants implicitly:

$$\Delta\Delta G^{\ddagger} = (\Delta G^{\ddagger}_{\text{eq}} - \Delta G^{\ddagger}_{\text{ax}}) + \Delta G^{\circ}$$
$$\Delta\Delta G^{\ddagger} = (G_{\text{TS(eq)}} - G_{\text{R (eq)}}) - (G_{\text{TS(ax)}} - G_{\text{R (ax)}}) + (G_{\text{R(eq)}} - G_{\text{R (ax)}})$$
$$\Delta\Delta G^{\ddagger} = G_{\text{TS(eq)}} - \cancel{G_{\text{R (eq)}}} - G_{\text{TS(ax)}} + \cancel{G_{\text{R (ax)}}} + \cancel{G_{\text{R(eq)}}} - \cancel{G_{\text{R (ax)}}}$$
$$\Delta\Delta G^{\ddagger} = G_{\text{TS(eq)}} - G_{\text{TS(ax)}}$$

This derivation leads to a direct way accond for the stereoselectivity of the reaction by evaluating the difference in the activation barriers of the transition states. The sign of $\Delta\Delta G^{\ddagger}$ determines the stereoselectivity of the reaction. A negative value of $\Delta\Delta G^{\ddagger}$ indicates a more stable equatorial transition state (TS), while a positive value suggests a more stable axial TS.

4.2 Computational Details

The subsequent section provides a detailed description of the computational methods used in this work, as well as an overview of some of the code developed to automate the process. For better readability, the section is divided into two parts: OEEF Evaluation and Solvation Methodology.

4.2.1 OEEF Evaluation

All calculations involving oriented electric fields were performed using the Gaussian16 quantum chemistry package,[81] employing DFT. To maintain consistency with previous work, these calculations were carried out at the M062X/def2-tzvpp// M062X/6-311+G(d,p) compound model. It is important to note that M062X, a hybrid density functional from the Minnesota suite[65], is extensively used for calculating transition state geometries due to its high accuracy.[86–88]

The initial geometry was taken from the work of Oliveira,[19] and the OEEF optimization was performed following the recommendations of Shaik's work.[15,21] Two different general orientations of the electric fields were considered: one following the reaction axis rule and the other using the molecular axis as a reference. All OEEF calculations were performed with varying field strengths to evaluate the influence of both weak and strong electric fields on the reaction. The reaction axis rule had a field strength of -8.00×10^{-3} to 8.00×10^{-3} a.u., while the molecular axis was evaluated with field strengths of $\pm 1.00 \times 10^{-5}$ and $\pm 6.00 \times 10^{-5}$ a.u. to elucidate the effect of weaker fields.

The reaction axis consists of the vector that points from the nucleophilic site to the electrophilic site. Observing Figure 4.2, it becomes clear that the general flow of electrons

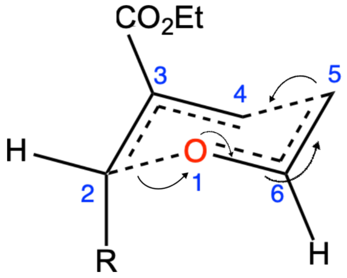

Figure 4.2: Electronic flow of the ax-Hurd-Claisen rearrangement, the curved arrows indicate the electronic movement. Red indicates the formation of a $C-C$ bond, while blue indicates the breaking of a $C-O$ bond.

follows two opposite directions, hence the simultaneous formation of a $C-C$ bond and the breaking of a $C-O$ bond. Thus, for the Hurd-Claisen rearrangement (and all Claisen sigmatropic rearrangements), the reaction axis can be defined along the $C-O$ bond that will be broken or the $C-C$ bond that will be formed. This result is similar to the work of Wang et al. about the electrocataliosys of the Diels Alder reaction.[16]

The reaction axis rule states that the electric field should be oriented along the reaction axis to maximize its effect on the reaction. To achieve this result in Gaussian16, one should align the desired bond with the z-axis and apply the electric field along the same axis. This reorientation process can be very cumbersome and prone to human error. To mitigate this issue, *MoleKing* was employed to automate the process by reordering the atoms of all studied molecules, assigning them new indices, and then reorienting the molecule along the desired axis.

When dealing with the thousands of point charges generated during the S-QM/MM solvation process, *MoleKing* also applies the same rotation rules to the point charges, thus ensuring that the electric field is correctly oriented along the reaction axis.

The molecular axis can be obtained by performing a Principal Component Analysis (PCA) on the molecule's coordinates. The PCA algorithm calculates the eigenvectors of the covariance matrix of the molecule's coordinates, which are then used to define the molecular axis. This axis is determined by the eigenvector with the largest eigenvalue, corresponding to the direction of the molecule's longest axis. The electric field can then be oriented along this axis to evaluate its influence on the reaction, not only along the reaction axis but also in other directions. A good point to note is that weaker fields leads to negligible changes on molecular geometry[89], thus molecular axis was evaluated with out geometry optimization.

This approach allows for a more comprehensive evaluation of the OEEF effect on the reaction under a more general orientation of the electric field, which tends not to catalyze the reaction as effectively as the reaction axis rule but can alter stereoselectivity by inducing changes in the transition state geometry. Once again, *MoleKing* was used to automate the process of obtaining and reorienting the molecule along the molecular axis through the `alingMolecule` function.

4.2.2 S-QM/MM

The S-QM/MM solvation method was performed using the DICE software[24,90] in conjunction with ASEC-FEG[26–29] approximation. The transition states were embedded in a box containing 500 EVE (ethyl vinyl ether) molecules at 373 K to maintain comparability with the work of Silva.[17] The box dimensions were defined according to the experimental density of the solvent. These simulations were divided into two stages.

In the first stage, called thermalization, two Monte Carlo simulations were performed, referred to as the first and second thermalization, respectively. The first thermalization, carried out at constant volume, consisted of 4.00×10^7 Monte Carlo steps and 150 cooling steps, with the aim of adjusting the initial positions of the solvent molecules to achieve a more stable configuration. This process allows the solvent molecules to approach or move apart to minimize the system's total energy.

The second thermalization, conducted at constant pressure, involved 6.00×10^7 Monte Carlo steps, allowing the box volume to adjust according to the magnitude of solvent-solvent interactions. This variation in the total box volume promotes the relaxation of electrostatic solvent-solvent interactions.

This thermalized system is used as the starting point for the second stage of the simulation, referred to as the equilibrium simulation. It is performed at constant pressure (to maintain the solvent density during the simulation), totaling 1.25×10^8 Monte Carlo steps. The number of Monte Carlo steps in the equilibrium simulation was chosen with the objective of obtaining 125 uncorrelated configurations, sampling one configuration every 2,000 Monte Carlo steps.

The 125 configurations obtained were then combined into the ASEC configuration, that was used in subsequent quantum calculations. During the quantum mechanical part of an S-QM/MM simulation, the solvent molecules are often treated as point charges. After the ASEC superposition, the system becomes a large set of Cartesian coordinates. Therefore, the use of *MoleKing* to handle the normalization and parsing of the ASEC configuration was crucial for optimizing the S-QM/MM simulations.

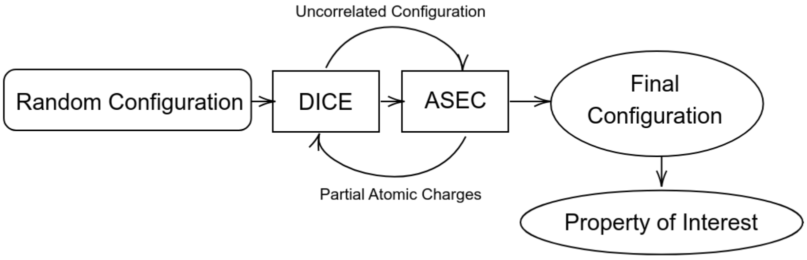

Figure 4.3: General scheme of ASEC-FEG. Adapted from Matias, 2023.[64]

This solute-solvent configuration is then subjected to the geometrical relaxation of the free energy gradient. Typically, an external optimization routine is employed to minimize the free energy gradient. However, in this work, in an effort to reduce computational costs, the gradient was minimized using the Gaussian16 package,[81] by performing single-step geometry optimizations (using the Berny algorithm) at the M06-2X/6-311+G(d,p) level of theory. At each subsequent step, another geometry optimization was performed, effectively producing an N-step minimization of the FEG in a simulation with N steps. After this relaxation, the atomic charges of the solute are recalculated using the Merz-Kollman (MK) population analysis.

Using the calculated MK charges, a new dipole moment of the solute is obtained. These new charges and geometric parameters of the solute are then used in a fresh S-QM/MM simulation, which will produce a new dipole moment and a new set of charges/positions to be used in another S-QM/MM simulation. This process is repeated at leas of 10 times or until the convergence of the dipole moment. Figure 4.3 brings a schematic representation of the whole process.

To optimize the iterative procedure described above, a new version of the *DicePlayer* code[31] was developed using Python 3.x. This code automates the ASEC protocol, identifies the dipole moment convergence point, and partitions the equilibrium simulation, with 1.25×10^8 Monte Carlo steps, into n smaller simulations, each containing 1.25×10^8 Monte Carlo steps, performed simultaneously. The sum of the results from these parallel simulations can be interpreted as equivalent to a single 1.25×10^8-step Monte Carlo simulation and is used to generate the ASEC distribution. This parallelization of the equilibrium simulation reduces the total simulation time by a factor of n.

The code uses files directly extracted from the LigParGen server[91–93] as input to generate the correct OPLS parameters for the solvent molecules. As mentioned before, *MoleKing* was used to both normalize the ASEC configuration and parse the files for the *DicePlayer* code in a faster and more efficient manner. By using this version of the *DicePlayer* code, the otherwise convoluted ASEC-FEG process was simplified and optimized, significantly reducing human error and computational time.

4.3 MoleKing

MoleKing is a Python package written in C++ with linkage powered by `pybind11`. It contains several useful classes for those who develop Python scripts aimed at computational chemistry. The main goal of this package is to introduce chemistry-related concepts and objects, such as *Molecules*, *Atoms*, and *Geometries*, into Python, making programming more intuitive and accessible for chemists.

One of the main challenges in chemistry programming is the lack of chemical intuition in the code. By using *MoleKing*, users can easily create and manipulate molecules, atoms, and complex molecular systems, making the code more readable and intuitive. Additionally, *MoleKing* is capable of reading and writing input and output files for the Gaussian 16 package and the Psi4 SAPT module[94].

The building blocks of *MoleKing* are the *Atom* and *Molecule* classes. The *Atom* class represents a single atom, containing information such as its atomic number, symbol, and Cartesian coordinates. The *Molecule* class, on the other hand, represents a collection of atoms using a vector, allowing the user to manipulate and analyze molecular systems.

From a quantum perspective, a chemical bond is defined by the distance between two atoms. Therefore, by using the covalent radii of the atoms, it is possible to determine which atoms are bonded to each other within the collection. To fine-tune this process, a bond length correction parameter is used. This parameter is user-defined and can be modified at any time. The default value is 1.3, meaning that two atoms are considered bonded if the distance between them is less than 1.3 times the sum of their covalent radii. This default value was established based on the transition state geometries of Claisen rearrangement reactions. Listing 4.1 shows the constructors of the *Atom* and *Molecule* classes. Note that while the *Atom* class can be instantiated using either the atomic number or the atomic symbol, the *Molecule* class is instantiated without any arguments.

Listing 4.1: Creating a Atom/Molecule Object

```
Atom::Atom(int atomicNumber, double x, double y, double z, double charge, bool freezeCode_){
    PeriodicTable temp;
    this->atomicNumber = atomicNumber;
    this->atomicSymbol = temp.getSymbol(this->atomicNumber);
    this->point = Point(x, y, z, 'c');
    this->charge = charge;
    this->freezeCode = freezeCode_;
```

```
        this->atomicMass = temp.getAtomicMass(this->atomicSymbol);
        this->atomicRadio = PeriodicTable().getCovalentRadii(this->atomicSymbol);
        this->opls = "None";
    };
    Atom::Atom(string atomicSymbol, double x, double y, double z, double charge, bool freezeCode_){
        PeriodicTable temp;
        string symbol(atomicSymbol);
        this->atomicSymbol = symbol;
        this->atomicNumber = temp.getAtomicNumber(atomicSymbol);
        this->point = Point(x, y, z, 'c');
        this->charge = charge;
        this->freezeCode = freezeCode_;
        this->atomicMass = temp.getAtomicMass(this->atomicSymbol);
        this->atomicRadio = PeriodicTable().getCovalentRadii(this->atomicSymbol);
        this->opls = "None";
    };
    Molecule::Molecule(){
        this->molecule = AtomList();
        this->multiplicity = 1;
        this->VDWRatio = 1.3;
        this->charge = 0;
    };
```

4.3.1 Internal Redundant Coordinates

Generally the spatial position of atoms in a molecule is described by the Cartesian coordinates, however expression this positons in a non-constrined way, like in a Z-matrix, can be more eficient when dealing with geometrical parameters[95,96]. The internal redundant coordinates (IRC) are a set of coordinates that describe the molecular geometry in terms of bond lengths, bond angles, and dihedral angles. These coordinates are independent of the molecular orientation and can be used to describe the molecular geometry in a more intuitive way. The *MoleKing* package contains a method called *doIRC* that allows the user to convert between Cartesian and internal redundant coordinates. Listing 4.2 shows the constructors of the *IRC* class.

Listing 4.2: Obtaining Bond length, Angles and Dihedrals

```
    void Molecule::doIRC(){
        this->bonds.clear();
        this->angles.clear();
        this->dihedrals.clear();
        this->getBonds();
        this->getAngles();
        this->getDihedrals();
    };
    void Molecule::getBonds(){
        string symbol1, symbol2;
```

```
    for (int i = 0 ; i < (int) this->molecule.size(); i++){
        for (int j = i; j < (int) this->molecule.size(); j++){
            double length = this->bondLength(i, j);
            symbol1 = this->molecule[i].getAtomicSymbol();
            symbol2 = this->molecule[j].getAtomicSymbol();
            PeriodicTable table = PeriodicTable();
            double radii = this->VDWRatio * (table.getCovalentRadii(symbol1) +
table.getCovalentRadii(symbol2));
            if (length <= radii){
                if (i != j){
                    StraightSegment bond = StraightSegment(this->molecule[i].getPoint(),
this->molecule[j].getPoint());
                    this->bonds.push_back(pair < vector <int> , StraightSegment > {vector
<int> {i,j}, bond});
                };
            };
        };
    };
};
```

Here (Listing 4.2), every atom pair in the molecule has its minimal distance calculated, and if this distance is less than the sum of the covalent radii of the atoms times the bond length correction parameter, the atoms are considered bonded. The bond length is then stored in a vector of pairs, where the first element is a vector of integers representing the atom indexes and the second element is the bond length. Once the bonded atoms are known, all angles and dihedrals can be calculated using shperical coordinates.

$$
\begin{aligned}
x &= r\sin\theta\cos\phi \\
y &= r\sin\theta\sin\phi \\
z &= r\cos\theta
\end{aligned}
\tag{4.2}
$$

An advantage of using internal redundant coordinates is that once the bond lengths are defined, all geometrical parameters for the molecule are readly available. When dealing with OEEF optimization in a theoretical manner Gaussian requires the use of the Z-matrix representation. Therefor a conversion between the Cartesian and internal Z-matrix coordinates is shown in Listing 4.3. By ordering the molecule with two specific atoms at first, a bond alined Z-matrix is obtained.

Listing 4.3: Ordering the molecule for Z-Matrix

```
void Molecule::reorderMolecule(vector <int> fixedAtoms){
    if (fixedAtoms.size() == 0)
    {
        vector <int> temp;
        vector <double> distances;
```

```
            vector <double> atom1 = this->molecule[0].getPos();

            for (int i = 1; i < (int) this->molecule.size(); i++){
                vector <double> atom2 = this->molecule[i].getPos();
                distances.push_back(Vector3D(atom1, atom2).magnitude());
            }
            vector <double> distancesCopy = distances;
            sort(distances.begin(), distances.end());
            for (int i = 0; i < (int) distances.size(); i++){
                for (int j = 0; j < (int) distancesCopy.size(); j++){
                    if (distances[i] == distancesCopy[j]){
                        temp.push_back(j+1);
                        distancesCopy[j] = -1;
                        break;
                    }
                }
            }
            AtomList tempMolecule;
            tempMolecule.push_back(this->molecule[0]);
            for (int i = 0; i < (int) temp.size(); i++){
                tempMolecule.push_back(this->molecule[temp[i]]);
            }
            this->molecule = tempMolecule;
        }
        else if (fixedAtoms.size() == 2)
        {
            vector<pair<double, int>> distances;
            vector<double> atom1 = this->molecule[fixedAtoms[0]].getPos();
            for (int i = 0; i < (int)this->molecule.size(); i++)
            {
                if (i != fixedAtoms[0] && i != fixedAtoms[1])
                {
                    vector<double> atom2 = this->molecule[i].getPos();
                    distances.push_back({Vector3D(atom1, atom2).magnitude(), i});
                }
            }
            sort(distances.begin(), distances.end());
            AtomList tempMolecule;
            tempMolecule.push_back(this->molecule[fixedAtoms[0]]);
            tempMolecule.push_back(this->molecule[fixedAtoms[1]]);
            for (const auto &pair : distances)
            {
                tempMolecule.push_back(this->molecule[pair.second]);
            }
            this->molecule = tempMolecule;
        }
    };
```

4.3.2 Spatial Manipulation

During a theoretical investigation of a chemical reaction, it is common to have molecular movements in the Cartesian space. To represent these movements, the *MoleKing* package makes use of the rotational and translational matrices. MoleKing uses the Rodrigues'[97,98] rotation formula to rotate the molecule around an arbitrary axis. The rotation matrix is defined by Equation 4.3, as shown in Listing 4.4.

$$R = \begin{bmatrix} \cos\theta + u_x^2(1-\cos\theta) & u_x u_y(1-\cos\theta) - u_z\sin\theta & u_x u_z(1-\cos\theta) + u_y\sin\theta \\ u_y u_x(1-\cos\theta) + u_z\sin\theta & \cos\theta + u_y^2(1-\cos\theta) & u_y u_z(1-\cos\theta) - u_x\sin\theta \\ u_z u_x(1-\cos\theta) - u_y\sin\theta & u_z u_y(1-\cos\theta) + u_x\sin\theta & \cos\theta + u_z^2(1-\cos\theta) \end{bmatrix} \tag{4.3}$$

Listing 4.4: Rotating the Molecule

```
void Point::rotationVector(double angle, Vector3D unitVector){
    angle = M_PI * angle / 180;
    double x_u = unitVector.axisValue(’i’);
    double y_u = unitVector.axisValue(’j’);
    double z_u = unitVector.axisValue(’k’);
    vector < vector < double> > posMatrix= { {this->x}, {this->y}, {this->z}, {1.0} };

    Matrix rotMatrix = Matrix( { { cos(angle) + pow(x_u, 2)*(1 - cos(angle)), y_u * x_u * (1 - cos(angle)) - z_u * (sin(angle)), z_u * x_u * (1 - cos(angle)) + y_u * (sin(angle)), 0.0},
                                 { x_u * y_u * (1 - cos(angle)) + z_u * (sin(angle)), cos(angle) + (1 - cos(angle)) * pow(y_u, 2), z_u * y_u * (1 - cos(angle)) - x_u * (sin(angle)), 0.0},
                                 { x_u * z_u * (1 - cos(angle)) - y_u * sin(angle), y_u * z_u * (1 - cos(angle)) + x_u * sin(angle), cos(angle) + (1 - cos(angle)) * pow(z_u, 2), 0.0},
                                 {0.0, 0.0, 0.0, 1.0} } );

    Matrix newPos = rotMatrix.multiplication(posMatrix);
    this->x = newPos.element(1, 1);
    this->y = newPos.element(2, 1);
    this->z = newPos.element(3, 1);
    vector <double> newPosSpherical = SphericalCoords(this->x, this->y, this->z, ’c’).toSpherical();
    this->radius = newPosSpherical[0];
    this->tetha = newPosSpherical[1];
    this->phi = newPosSpherical[2];
};
```

Translation is handled in an analogous manner. By using homogeneous coordinates, the translation can be performed through a simple multiplication of the position vector by the translation matrix. The translation operation is represented by Equation 4.4:

$$\begin{bmatrix} x' \\ y' \\ z' \\ 1 \end{bmatrix} = \begin{bmatrix} 1 & 0 & 0 & t_x \\ 0 & 1 & 0 & t_y \\ 0 & 0 & 1 & t_z \\ 0 & 0 & 0 & 1 \end{bmatrix} \begin{bmatrix} x \\ y \\ z \\ 1 \end{bmatrix} = \begin{bmatrix} x+t_x \\ y+t_y \\ z+t_z \\ 1 \end{bmatrix} \tag{4.4}$$

4.3.3 Molecular axis

Another key point of the uses of MoleKing in handling external effects is the definition of the molecular axis. The molecular axis is defined as the vector that connects the two atoms that are farthest apart in the molecule. A principal component analysis (PCA) is performed to determine the molecular axis. The PCA is a statistical method that uses an orthogonal transformation to convert a set of observations of possibly correlated variables into a set of linearly uncorrelated variables called principal components. The first principal component is the vector that maximizes the variance of the data, and it is used to define the molecular axis. The PCA is performed by calculating the covariance matrix of the molecule and then finding the eigenvectors and eigenvalues of this matrix. The eigenvector with the largest eigenvalue is the first principal component, which defines the molecular axis. Listing 4.5 shows the PCA method implemented in *MoleKing*, here the Eigen3 library is used to calculate the eigenvectors and eigenvalues of the covariance matrix, Eigen3 is the only non standard library used in *MoleKing*.

Listing 4.5: Principal Component Analysis of Molecular Axis

```
void Molecule::alignMolecule(char axis){

    Eigen::MatrixXd coords(this->molecule.size(), 3);

    for (size_t i = 0; i < this->molecule.size(); ++i)
    {
        coords.row(i) = Eigen::Vector3d(this->molecule[i].getX(), this->molecule[i].getY(), this->molecule[i].getZ());
    }

    //perform PCA

    Eigen::SelfAdjointEigenSolver<Eigen::MatrixXd> solver(coords.transpose() * coords);
    Eigen::MatrixXd principalAxis = solver.eigenvectors().col(2);  // The principal axis is the eigenvector with the largest eigenvalue
    Eigen::Matrix3d rotationMatrix = Molecule::getRotationMatrix(principalAxis, axis);

    for (size_t i = 0; i < this->molecule.size(); ++i)
    {
```

```
            Eigen::Vector3d pos = Eigen::Vector3d(this->molecule[i].getX(), this->molecule[i].getY(), this->molecule[i].getZ());
            pos = rotationMatrix * pos;
            this->molecule[i].setX(pos(0));
            this->molecule[i].setY(pos(1));
            this->molecule[i].setZ(pos(2));
        }

        this->moveMassCenter(0,0,0);
    };
```

4.3.4 Gaussian File Handling in *MoleKing*

The *MoleKing* package is designed to efficiently read and write Gaussian output and input files. The process begins with reading Gaussian output files (`.log`) line by line, with each line stored in a `vector<string>`. This approach allows for efficient parsing of large files, enabling quick data retrieval without significant memory overhead.

The parsing process extracts key computational data such as:

- *Atomic Coordinates:* Extracted from the standard orientation section for geometry analysis.
- *SCF Energy:* Retrieved from lines containing `SCF Done:` to monitor energy convergence.
- *Molecular Orbitals (HOMO/LUMO):* Identified from orbital energy sections for electronic structure analysis.
- *Dipole Moments:* Parsed from the `Dipole moment` block, providing components in the x, y, and z directions.
- *TD-DFT Transitions:* Extracted for excited-state calculations, including transition energies and oscillator strengths.
- *NLO Properties* Extrac the NLO tensors separating then by frequency and orientation.

For writing Gaussian input files (`.gjf`), *MoleKing* constructs the file line by line, storing the content in a `vector<string>` before outputting it to disk using the `ofstream` class. This approach ensures compatibility with Gaussian input syntax and enables the automated generation of new input files from parsed data.

While the overall syntax for input/output handling is simple, the underlying implementation is extremely intricate and convoluted. Therefore, no code will be presented in this section.

Chapter 5

Results and Discussion

5.1 MoleKing: A Python Module for Theoretical Chemistry.

One of the main goals of this thesis was to develop a Python module, *MoleKing*, designed to simplify coding for chemical calculations. A common challenge faced by individuals new to programming is understanding that computers lack any form of common sense; every instruction must be explicitly defined, leaving little room for ambiguity. This can be both time-consuming and error-prone, particularly when adapting complex systems, such as molecules, to machine-readable logic.

To address these challenges, the *MoleKing* module was developed to incorporate chemical logic directly into computational workflows, streamlining the process of writing code for theoretical chemistry applications. *MoleKing* is a versatile tool designed for a wide range of tasks, including molecular geometry manipulation, quantum chemistry data parsing, and automation of computational workflows.

Figure 5.1: The *MoleKing* logo.

The module is available for download at GitHub, where the latest version, while the documentation and usage examples, can be accessed via the MK User Guide. The module is also readily available on the Python Package Index (PyPI) and can be installed using the command `pip3 install MoleKing`. While *MoleKing* is adaptable to various theoretical chemistry applications, it is particularly recommended for:

- Automating the parsing of Gaussian output files for energy, dipole moments, and orbital information.
- Handling molecular geometry transformations, including rotations, translations, and coordinate conversions.
- Integrating with QM/MM workflows, especially for managing point charges and external field effects.
- Simplifying the generation of Gaussian input files for batch processing.

While working on the present study of the Hurd-Claisen rearrangement, *MoleKing* was employed in nearly all stages of the computational workflow, from the initial geometry manipulation to the final parsing of the results. The module proved particularly useful in automating the OEEF (Oriented External Electric Field) calculations, as it facilitated the reorientation of molecules along both the reaction axis and the molecular axis. Additionally, it handled the point charges generated during the S-QM/MM solvation process with ease. More detailed information can be found in the *MoleKing* section of the Methodology chapter. the Listing below shows an example of the code used to generate the input files for the OEEF calculations, using the reaction axis rule to orient the molecule central $C-O$ bond along the z-axis:

Listing 5.1: Generating Gaussian input files for OEEF

```python
from MoleKing import G16LOGfile
from sys import argv
from os import chdir, mkdir
referenceMol = argv[-1]
print(referenceMol)
mymol = G16LOGfile(referenceMol).getMolecule()
fields = [0, 2e-3, 4e-3, 6e-3, 8e-3]
axis = ['x', 'y', 'z']
mymol.alignBond(0,4,'y')
mkdir(referenceMol.split('.')[0]+'_EField')
chdir(referenceMol.split('.')[0]+'_EField')
for i in range(len(fields)):
    efield_p = [0.0, 0.0, fields[i]]
```

```
        efild_m = [0.0, 0.0, -1*fields[i]]
        fields_name = str(int(fields[i]*10000))
        P = mymol.copy()
        M = mymol.copy()
        if i==0:
            fields_name = ’0’
            P.toGJF(fileName=’0’+axis[2]+’_’+referenceMol.split(’.’)[0]+’_ZA.gjf’,
    method=’M062X’, basis=’6-311+G(d,p)’,
    addKeywords=’opt=(zmatrix,calcfc,ts,maxcycle=100000,noeigentest) freq=noraman
    int=(grid=ultrafine) density=current test NoSymm’, charge=0, multiplicity=1, zmatrix=True,
    bondFixer=[0,4])
        else:
            P.toGJF(fileName=’p’+fields_name+axis[2]+’_’+referenceMol.split(’.’)[0]+’_ZA.gjf’,
    method=’M062X’, basis=’6-311+G(d,p)’,
    addKeywords=’opt=(zmatrix,calcfc,ts,maxcycle=100000,noeigentest) freq=noraman
    int=(grid=ultrafine) density=current test NoSymm’, charge=0, multiplicity=1, zmatrix=True,
    bondFixer=[0,4], EField=efield_p)
            M.toGJF(fileName=’m’+fields_name+axis[2]+’_’+referenceMol.split(’.’)[0]+’_ZA.gjf’,
    method=’M062X’, basis=’6-311+G(d,p)’,
    addKeywords=’opt=(zmatrix,calcfc,ts,maxcycle=100000,noeigentest) freq=noraman
    int=(grid=ultrafine) density=current test NoSymm’, charge=0, multiplicity=1, zmatrix=True,
    bondFixer=[0,4], EField=efild_m)
    chdir(’..’)
```

This section will now provide a brief overview of some of the module’s applications during the development of this thesis.

While the focus of this study was the application of point charges as a means of simulating the electrostatic effects of solvents, the *MoleKing* module is also capable of handling other types of point charges, such as those generated by the supramolecular model for crystalline representation.[72,73] This methodology employs an iterative process to account for the effects of the polarized medium on the electrical properties of molecular crystals. The point charge embedding approach enhances the simulation of the crystal environment by generating the correct crystalline electrostatic Coulomb potential. The electrostatic crystal potential experienced by each atom in a molecule within the infinite crystal lattice is simulated using a finite, self-consistently derived array of point charges.[72]

During the development of a study on the effects of an electrostatic crystalline environment on a stilbazolium derivative (VSNS), the module was utilized to generate input files for Gaussian calculations and to parse the output files, extracting the Non-Linear Optical (NLO) properties of the crystal. By employing HF (Hartree-Fock) titration alongside the point charges, it was possible to achieve a systematic ordering of excitation energies and oscillator strengths, significantly improving the precision of the calculations.

The following listing shows an example of the code used to extract the NLO properties from the Gaussian output files:

Listing 5.2: Extracting NLO properties from Gaussian output files using MoleKing.

```python
from MoleKing import G16LOGfile
from pandas import DataFrame
from sys import argv
class NLO:
    def __init__(self, filename):
        self.VSNS = G16LOGfile(filename, polarAsw=True)
    def getNLO(self):
        F = self.VSNS.getFrequency()
        Beta = {}
        for i in F:
            if i != 0.0:
                Beta.update({i:self.VSNS.getBeta(orientation=’Input’, frequency=i, unit=’esu’, BSHG=1)})
        df = DataFrame(Beta)
        df.sort_index(axis=1, inplace=True)
        df.to_csv(’Beta.csv’, sep=’,’)
if __name__ == ’__main__’:
    nlo = NLO(argv[1])
    nlo.getNLO()
```

During the development of the work on the Hurd-Claisen rearrangement by Oliveira,[19] the fragmentation protocol proposed by Silva[17] was extended to other substituents in both ester-containing and nitrile-containing molecules. The *MoleKing* module was used to simplify the fragmentation process, which was performed using the following code:

Listing 5.3: Partial Fragmentation of the Hurd-Claisen rearrangement using MoleKing.

```python
from MoleKing import Molecule, G16LOGfile, PeriodicTable
def LOG_to_molecule(self):
    Mol = Molecule()
    mol = G16LOGfile(arq).getMolecule()
    for atom in mol:
        Mol.addAtom(self.PT.getSymbol(int(atom.getAtomicSymbol())), atom.getX(), atom.getY(), atom.getZ())
    return Mol
def Get_bonds(self):
    b = self.mol.getIRCBonds()
    while [] in b:
        b.remove([])
    return b
def list_bonds(self, atom):
    bond_list = []
    for bond in self.bonds:
        if atom == bond[0]:
            bond_list.append(bond[1])
        elif atom == bond[1]:
```

```
                bond_list.append(bond[0])
        bond_atoms = [self.mol[x].getAtomicSymbol() for x in bond_list]
        return bond_list, bond_atoms
        (...)
```

By using the *MoleKing* module to detect the bonds between atoms, it was possible to fragment the molecule into smaller parts based on the presence of a common fragment known as the bridge. The bridge is the fragment that connects the two major parts of the molecule, allowing the molecule to be systematically divided into three key components: the Hurd group, the Electron Withdrawing Group (EWG), and the substituent group.

As showcased in the examples above, the use of the *MoleKing* module simplified the code, making it more readable and easier to maintain. Additionally, it significantly reduced the time required for code development, as the module provides built-in functions necessary for performing a wide range of tasks commonly encountered in theoretical chemistry workflows. Moreover, *MoleKing*'s modular design allows for easy integration into existing computational workflows, making it a valuable tool for automating repetitive tasks in quantum chemistry simulations.

5.2 Oriented External Electric Field

As stated in the Methodology chapter, the effect of the OEEF on the Hurd-Claisen rearrangement was investigated using two relative orientations. In the first case, the *reaction axis* of the transition state was aligned with the z-axis, and the external electric field was applied along the Cartesian z-axis. In the second case, the *molecular axis* was aligned with the z-axis, and the external electric field was applied along all three Cartesian axes.

A simple way to evaluate the geometric changes in the transition state is through the Root Mean Square Deviation of Atomic Positions (RMSD), which quantifies the differences between atomic positions of the transition state under varying OEEF conditions. The results indicate that larger OEEF magnitudes leads to greater structural changes, confirming that the OEEF significantly influences the transition state geometry.

As a side note, while RMSD values were occasionally mentioned throughout this discussion, to avoid excessive data proliferation, these results have been mostly compiled separately in Appendix A.1.

5.2.1 Reaction Axis Orientation

Figure 5.2 illustrates the effect of the OEEF ranging from -8.00×10^{-3} to 8.00×10^{-3} a.u. on the CH_3 Hurd-Est rearrangement for both E and Z isomers. By analyzing the general trends in both graphs, it is clear that both orientations of the OEEF lead to the stabilization of the TS structure.

This stabilization follows the trend described by Wang for the Diels-Alder reaction,[16] where the OEEF can significantly lower the activation barrier. Typically, it is expected that only one orientation of the OEEF would result in a stabilization; however, in the case of the Hurd-Est rearrangement, the electron flow occurs in both directions, the breaking of the $C-O$ bond and the formation of the $C-C$ bond, whitch are parallel to the reaction axis. Consequently, it is natural that both, the positive and negative, OEEF orientations lead to a stabilization.

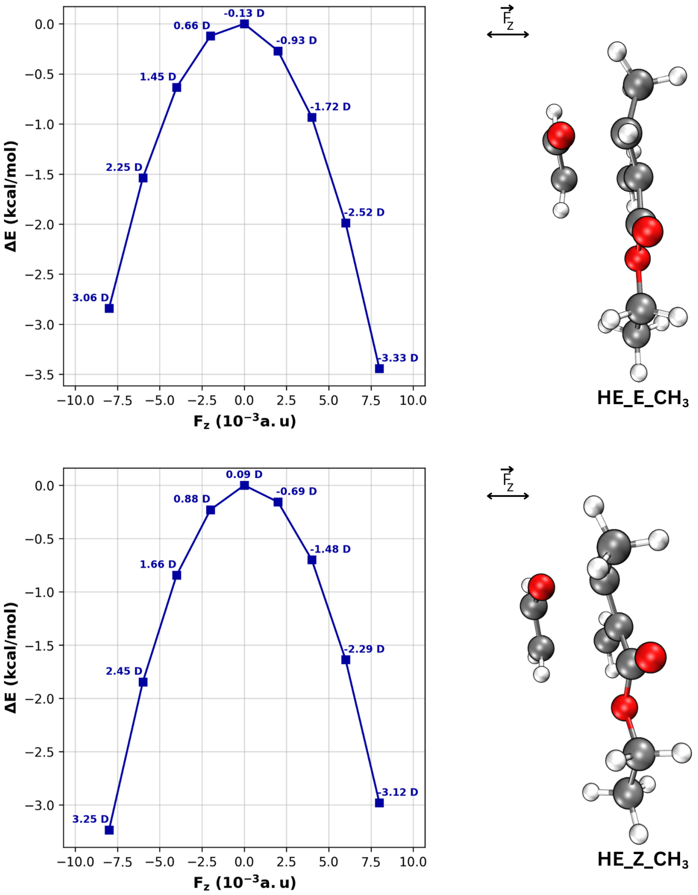

Figure 5.2: OEEF effect in relative energy and the $\hat{k}$ component of the dipole moment for the CH_3 Hurd-Est rearrangement ranging from -8.00×10^{-3} to 8.00×10^{-3} a.u. For the E (above) and Z (below) isomers.

Another point of interest is the asymmetric behavior observed in the E isomer. While the Z isomer shows no preference for any specific orientation of the OEEF, with a stabilization of approximately 3.2 kcal/mol, the E isomer exhibits a clear preference for the positive orientation, resulting in a stabilization of 3.58 kcal/mol. In contrast, the stabilization under the negative orientation is 2.72 kcal/mol, leading to a difference of 28% between the two.

Analyzing the changes in bond length for the reactive $C{-}C$ and $C{-}O$ bonds, we observe that the effect on both is symmetrical and equivalent for both isomers, with both bonds lengthening as the OEEF increases. As observed in Figure 5.3, under an OEEF, bond polarization occurs when the electron cloud of the bond is distorted, often increasing both the partial charges (q) and the bond length.

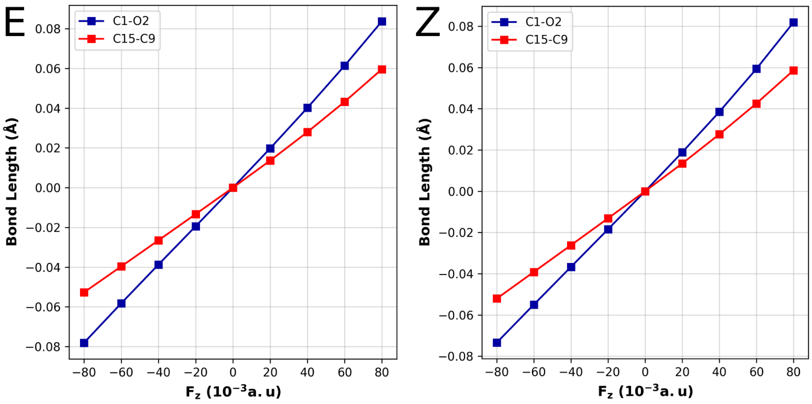

Figure 5.3: OEEF effect in the reactive bonds of the $CH3$ Hurd-Est rearrangement ranging from -8.00×10^{-3} to 8.00×10^{-3} a.u. The numbered atoms represent the order in which the atom appears on Gaussian Z-Matrix. The $C-O$ bond is the one that breaks, and the $C-C$ bond is the one that forms.

This symmetry suggests that the asymmetric behavior observed in the E isomer is not attributed to bond length but rather to the electronic distribution within the molecule. As expected, the $\hat{k}$ component of the dipole moment follows the same trend as the OEEF (see Figure 5.2). Notably, in the EQ stereoisomer (corresponding to the previously mentioned Z isomer), the dipole moment ranges from -3.186 to 3.195 a.u., whereas in the AX stereoisomer (E), it varies from -3.405 to 3.002 a.u.

This observation underscores a crucial distinction: the Z isomer exhibits symmetrical behavior under the external electric field, while the E isomer displays a clear asymmetry. This asymmetry arises from the dipole-field interaction, as described by Equation 3.54.

A similar behavior is observed in the $Et/SProp$ Hurd-Est rearrangements, as shown in Figures 5.4 and 5.5. The E isomer displays a clear preference for the positive orientation of the OEEF, with a stabilization of 3.88/4.21 kcal/mol—33%/18% higher than that observed for the negative orientation. Now, the Z isomer exhibits a slight preference for the negative orientation of the OEEF; however, this preference is considerably less pronounced than that of the E isomer.

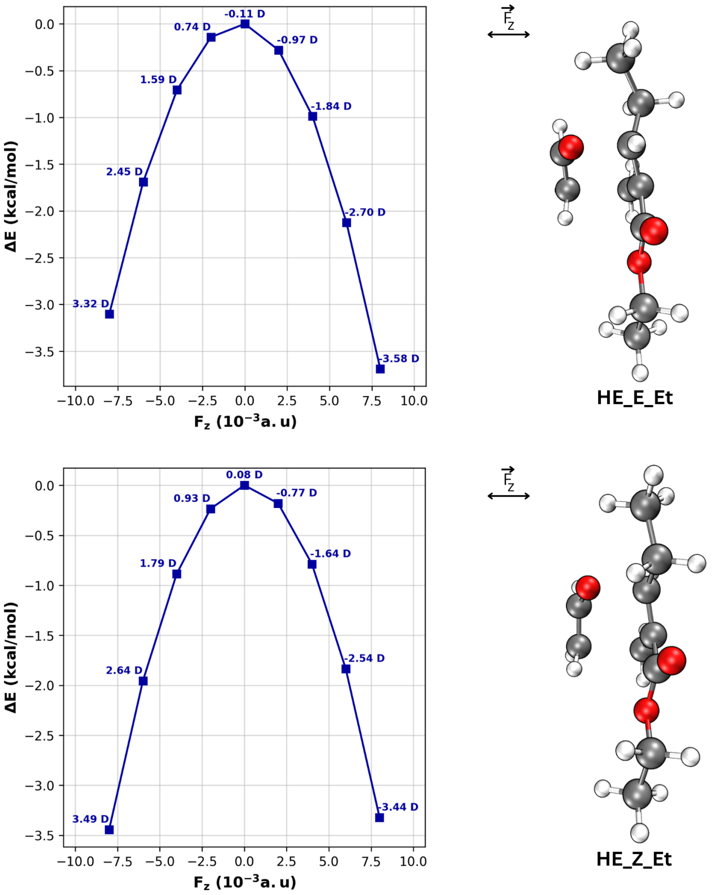

Figure 5.4: EEF effect in relative energy and the $\hat{k}$ component of the dipole moment for the Et Hurd-Est rearrangement ranging from -8.00×10^{-3} to 8.00×10^{-3} a.u. For the E (above) and Z (below) isomers.

This general trend of the E isomer showing a preference for the positive orientation of the OEEF leads to the expectation that the AX-stereoselectivity will be favored by a positive OEEF aligned with the reaction axis. The changes on bond length of the $C-C$ and $C-O$ bonds are numerically equivalent to those observed in the CH_3 Hurd-Claisen rearrangement, there for we will not present them here.

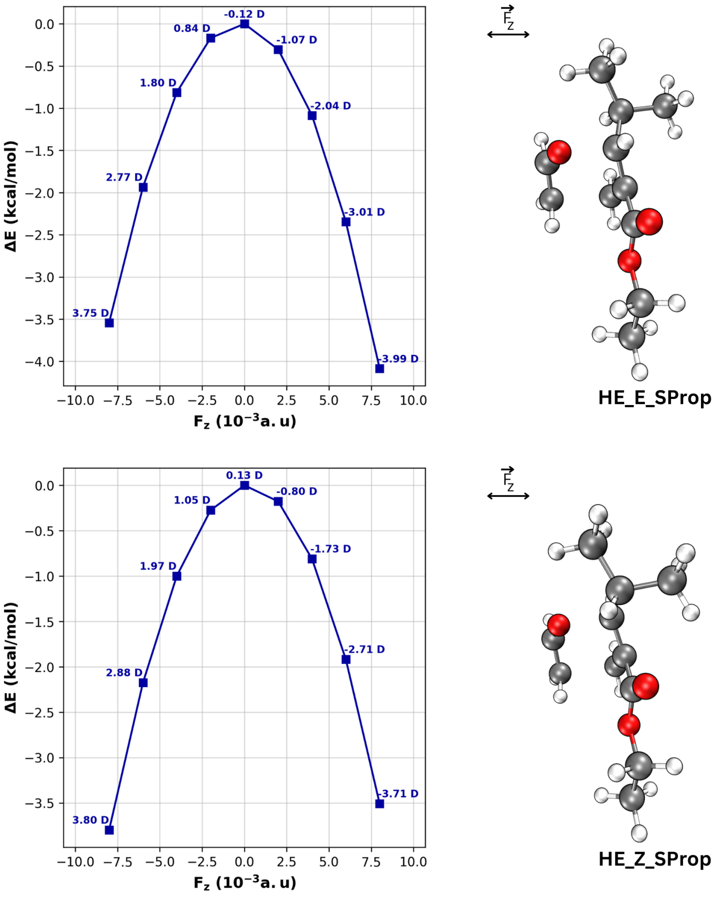

Figure 5.5: EEF effect in relative energy and the $\hat{k}$ component of the dipole moment for the *SProp* Hurd-Est rearrangement ranging from -8.00×10^{-3} to 8.00×10^{-3} a.u. For the *E* (above) and *Z* (below) isomers.

Here, we once again demonstrate the direct impact of the electric field on the dipole moment of the molecule. In a study on the effect of an oriented electric field on the oxidation of methane catalyzed by Mn-corrolazine, Xiangqian Wang[99] showed that an electric field can invert the dipole moment of a molecule, resulting in bidirectional stabilization of the transition state. A similar phenomenon is observed here, where the dipole-field interaction is the primary driver of transition state stabilization.

Turning to the highly sterically hindered isopropyl and tert-butyl substituents, where the corresponding results are shown in Figures 5.6 and 5.7. In contrast to the general trend—where positive fields typically stabilize the preferred isomer—the negative field here promotes greater stabilization for both isomers in the *TBut* reaction. And more, the *Z-IsoButyl* rearrangement exhibits a preference under a positive field, further deviating from the expected pattern.

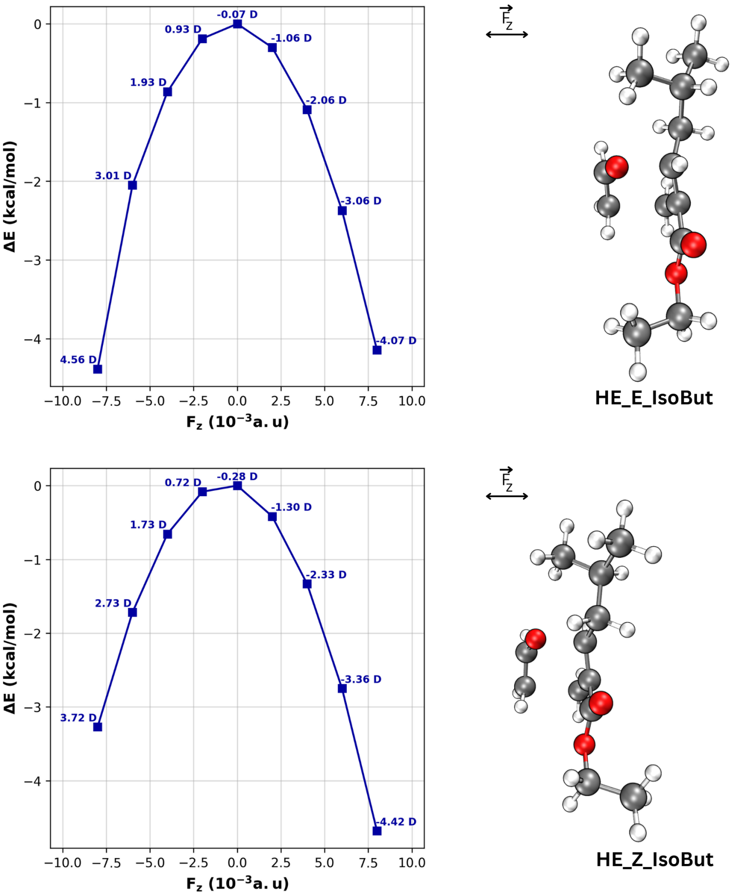

Figure 5.6: EEF effect in relative energy and the $\hat{k}$ component of the dipole moment for the *IsoBut* Hurd-Est rearrangement ranging from -8.00×10^{-3} to 8.00×10^{-3} a.u. For the *E* (above) and *Z* (below) isomers.

Despite these deviations, the overall asymmetrical stabilization observed in both field directions remains present. These findings suggest that in systems with bulky substituents, steric effects may begin to outweigh electronic contributions, leading to more complex and less predictable OEEF responses.

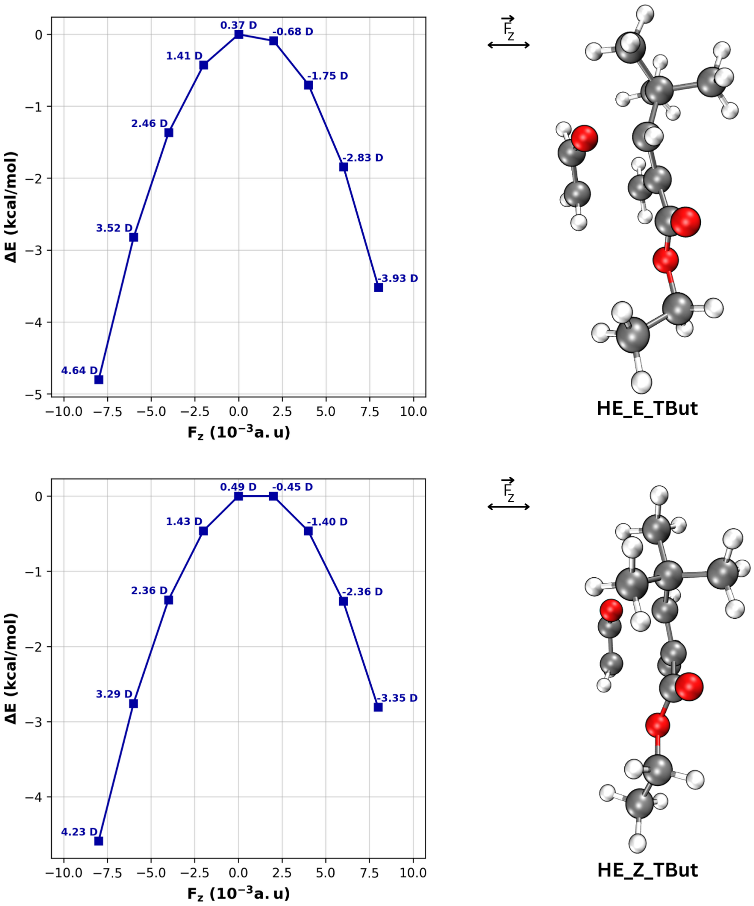

Figure 5.7: EEF effect in relative energy and the $\hat{k}$ component of the dipole moment for the $TBut$ Hurd-Est rearrangement ranging from -8.00×10^{-3} to 8.00×10^{-3} a.u. For the E (above) and Z (below) isomers.

By using the GoodVibes python package[100], the Gibbs free energy with the Grimme quasi-harmonic approximation was calculated for alkyl substituted Hurd-Est rearrangement. Some of theese results are shown in Figure 5.8, alongside a stabilization comparison of both isomers.

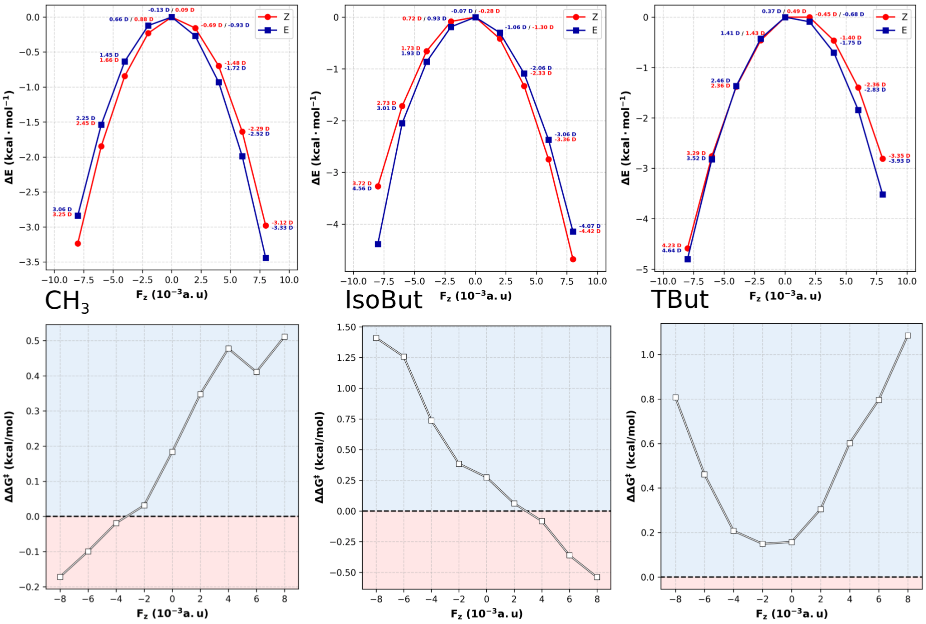

Figure 5.8: $\Delta\Delta G^{\ddagger}$ (down) and energy stabilization (up) for the CH_3 (left), $IsoBut$ (middle) and $TBut$ (right) Hurd-Est rearrangement, calculated with the Grimme quasi-harmonic approximation via GoodVibes in $373k$ at M062X/def2tzvpp level of theory. The red zone represent the region of the Gibbs free energy where the Z isomer is more stable than the E isomer.

As presented, the Z/E ratio can be estimated by the difference in the Gibbs free energy of the transition states of the Z and E isomers. A negative value for this difference indicates that the Z isomer is more stable than the E isomer.

The CH_3 and $IsoBut$ Hurd-Est rearrangements show a general preference for the E isomer; however, applying a proper oriented OEEF (positive for $IsoBut$ and negative for CH_3) along the reaction axis stabilizes the Z isomer, making it more favorable. In contrast, the $TBut$ Hurd-Est rearrangement consistently favors the E isomer, regardless of the OEEF orientation.

The energy stabilization comparison (Figure 5.8, upper portion) demonstrates that while both field orientations stabilize the transition states, the magnitude of stabilization differs between the E and Z isomers. Generally, the Z isomer is strongly stabilized by the negative OEEF, whereas the E isomer experiences greater stabilization under the positive OEEF. Thus, the orientation of the OEEF along the reaction axis serves as an effective tool for controlling the stereoselectivity of reactions involving transition states with similar energies. Specifically, a negative OEEF can invert the stereoselectivity of some alkyl-substituted Hurd-Est rearrangements.

The consistency of these trends across the studied alkyl substituents suggests that the OEEF interaction depends primarily on the electronic distribution of the molecule rather than on substituent size. The *Et* and *SProp* rearrangements produced results similar to those of the methyl group and were therefore relegated to an appendix.

To further investigate this effect, an additional class of substituents was analyzed: the aryl groups (*Ph*, NO_2Ph and NH_2Ph,), which exhibit the unprecedented stereoselectivities previously observed by Silva. These substituents were chosen due to their high dipole moment and high polarizability, which is expected to lead to a more pronounced interaction with the OEEF.

Figure 5.9 presents the results for the stabilization energy and $\Delta\Delta G^{\ddagger}$ of the aryl Hurd-Est rearrangements. A striking difference is observed in the response of the NO_2Ph transition state to a low positive electric field: both isomers exhibit a destabilization of approximately 0.5 kcal/mol. The high polarization of this system imposes a barrier to dipole moment reorientation, resulting in an unfavorable dipole-field interaction within this initial range of field strengths, thereby explaining the observed increase in energy. The same effect is observed for the NH_2Ph rearrangement, but to a lesser degree.

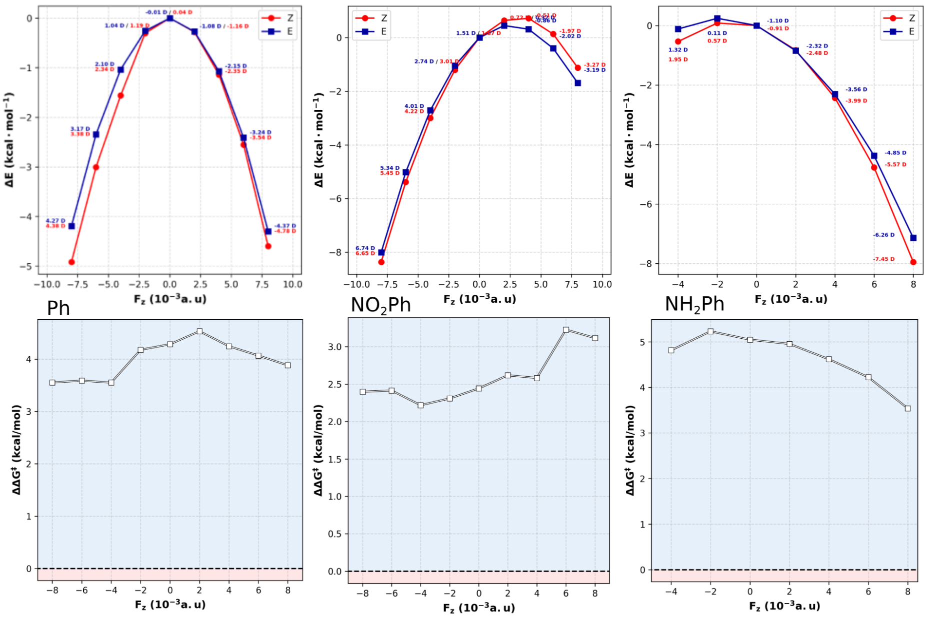

Figure 5.9: $\Delta\Delta G^{\ddagger}$ (down) and energy stabilization (up) for the *Ph* (left), NO_2Ph (middle) and NH_2Ph (right) Hurd-Est rearrangement, calculated with the Grimme quasi-harmonic approximation via GoodVibes in 373*k* at M062X/def2tzvpp level of theory. The red zone represent the region of the Gibbs free energy where the *Z* isomer is more stable than the *E* isomer.

The dipole polarizabilities for the CH_3 and aryl Hurd-Est rearrangements are shown in Table 5.1. The aryl substituents exhibit higher dipole polarizabilities than the alkyl groups, with the phenyl-based substituents showing a particularly large difference. This effect is likely due to the presence of amino groups, which are highly polarizable and can significantly influence the dipole moment of the molecule.

Table 5.1: Dipole moment for the NO_2Ph and CF_3 Hurd-Claisen rearrangements under no OEEF. This results were extracted from the M062X/def2tzvpp calculations.

Substituent	**Dipole polarizability Z/E (a.u.)**
CH_3	121.805 / 121.180
Ph	176.395 / 175.113
NO_2Ph	195.510 / 193.669
NH_2Ph	191.492 / 189.276

By comparing the polarizability values of the CH_3 and NO_2Ph systems, it is evident that a higher polarizability leads to a more pronounced interaction with the OEEF. Notably, for the same electric field of -8.00×10^{-3} a.u., the molecule with the greater dipole polarizability exhibits stronger stabilization.

Here, the application of a negative OEEF along the reaction axis leads to a preference for the EQ isomer. However, in this case, the stabilization of the AX stereoisomer under a positive field is not evident, suggesting that the use of invisible catalysis preferentially favors the EQ configuration. Furthermore, the differentiation induced by the electric field is not sufficient to invert the stereoselectivity, as the Gibbs free energy difference between the isomers remains positive.

Turning to the nitrile-containing Hurd-Nit rearrangement, the results are shown in Figure 5.11(B). Here, we highlight the data for the $SProp$ and $TBut$ substituents, as presented in Figure 5.10.

By examining the stabilization of the $SProp$ and $TBut$ isomers, we observe that the general trend of both-way stabilization is preserved. However, the electron-withdrawing nitrile group shifts the inherent selectivity from the E to the Z isomer.

A comparison between Figures 5.5 and 5.10 shows that the Hurd-Nit rearrangement is slightly more stabilized by the OEEF than the corresponding Hurd-Est system.

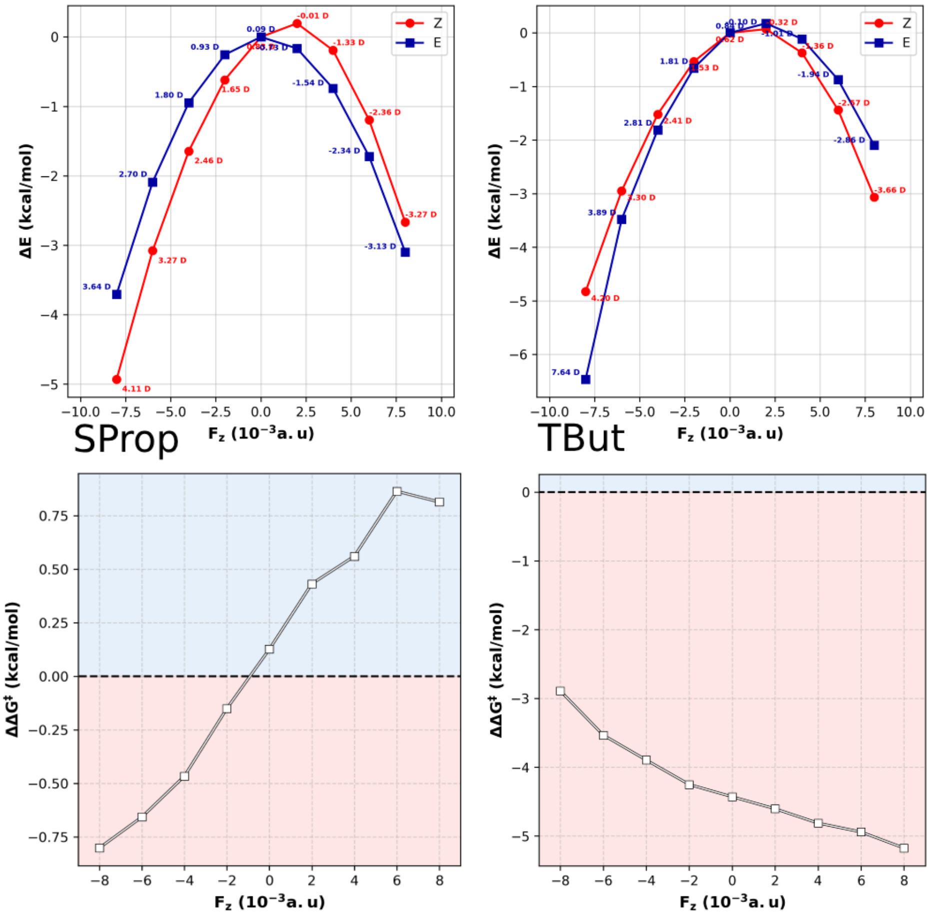

Figure 5.10: $\Delta\Delta G^{\ddagger}$ (down) and energy stabilization (up) for the *Sprop* (left) and *TBut* (right) Hurd-Nit rearrangement, calculated with the Grimme quasi-harmonic approximation via GoodVibes in 373*k* at M062X/def2tzvpp level of theory. The red zone represent the region of the Gibbs free energy where the *Z* isomer is more stable than the *E* isomer.

Further comparing both rearrangements, it is important to note that—with the exception of the tert-butyl system—all reactions maintained the same trends of stabilization as a function of the OEEF. This highlights the idea that the electron-withdrawing group (EWG) modifies only the intensity of the intramolecular electrostatic interactions, not their fundamental nature. As a result, the OEEF remains capable of controlling the stereoselectivity of reactions with indecisive barriers.

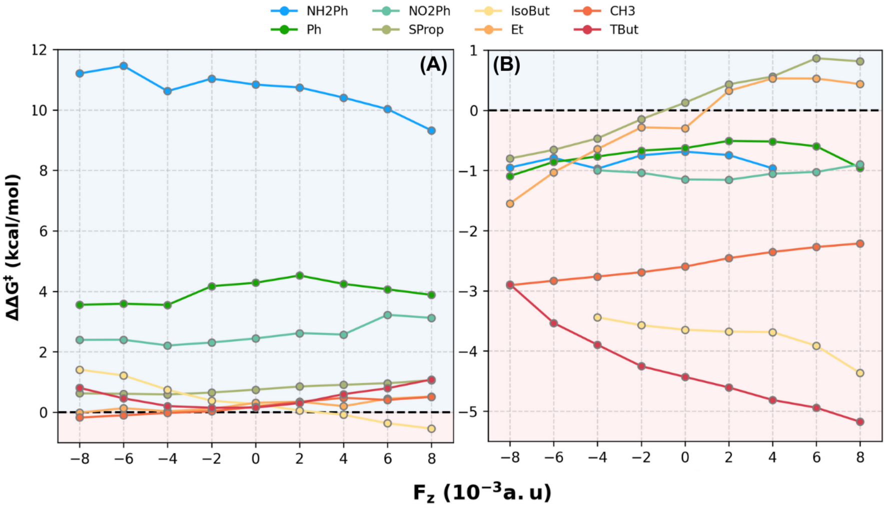

Figure 5.11: Gibbs free energy differences of transition states $\Delta\Delta G^{\ddagger}$ for (A), the Hurd-Est and (B) Hurd-Nit rearrangements. $\Delta\Delta G^{\ddagger}$ was calculated using Grimme's *quasi*-harmonic approximation at 373 K with the M06-2X/def2-TZVPP level of theory. The red-shaded region indicates where the Z isomer is favored over the E isomer.

Once again the geometrical parameters took a minor role in the stabilization of the transition state, with the bond length changes being similar to those observed in the Hurd-Est rearrangement, therefore the results are not shown here. This is consistent with the findings of Wang et al., who observed that the OEEF primarily affects the electronic distribution of the molecule, leading to a more pronounced dipole-field interaction.

5.2.1.1 OEEF on Reactants

While an in-depth analysis of the activation complexes is sufficient to characterize the stereoselectivity of the Hurd-Claisen rearrangement[19,85] even under the influence of an electric field, studying the reactants is essential to understanding the overall effect of a field on reaction rates. Therefore, the same OEEF applied to the transition state were also applied the CH_3, *Et* and *SProp* ester-containing reactants.

In this case, the molecular alignment was based on the $C-O$ bond to mimic the overall positioning of the non-reactive sites. The results are shown in Figure 5.12.

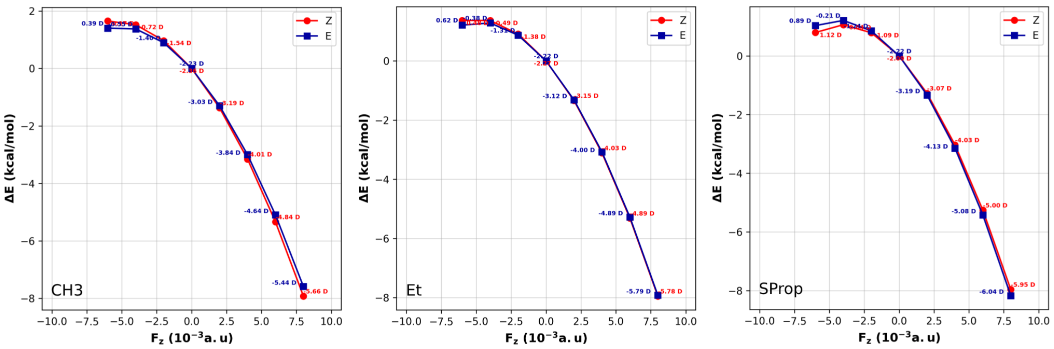

Figure 5.12: OEEF effect in the CH_3, *Et* and *SProp* Hurd-Est rearrangement ranging from -8.00×10^{-3} to 8.00×10^{-3} a.u. The energy of the field-free reactants was deducted from the energy of the OEEF-applied reactants.

Contrary to what is observed in the transition state, the stabilization of the reactants is unidirectional, with a negative OEEF leading to an increase in the energy of the reactants. The dipole moment components of the *SProp* Hurd-Claisen rearrangement, shown in Figure 5.13, shed light on the causes of this behavior. For both isomers, the negative field induces little to no change in the dipole moment, whereas the positive field leads to a significant increase in the $\hat{k}$ component, which enhances electrostatic stabilization.

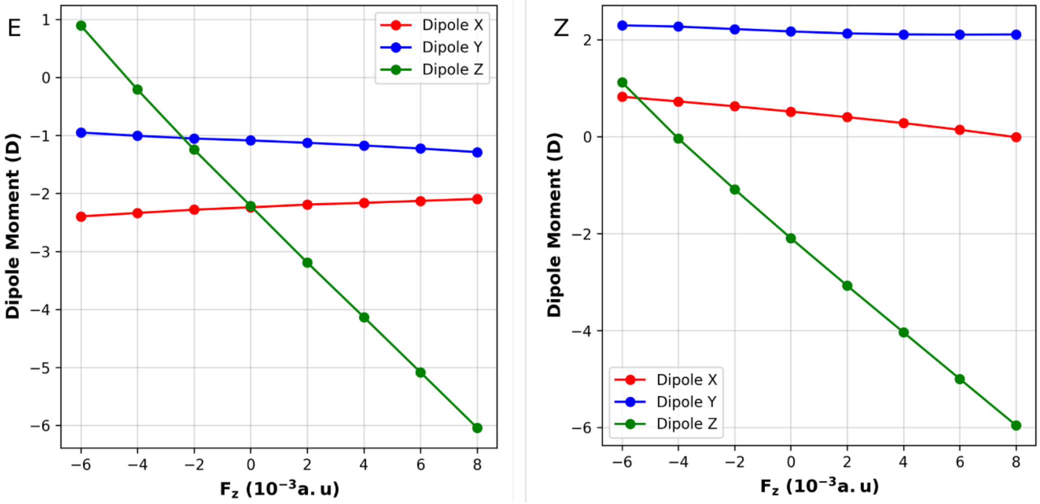

Figure 5.13: Components of the dipole moment of the *SProp* Hurd-Claisen in dependence with a OEEF ranging from -6.00×10^{-3} to 8.00×10^{-3} a.u. Aligned with the $C-O$ bond.

In the context of this stabilization, we can infer that while all studied alkyl transition states (TS) are stabilized by dipole-field interactions regardless of orientation, the unidirectional stabilization of the reactants suggests that a negative field will increase the reaction rate by lowering the energy barrier. Moreover, a positive field is expected to significantly reduce the reaction rate, as it decreases the energy of the reactants relative to the transition state. Therefore, although a reaction-axis-oriented OEEF can effectively control the stereoselectivity of the reaction, negative OEEFs are not capable of acting as catalysts, since they do not increase the relative energy of the reactants.

5.2.2 Molecular Axis Orientation

The OEEF was also applied along the molecular axis, with the molecule aligned to the z-axis. The results for both Hurd-Claisen rearrangements are shown in Figures 5.14 and 5.15. A key distinction between these rearrangements is the identity of the favored isomer: while the Hurd-Est rearrangement favors the E isomer, the Hurd-Nit rearrangement favors the Z isomer.

A quick glance at the general behavior of both rearrangements shows that the nitrile-containing system is more sensitive to the OEEF, displaying a differentiation of up to $2kcal \cdot mol^{-1}$ across multiple substituents. In contrast, for the Hurd-Est rearrangement, only the NO_2Ph substituent exhibited a differentiation of comparable magnitude.

As previously discussed, the primary contributor to energy changes in electric field interactions is the dipole-field interaction, with geometric changes playing a more passive role, usually manifesting as modifications to the molecular dipole moment. Therefore, since the results presented here do not account for geometric effects, the electronic interaction between the OEEF and the transition states can be categorized into two groups: E-stabilizing, where an increase in the OEEF leads to stabilization of the E isomer, and Z-stabilizing, where the Z isomer is stabilized as the OEEF increases.

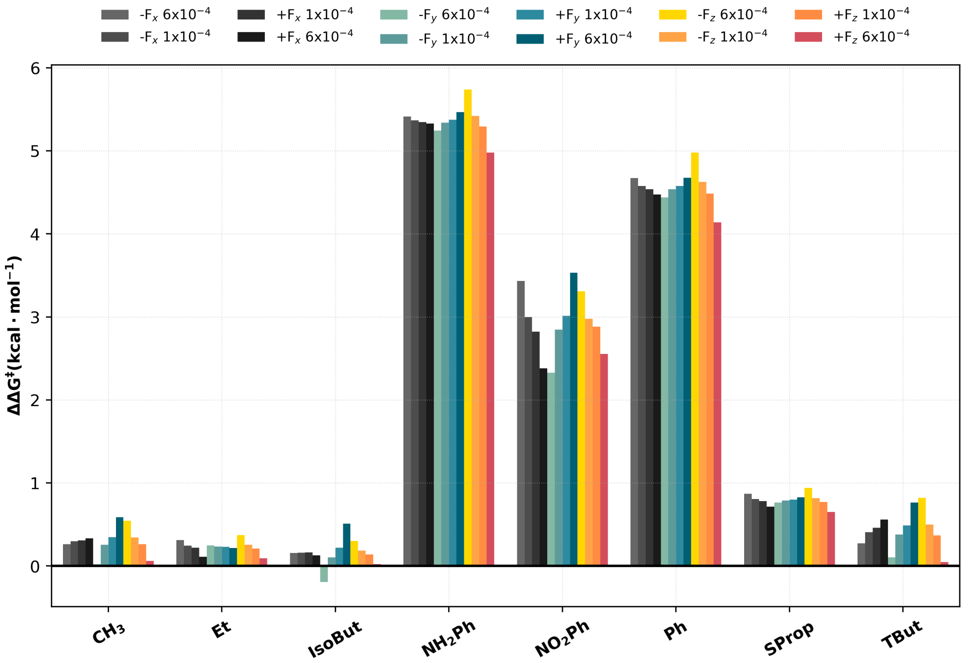

Figure 5.14: OEEF effect in the *CH*$_3$; *Et*; *SProp*; *IsoBut*; *TBut*; *Ph*; *NO*$_2$*Ph* and *NH*$_2$*Ph* Ester containing Hurd-Claisen rearrangements. The OEEF was applied along all three axes with two different magnitudes, 1.00×10^{-4} and 6.00×10^{-4} a.u., in opposite directions. These results were obtained with single-point calculations at the M06-2X/def2-TZVpp level of theory.

As a general rule, changing the magnitude of the OEEF affects only the intensity of the stabilization. Thus, if a field of 6.00×10^{-4} a.u. induces stabilization of the Z isomer, a field of 1.00×10^{-4} a.u. will also stabilize the Z isomer but to a lesser degree. Additionally, reversing the direction of the field will maintain this trend. With the exception of the *Et* reaction all others presented at least one Cartesian orientation that lead to a E-stabilization, and one that lead to a Z-stabilization.

It is important to note that variations in the OEEF magnitude are not sufficient to alter the stereoselectivity of reactions with a clearly defined preference for a particular isomer. However, as demonstrated by the sensitive changes observed in the *CH*$_3$ and both butyl Hurd-Est rearrangement, the OEEF can be effectively used to control the stereoselectivity of more "indecisive" reactions, where the energy difference between competing transition states is minimal.

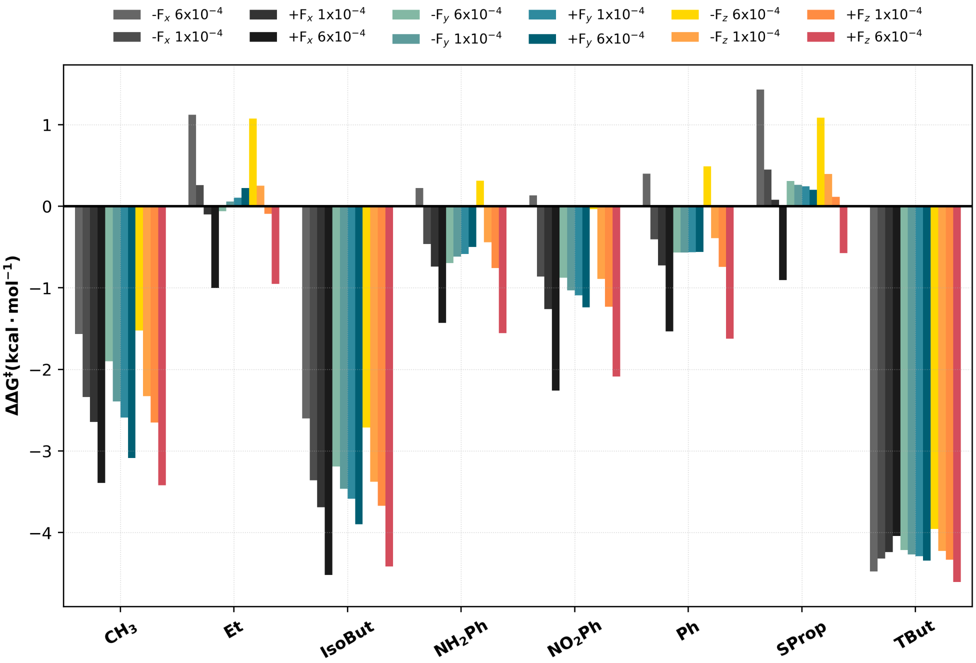

Figure 5.15: OEEF effect in the *CH*$_3$; *Et*; *SProp*; *IsoBut*; *TBut*; *Ph*; *NO*$_2$*Ph* and *NH*$_2$*Ph* Nitrile containing Hurd-Claisen rearrangements. The OEEF was applied along all three axes with two different magnitudes, 1.00×10^{-4} and 6.00×10^{-4} a.u., in opposite directions. These results were obtained with single-point calculations at the M06-2X/def2-TZVpp level of theory.

The same observation holds true for the Hurd-Nit reaction. In this case, the aryl substituents *Ph*, *NO*$_2$*Ph*, and *NH*$_2$*Ph* present "indecisive barriers", and have their stereoselectivity controlled by the OEEF.

Comparison of the molecular axis results for the methyl substituents, shown in Figure 5.16, reveals contrasting stereoselectivities. The small nitrile electron-withdrawing group leads to *Z*- isomer stabilization, while the ester electron-withdrawing group promotes *E*- isomer stabilization. The distinct electrostatic interactions associated with these two electron-withdrawing groups completely change the effect of the OEEF on the reaction pathway.

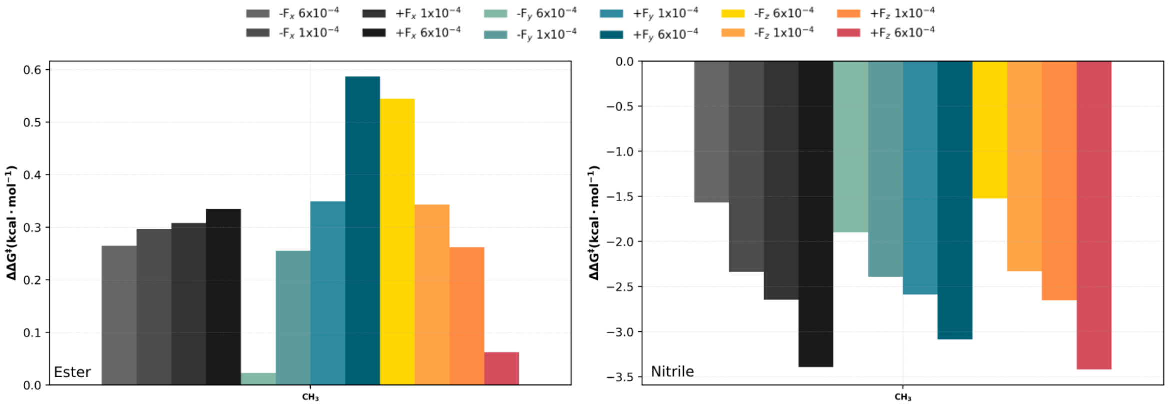

Figure 5.16: OEEF effect in the CH_3 Hurd-Claisen rearrangement with a Nitrile (right) and Ester (left) EWG. The OEEF was applied along all three axes with two different magnitudes, 1.00×10^{-4} and 6.00×10^{-4} a.u., in opposite directions. These results were obtained with single-point calculations at the M06-2X/def2-TZVpp level of theory.

In retrospect, this orientation leads to a significant change in the stereoselectivity of the reaction, with higher energy differentiation observed at lower field strengths compared to the Reaction Axis approach. Once again, closely related Z/E transition states exhibited an inversion of stereoselectivity depending on the magnitude of the OEEF.

For the Hurd-Est rearrangement, a negative y-oriented field induced an inversion for the $IsoBut$ reactions. While for the Hurd-Nit rearrangement, a negative x- or z-oriented field induced an inversion for the Et, $SProp$, and all aryl substituents, with any positive y-oriented field resulting In an inversion for the Et and $SProp$ reactions.

As stated by Shaik, an oriented external electric field applied outside the reaction axis cannot systematically modify the reactive bonds and is therefore better suited for stereochemical control. Consequently, this type of field, while responsible for large changes in stereocontrol, should not cause significant variations in the reaction rate[15].

By using the Curtin-Hammett principle, the analysis of the geometric and electronic parameters of TS is sufficient to highlight differences in isomerization outcomes under varying OEEF conditions. the OEEFs were able to control the stereoselectivity of reactions with similar transition-state energies, as exemplified by the alkyl Hurd-Claisen rearrangement. However, the experimental application of OEEFs presents significant challenges, particularly in achieving precise field orientation, as evidenced by the techniques discussed in the reviewed studies[10,12,15]. This raises a key question: Could a non-oriented or more isotropic electric field effectively influence the stereoselectivity of reactions with comparable transition-state energies, thereby circumventing the need for strict field alignment?

5.2.3 Isotropic Electric Field

To investigate this question, the effect of 50 OEEFs with varying orientations but constant magnitude was evaluated in the Hurd-Claisen rearrangements. Specifically, OEEFs with a magnitude of 4.00×10^{-3} a.u. were applied to the transition states of the nitrile-containing systems with CH_3, Et, $SProp$, Ph, and NO_2Ph substituents, as well as to the ester-containing variants with CH_3 and $SProp$. This approach enables the simulation of a truly non-oriented external electric field by sampling the interaction of the field with the molecule across its full set of rotational degrees of freedom. Figure 5.17 illustrates the isotropic field distribution applied to the Hurd-Nit $SProp$ rearrangement. By applying the electric fields in this manner, it becomes possible to study the influence of OEEFs on the transition state without imposing a specific orientation, as the rotational freedom of the molecule is inherently incorporated into the analysis.

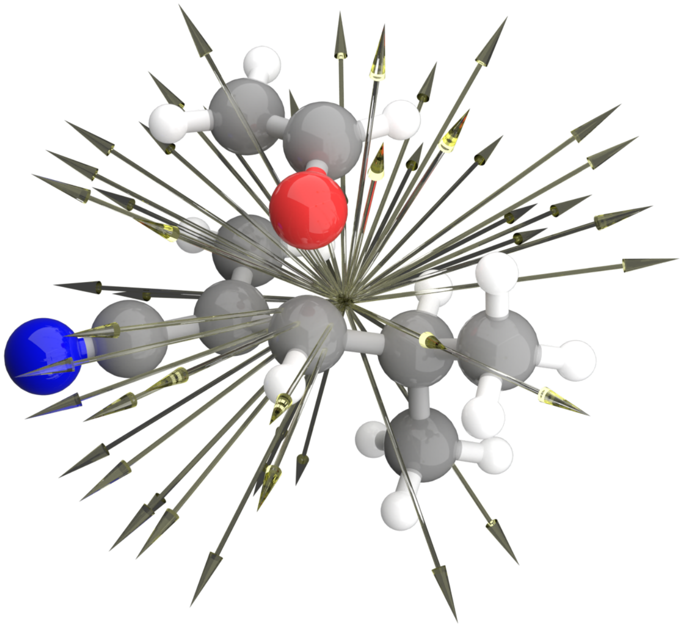

Figure 5.17: Representation of the isotropic field applied to the Hurd-Claisen rearrangement. Each reaction is studied with 50 different orientations of the OEEF, all with the same magnitude 4.00×10^{-3} a.u.

The results of the isotropic field study for the isopropyl Hurd-Nit transition state are shown in Figure 5.18. The energy of the field-free transition state was subtracted from that of the OEEF-applied transition states, enabling a direct comparison of the stabilization effects.

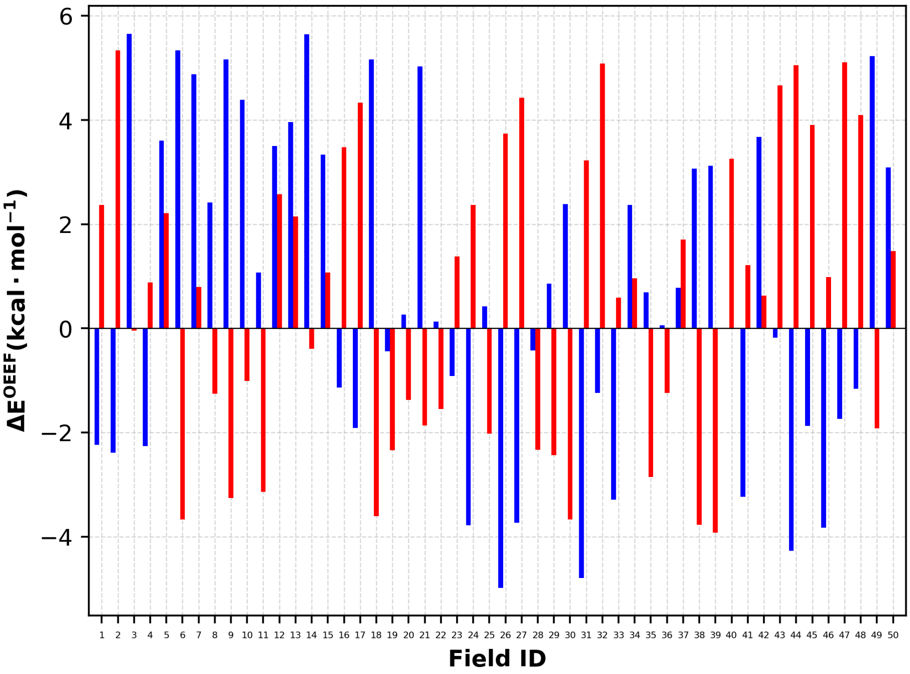

Figure 5.18: OEEF effect in the *SProp* Hurd-Claisen rearrangement with 50 different oriented Electric fields with equal magnitude (4.00×10^{-3} a.u.) for the E (blue) and Z (red) isomers. The energy of the field-free transition state was deducted from the energy of the OEEF-applied transition states.

It is clear that OEEFs with varying orientations but constant magnitude—hereafter referred to as the isotropic field—result in the destabilization of both E and Z isomers. Only 21 out of the 50 field orientations lead to a lowering of molecular energy for either isomer. The overall magnitude of this destabilization is comparable for both configurations, suggesting that the isotropic electric field exerts a similar influence on each isomer.

As stated previously, an electric field modifies the dipole moment of the molecule. This effect is also evident under the isotropic field approach, where the dipole moments vary drastically with the orientation of the field, as illustrated in Figure 5.19.

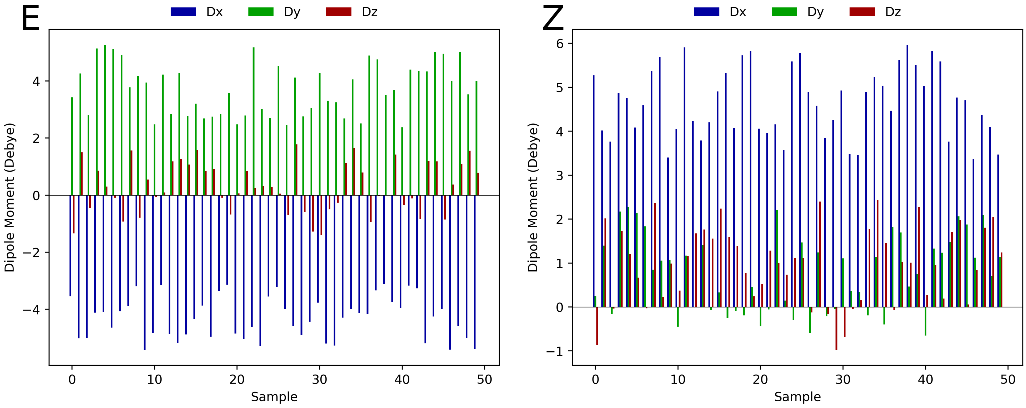

Figure 5.19: Components of the dipole moment of the *SProp* Hurd-Nit rearrangement with 50 different oriented Electric fields with equal magnitude (4.00×10^{-3} AU) for the E (right) and Z (left) isomers.

The dipole moments of the isomers are similar in magnitude, with the E isomer exhibiting an overall negative direction and the Z isomer a positive one. Notably, the dipole moment of the E isomer arises from a competition between the $\hat{\imath}$ and $\hat{\jmath}$ components, whereas the Z isomer is dominated by the $\hat{\imath}$ direction. This distinction indicates that the electric field does not modify the dipole moment equally for both isomers, even though their energy variations are similar. These findings suggest that Y-oriented OEEFs will influence the E isomer more strongly than the Z isomer, while Z-oriented fields will cause minimal differentiation between the two under a reaction axis-aligned orientation.

To accont for the shift on the geometrical parameters a RMSD analysis was performed, the results are shown in Figure 5.20.

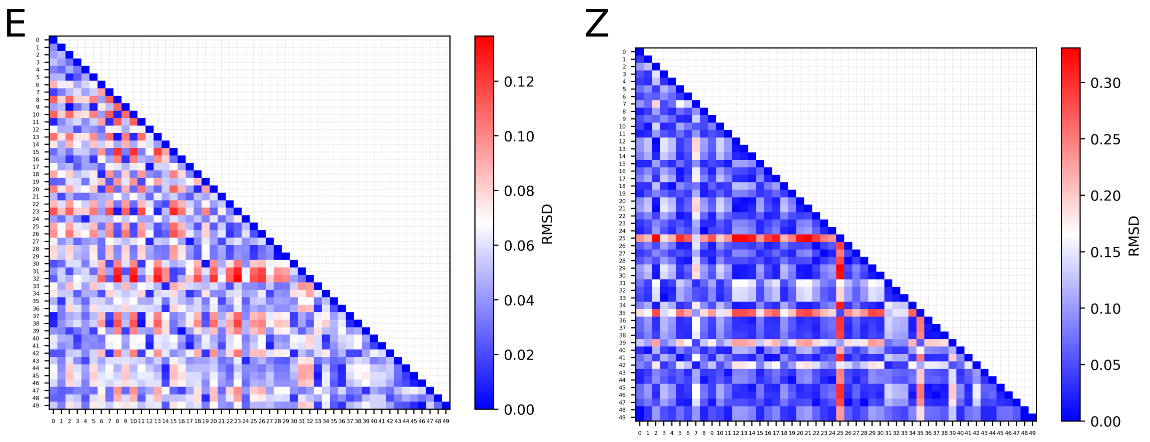

Figure 5.20: RMSD of the *SProp* Hurd-Claisen rearrangement with ten different oriented Electric fields with equal magnitude (4.00×10^{-3} a.u.) for the *E* (right) and *Z* (left) isomers

Two key conclusions emerge from the RMSD analysis. First, the *Z* isomer exhibits greater variation in transition state geometry, with a standard deviation of 0.0640 Å, compared to 0.0258 Å for the *E* isomer. This indicates that the *Z* isomer is more sensitive to the isotropic electric field.

Second, the maximum RMSD observed in the isotropic field study is significantly higher than that produced by the reaction-axis-oriented OEEF at the same field strength (see Figure A.1). This suggests that reaction-axis fields induce localized geometric changes near the reacting bonds, whereas isotropic fields promote a broader, more generalized relaxation across the entire molecule.

However, this effect is orientation-dependent, as electric fields with a significant *X*- or *Y*-component lead to higher RMSD values for the corresponding stereoisomer. Notably, the maximum RMSD for the *Z* isomer is nearly double that of the *E* isomer. This pronounced increase, however, occurs in response to a two specific OEEF direction, suggesting that it is linked to a specific field orientation rather than representing a general trend.

The same protocol was followed for the CH_3, *Et*, *Ph*, and NO_2Ph Hurd-Nit rearrangements. The energy variation is shown in Figure 5.21. The results are consistent with those of the *SProp* rearrangement, with the *E* isomer exhibiting a preference for the positive orientation of the OEEF and the *Z* isomer showing a slight preference for the negative orientation.

All studied TS exhibited more destabilizing interactions than stabilizing ones. A more pronounced energetic variation was observed for the NO_2Ph *Z* isomer when compared to the general behavior of the other systems. This trend is likely associated with the high polarizability of the NO_2Ph substituent, which enhances its interaction with the OEEF.

The geometrical changes once again played a minor role in the stabilization of the transition state for the *AX* stereoisomer. However, a greater distinction between the *E* and *Z* isomers was observed, particularly for the *Et* and NO_2Ph rearrangements. These differences suggest that the activation complex of the *EQ* isomer is more strongly perturbed by the OEEF, leading to more pronounced polarization changes in these cases.

Comparison of these findings with the reaction axis results indicates that a non-reactive alignment of the OEEF induces greater perturbation of the transition state geometry, and consequently, larger changes in both dipole moment and system energy. This trend is consistent with the findings reported by Shaik, in which non-reactive OEEFs were shown to be more effective at controlling stereoselectivity[15,21].

To avoid repetition, the RMSD values for the CH_3, *Et*, *Ph*, and NO_2Ph rearrangements are not shown here, but can be found in the appendix.

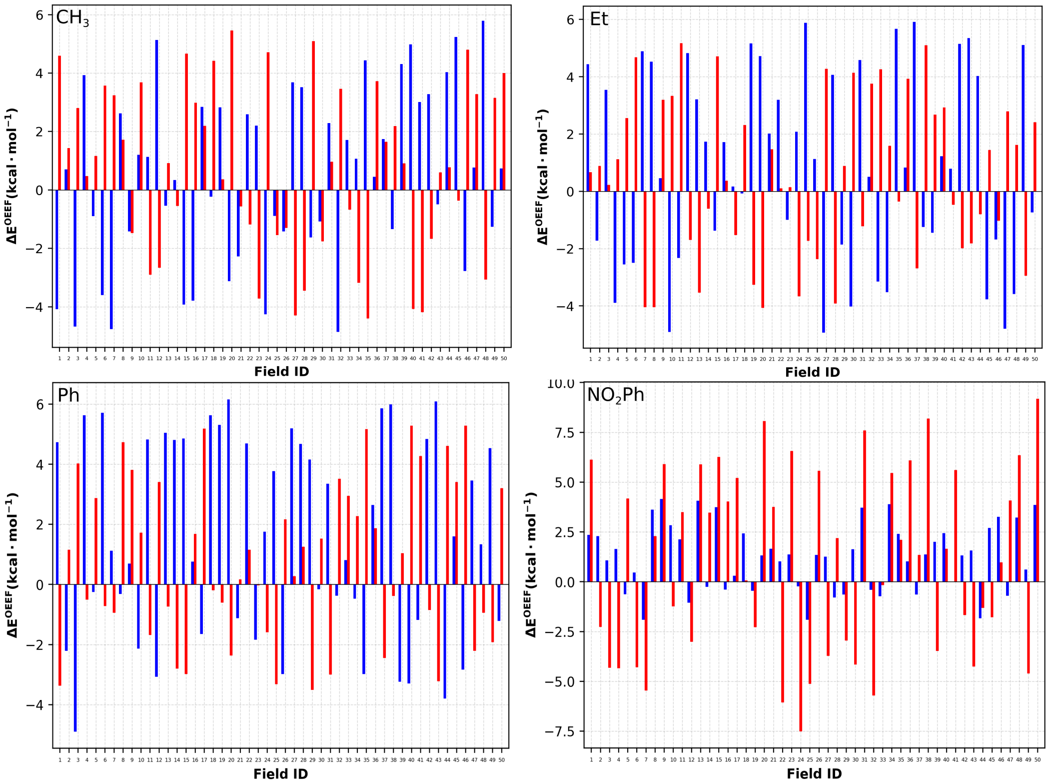

Figure 5.21: OEEF effect in the CH_3 (upper left); *Et* (upper right); *Ph* (down left) and NO_2Ph (down right) Hurd-Nit rearrangements with 50 different oriented Electric fields with equal magnitude (4.00×10^{-3} AU) for the *E* (blue) and *Z* (red) isomers. The energy of the field-free transition state was deducted from the energy of the OEEF-applied transition states.

Lastly, the thermally corrected Gibbs free energy was calculated. Drawing inspiration from the average solvent electrostatic configuration, the mean effect of an electric field was estimated as the arithmetic mean of the Gibbs free energy values obtained from the studied field orientations. The results are presented in Table 5.2.

Interestingly, a simple arithmetic average of the Gibbs free energy can overlook an important aspect of how electric fields affect reactivity. Experimentally, the reactive system not only adapts its atomic positions in response to the field, but also tends to reorient itself so that its dipole moment aligns anti-parallel to the external field. As a result, configurations already aligned in this way are statistically more likely to be populated in the reaction medium.

To account for the rotational freedom of molecules, a weighted mean was calculated in which the dipole-field orientation was incorporated using the dipole-field interaction energy, as described by Shaik et al.[21]. This interaction, computed from the perturbed dipole moments, was incorporated into a Boltzmann distribution to statistically weight the Gibbs free energy of each configuration. Appropriate unit scaling factors were applied to ensure thermochemical consistency, allowing this model to reflect both electronic and geometrical contributions to field-induced reactivity.

$$\beta_i = e^{-\left(\frac{\vec{E}_i \cdot \vec{\mu}_i}{4.8 k_b T}\right)} \tag{5.1}$$

In this formulation, an anti-parallel dipole-field alignment yields a greater weight, while a parallel alignment yields a weight close to zero. The mean Gibbs free energy was then computed as:

$$\bar{\Delta}G = \frac{\sum_{i=1}^{n} \beta_i G_i}{\sum_{i=1}^{n} \beta_i}, \tag{5.2}$$

where G_i is the Gibbs free energy of the i-th sample, γ_i is the corresponding weight, and n is the number of samples. The final results are presented in Table 5.2.

Boltzmann averaging reproduced the qualitative trends observed in the arithmetic means (including stereoselectivity inversions), albeit with an amplified magnitude owing to its exponential sensitivity to dipole-field interactions ($e^{-\Delta E/k_B T}$). As shown in Figure 5.22, this scheme disproportionately favors near-antiparallel alignments and effectively suppresses other configurations. However, Boltzmann weighting assumes instantaneous orientational equilibrium, which is a problematic premise for transition states, whose lifetimes (10^{-13} s)[101] are typically several orders of magnitude shorter than the rotational diffusion timescales ($>> 10^{-9}$ s)[102]. To resolve this bias while retaining the preferential alignment effects, we employed a von Mises-Fisher distribution[103,104] scheme (Table 5.2). This approach better represents the partial orientational equilibrium achievable during the TS lifetime because it maintains the Boltzmann-like preference for anti-alignment and smoothly samples non-equilibrated configurations.

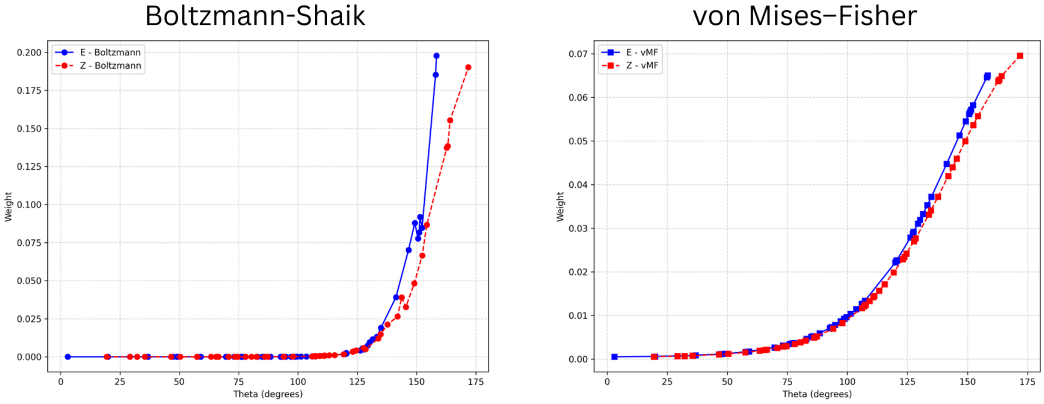

Figure 5.22: Weights of the *SProp* Hurd-Nit rearrangement with 50 different oriented Electric fields with equal magnitude (4.00×10^{-3} AU) for the E (blue) and Z (red) isomers, for the Boltzmann (left) and von Mises-Fisher (right) distributions.

The von Mises-Fisher distribution is a probability distribution defined on the surface of a sphere, commonly used to model directional data. It is characterized by two parameters: a mean direction (or orientation) and a concentration parameter, which determines how tightly the distribution is clustered around that direction. The von Mises-Fisher distribution is particularly useful for modeling three-dimensional orientation-dependent phenomena, such as the spatial distribution of molecular dipole moments.

In this work, the cosine of the angle between the dipole moment and the electric field vector was used to define the mean direction, and the concentration parameter was set to 5.This formulation preserves the benefits of rotational sampling while mitigating statistical biases caused by extreme dipole-field alignments. The cosine-weighted von Mises-Fisher distribution used here is defined as:

$$f(\theta) = e^{\left(\frac{\kappa(1-\cos\theta)}{2}\right)} \tag{5.3}$$

Once again, rearrangements with closely related energy barriers show great potential for the use of OEEFs in controlling the stereoselectivity of the reaction. The *Et* and *Ph* Hurd-Nit rearrangements exhibit Z-isomer preference in the absence of a field, but the application of an isotropic field shifts the selectivity toward the E isomer. The *SProp* and NO_2Ph rearrangements display a similar trend; however, in these cases, the isotropic field further enhances the preference for the Z isomer.

Table 5.2: $\Delta\Delta G^{\ddagger}$ between the Z and E free energy values (ΔG) for the studied Hurd-Nit rearrangements under different averaging schemes: arithmetic mean (Mean), and orientation-weighted average (Pond), and non-field perturbed[19] (NF). All values are in kcal/mol.

Substituent	Mean	Boltz	vMF	Non-Perturbed[19]
CH_3	-2.7675	-2.1423	-2.6073	-2.6360
Et	0.4788	0.9781	1.0997	-0.0630
SProp	0.2727	0.6717	0.5252	0.2510
Ph	0.6067	0.5771	0.8687	-0.2510
NO_2Ph	-0.6374	-5.7827	-3.5112	-0.8790

Interestingly, the methyl-substituted system appears to be largely unresponsive to the isotropic field, which suggests that the limited degrees of freedom associated with the methyl group hinder significant reorientation of the dipole moment in response to the field.

All weighted averaging methods produced consistent trends in Gibbs free energy. However, the use of a von Mises-Fisher distribution led to a smoother and more stable convergence of the averaged values, particularly for the NO_2Ph system.

The same protocol can be applied to the Hurd-Est rearrangements, specificly the CH_3 and *SProp* rearrangements. As seen in Figure 5.23, the same kind of development is observed for the Hurd-Est rearrangement. Both substituents had a more destabilizing interactions then not, with a maximum of 4.15 kcal/mol for the *SProp* rearrangement and 3.98 kcal/mol for the CH_3 rearrangement.

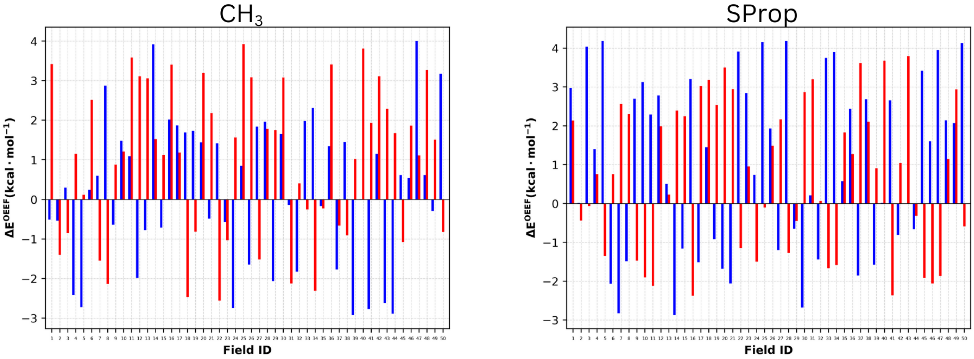

Figure 5.23: OEEF effect in the CH_3 (left) and *SProp* (right) Hurd-Est rearrangements with 50 different oriented Electric fields with equal magnitude (4.00×10^{-3} AU) for the E (blue) and Z (red) isomers. The energy of the field-free transition state was deducted from the energy of the OEEF-applied transition states.

As expected, the results for RMSD and dipole moment were also similar. However, in this case, no substituent exhibited a greater-than-average geometrical response. This is further supported by the dipole moment analysis of the CH_3 and *SProp* rearrangements, shown in Figure 5.24.

The axial methyl substituent displays a competition between the $\hat{j}$ and $\hat{k}$ components, while the equatorial configuration is characterized by a three-way competition among the $\hat{\imath}$, $\hat{j}$, and $\hat{k}$ components. In contrast, the isopropyl rearrangements exhibit a much simpler dipole behavior: the $\hat{\imath}$ component dominates the E isomer, while the $\hat{j}$ component dominates the Z isomer.

This dipole differentiation illustrates the distinct ways in which each substituent interacts with the isotropic electric field, which is likely the primary reason for the different stabilization trends observed between isomers.

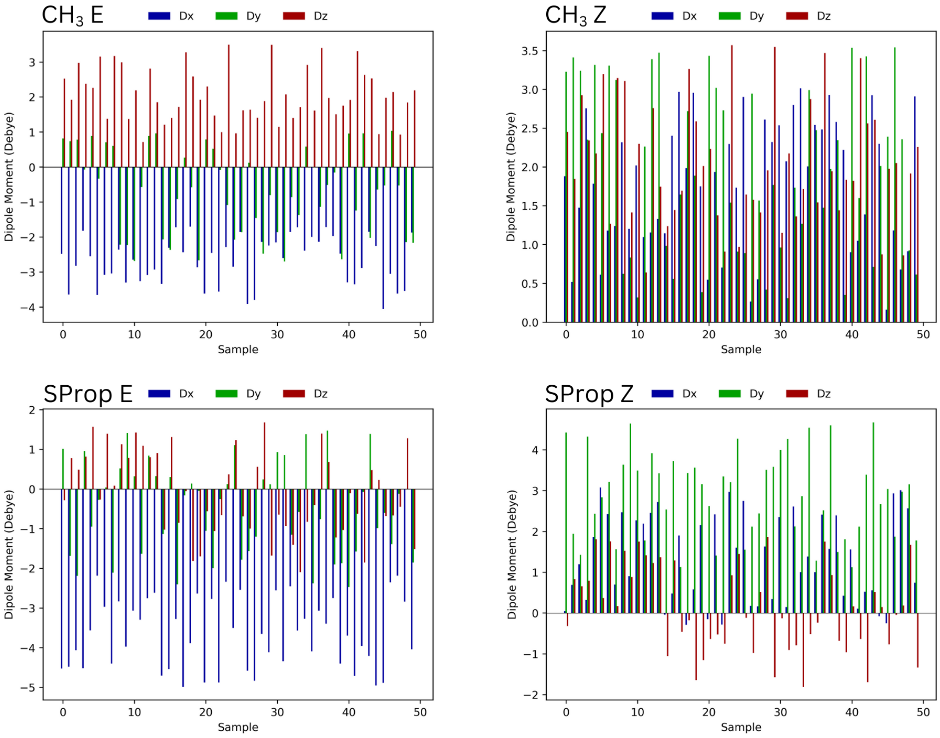

Figure 5.24: Components of the dipole moment of the *SProp* (down) and CH_3 (upper) Hurd-Est rearrangement with 50 different oriented Electric fields with equal magnitude (4.00×10^{-3} AU) for the E (left) and Z (right) isomers.

By averaging the Gibbs free energy of the CH_3 and *SProp* Hurd-Est rearrangements (Table 5.3), we observe that the stereoselectivity of the CH_3 rearrangement is inverted, while the *SProp* rearrangement remains unchanged. This suggests that isotropic electric fields can effectively control the stereoselectivity of reactions with similar transition-state energies, even in the absence of strict field alignment.

A particularly interesting point is the difference in sign between the Boltzmann and von Mises-Fisher distributions for the methyl rearrangement. This indicates that the heavily weighted antiparallel field configurations are E-stabilizing in this case.

Table 5.3: $\Delta\Delta G^{\ddagger}$ between the Z and E free energy values (ΔG) for the studied Hurd-Nit rearrangements under different averaging schemes: arithmetic mean (Mean), and orientation-weighted average (Pond), and non-field perturbed[19] (NF). All values are in kcal/mol.

Substituent	**Mean**	**Boltz**	**vMF**	**Non-Perturbed[19]**
CH_3	-0.5661	0.1014	-0.4612	0.1260
SProp	1.0593	1.4271	1.3831	0.8790

A reasonable conclusion can be drawn from the isotropic electric field study: the use of a non-oriented electric field can effectively modulate the stereoselectivity of reactions with similar transition-state energies. However, this modulation is strongly influenced by the nature of the substituent. Previously "indecisive" reactions—such as the Hurd-Nit *SProp* case—did not undergo a complete inversion of stereoselectivity. Nevertheless, even in these cases, the standard stereochemical outcome was reinforced.

These results suggest that isotropic electric fields represent a promising tool for stereocontrol in organic reactions, offering an experimentally feasible approach to applying invisible catalysis. However, computational methods remain essential for predicting the favored isomer, as this approach cannot universally dictate stereoselectivity at will.

5.2.4 Anchored Transition States by Thiolate Linkers on Gold Substrates

To overcome the experimental challenges associated with achieving precise alignment between the electric field and the desired molecular axis[10,12–14,105], a common strategy is to restrict molecular rotation by anchoring the system to a surface—most notably through the use of gold thiolate substrates[12,30]. In this approach, the molecule is covalently bonded to a gold surface via a thiol group, forming a robust and directional attachment that effectively immobilizes the molecular framework.

This section explores the theoretical application of OEEFs to such surface-bound systems. By eliminating rotational degrees of freedom, these models allow for a more realistic investigation of field-induced catalytic effects under experimentally accessible conditions. Geometry optimizations of the thiolate-bound systems were performed with the gold atoms held fixed, using the same computational protocol as in the previous sections. This approach was inspired by the work of Ramanan et al.[30].

Figure 5.25 shows the optimized structures of the Hurd-Est *Ph* transition states, each anchored via a thiol group to a five-atom gold surface. It is important to note that bonding occurs through the ester electron-withdrawing group, making this methodology inapplicable to the Hurd-Nit rearrangement. The OEEF alignment was based on the gold surface, where the Z-axis as aligned with the electric field in a menner to mimic the experimental conditions. The results are shown in Figure 5.26.

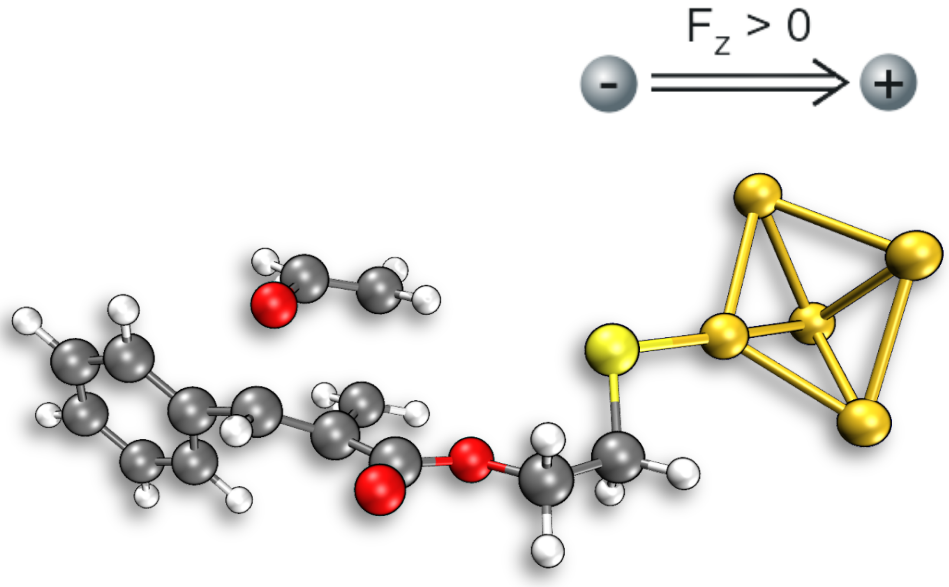

Figure 5.25: Optimized structures of the Hurd-Est *Ph axial* transition state, anchored via a thiol group to a five-atom gold surface, using the M06-2X/6-311+g(d,p) / SDD level of theory.

Immediately, it is evident that the degree of stabilization is significantly higher than that observed in the previous sections, reaching up to 2.00×10^1 kcal/mol for both rearrangements. This pronounced effect is likely due to the increased polarizability of the gold surface, which enhances the interaction with the OEEF and alters the molecular dipole moment through substrate-induced polarization.

These results are consistent with the findings of Ramanan et al.[30], who demonstrated that the gold substrate plays a significant role in the stabilization mechanism of the transition state.

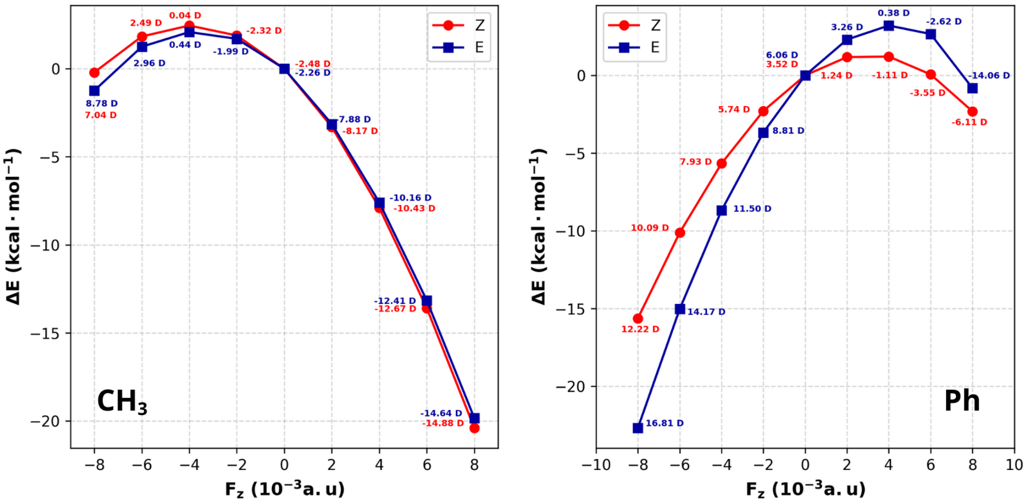

Figure 5.26: OEEF stabilization in the *Ph* (Right) and CH_3 (Left) Hurd-Est rearrangements with magnitudes ranging from (-8.00×10^{-3} to 8.00×10^{-3} AU) for the *E* (blue) and *Z* (red) isomers. The energy of the field-free transition state was deducted from the energy of the OEEF-applied transition states.

An important distinction between the CH_3 and *Ph* anchored systems is the inversion of their stabilization trends. The *Ph* isomer is stabilized by a negative electric field, whereas the CH_3 isomer is stabilized by a positive one. This phenomenon arises from differences in the overall dipole moments of the transition states: the *Ph* isomer exhibits a positive $\hat{k}$ component, while the CH_3 isomer has a negative one. As a result, each structure is preferentially stabilized by a field oriented in the direction opposite to its dipole moment, while initially experiencing destabilization under the opposing field.

This provides a clear example of how the substrate can significantly modify the dipole moment of the molecule, and thus influence its interaction with the OEEF. Notably, although the direction and magnitude of stabilization differ, both systems eventually experience net stabilization under any sufficiently strong field, once their dipole moments become anti-aligned with the applied field.

By analyzing the $\Delta\Delta G^{\ddagger}$ values in Figure 5.27, it is evident that the *Ph* transition state undergoes stereoselectivity modulation, despite exhibiting a clear preference for the *Z* isomer. When compared to the non-substrate results, the gold surface alone is sufficient to reverse the previously observed "unprecedented" *E*-selectivity of the unanchored *Ph* rearrangement, highlighting the significant role of the substrate in governing the reaction outcome. The CH_3 rearrangement, on the other hand, is not strongly affected by the substrate, as it maintains its original preference for the *E* isomer.

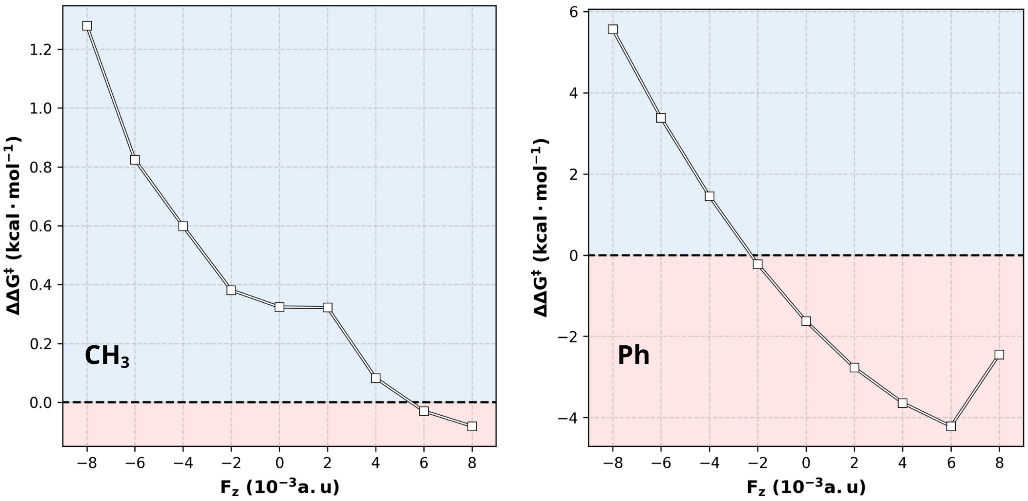

Figure 5.27: OEEF effect in the $\Delta\Delta G^{\ddagger}$ *Ph* (Right) and CH_3 (Left) Hurd-Est rearrangements with magnitudes ranging from (-8.00×10^{-3} to 8.00×10^{-3} AU) for the blue zone represents a *E* preference while the red zone represents a *Z* preference. The thermally corrected Gibbs free energy was calculated using $373K$ as the temperature.

A point of interest lies in the reduced stereodifferentiation observed at a field strength of 8.00×10^{-3} a.u., which shows a stronger preference for the *E* isomer compared to its 6.00×10^{-3} a.u. counterpart. As shown in Figure 5.26, this effect originates from the broken-symmetry of the wave function at this field strength. This behavior is consistent with the findings of Shaik[15], who noted that at sufficiently high field strengths, the dipole moment can become non-zero, resulting in a loss of stereoselectivity. Nonetheless, this behavior is unlikely to pose complications in practical applications, as experimental field strengths are expected to remain well below the levels that produce this effect.

The influence of the gold thiolate linkers on the properties of the Hurd-Claisen reaction was also evaluated by analyzing the Mulliken group charges of the molecular fragments defined in Figure 5.28, as well as the total molecular dipole moment in both field-free condition and under applied $\pm F_z$ fields, as shown in Figure 5.29. This analysis is conceptually inspired by the work of Ramanan et al.[30], who emphasized the role of field-induced charge migration and dipole modulation in governing reactivity and selectivity under OEEF.

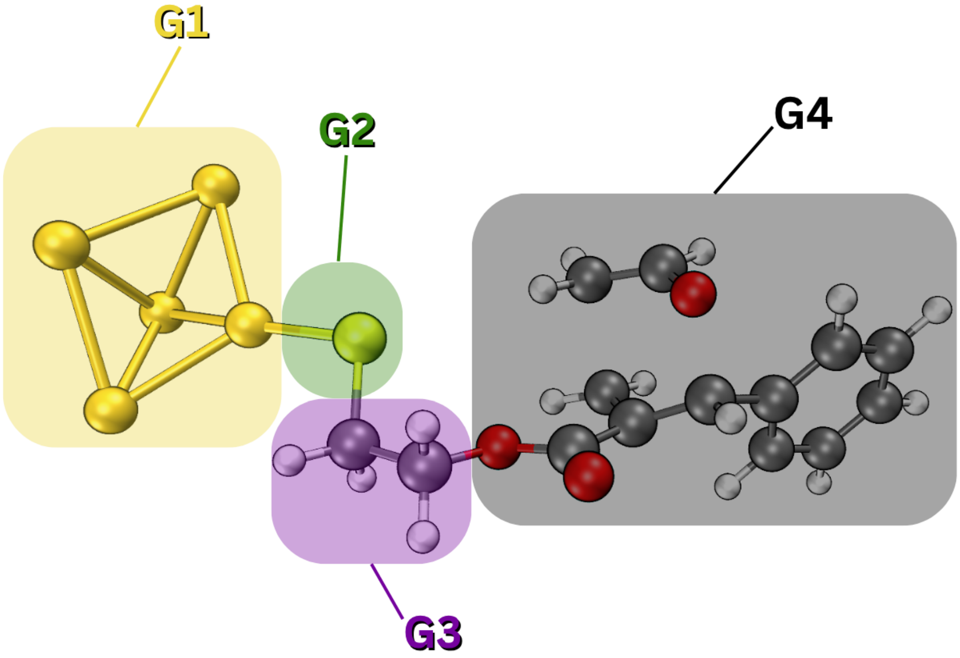

Figure 5.28: Molecular fragmentation scheme used to compute Mulliken group charges. The fragments G1-G4 were defined to enable a detailed analysis of charge redistribution under varying orientations and strengths of OEEFs.

In the absence of an external field, there is a clear charge separation more pronounced between fragment G1 (gold cluster) and G2 (sulfur atom) but the separation extends from the positively charged G3 (ethyl bridge) to the negatively charged G4 fragment (the reaction center). We observed that this charge separation at $F_z = 0$ is more significant for the E-than for the Z-isomer. Thus, the linkers introduces local dipoles whose electric fields are the underlying reason for the inversion for Z-preference observed at $F_z = 0$ in Figure 5.27 for Ph-substituted Hurd-Est rearrangement, showing also in the case of the reactions studied here that the linker moieties may not remain innocent when OEEFs are applied on the system.[30] Also, we note from the lower panels of Figure 5.29 that the total molecular dipole moment at $F_z = 0$ is almost orthogonal to the external field in the E-isomer but that there is some positive projection in the Z-isomer. These relative dipole orientations effectively explains the initial destabilization of the transition state for $F_Z > 0$.

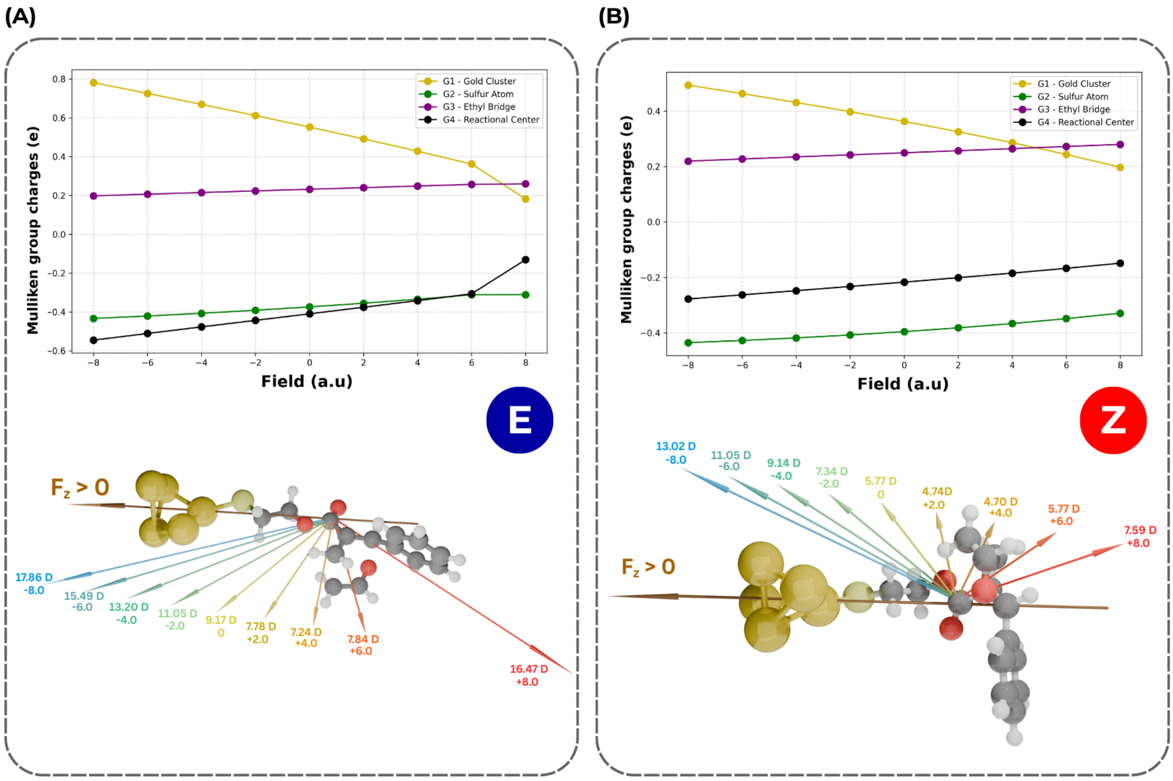

Figure 5.29: Mulliken group charges of the molecular fragments defined in Fig. 5.28 as a function of the OEEF for the (A) *E* and (B) *Z*-isomer of the Ph-substituted Hurd-Claisen rearrangement. The lower panels show the positive direction of the external field (along z-axis) and the corresponding total molecular dipole moments (in Debye) as a function of both strength and orientation of the field (in 10^{-4} *a.u.*) for each isomer.

Upon application of a positive electric field ($F_Z > 0$), we observe a pronounced polarization effect characterized by charge density shifting away from the reaction center (G4) toward the Au cluster (G1). In contrast, the connecting groups (G2 and G3) exhibit only modest changes, indicating limited participation in the polarization process. This trend is reflected in the shallow slopes of their charge-*versus*-field curves in Figure 5.29. Under $F_Z > 0$, the total dipole moment increases in magnitude and reorients in the direction of the field, but the magnitude of the total dipole decreases accordingly.

When the field is reversed ($F_Z < 0$), the direction of charge transfer is also reversed: G1 donates electron density to the other fragments, particularly toward the reaction core. As a result, the total dipole moment projects in the negative z-direction and reaches a larger magnitude compared to the $F_Z > 0$ case. This enhancement arises from the more extensive charge separation induced by the greater electron donation from the Au cluster. In all cases, the total dipole moment reorients to remain aligned with the direction of the applied external electric field, reflecting the system's intrinsic tendency to minimize electrostatic energy through dipole-field alignment.

As a final remark, the use of a gold substrate to anchor the molecule offers a promising avenue for the experimental application of OEEFs in the Hurd-Est rearrangement. It enables modulation of reaction stereoselectivity, even in systems with previously well-defined selectivity. This approach not only enhances the interaction between the OEEF and the transition state, but also allows for experimentally achievable control over the field orientation.

5.3 Solvent Efect

The convergence of the dipole moment for the CH_3 ester- and nitrile-containing Hurd-Claisen rearrangements in EVE is shown in Figure 5.30. For the Hurd-Est rearrangement, the initial dipole moment of 3.60 D rapidly increased to around 4.15 D, converging shortly thereafter. The Hurd-Nit reaction follows the same trend, but with higher dipole moments throughout.

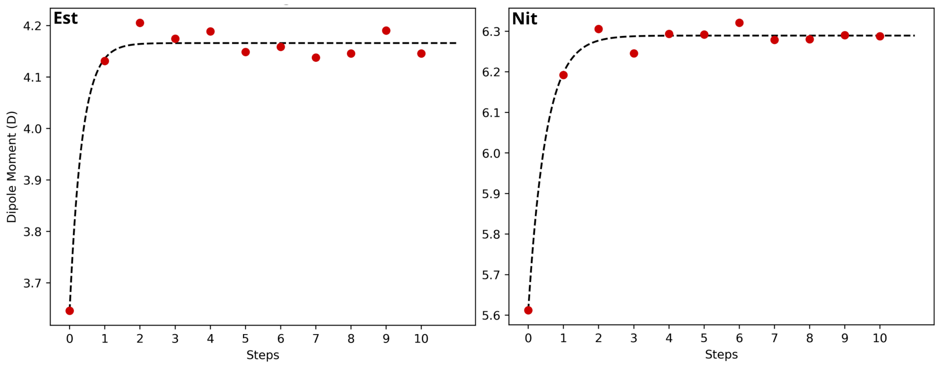

Figure 5.30: Convergence of the dipole moment of the $E-CH_3$ Hurd-Claisen rearrangements in EVE, for both EWG, with the S-QM/MM solvation protocol at 373 K and M062X/def2tzvpp level of theory.

This kind of dipole convergence is expected from the methodology, as the initial iteration of the dipole moment (step 0) is performed with the molecule in vacuum, and the solvent is added in the first MC step of the iteration. This results in a rapid increase in the dipole moment due to the sudden addition of the solvent charge points. All studied systems showed a similar behavior, with the dipole moment increasing in the first iteration step and then converging to a final value after approximately five iteration steps. Tables 5.4 and 5.5 shows the initial and final dipole moments for the studied systems. As all electrostatic convergences were similar, the rest os this result were relegated to appendix A.2.

Table 5.4: Initial and final dipole moments for the Hurd-Est systems.

AX			**EQ**		
System	Initial (D)	Converged (D)	System	Initial (D)	Converged (D)
E-Et	3.6153	4.1139	Z-Et	3.274	3.7591
E-CH_3	3.6456	4.146	Z-CH_3	3.3115	3.787
E-SProp	3.6305	4.203	Z-SProp	3.2662	3.753
E-TBut	3.2308	3.7219	Z-TBut	3.2699	3.7481
E-Ph	3.7094	4.2601	Z-Ph	3.7071	4.2388
E-NH_2Ph	3.7762	4.5097	Z-NH_2Ph	2.8419	3.1969
E-NO_2Ph	5.8917	6.577	Z-NO_2Ph	9.2818	10.3612

Table 5.5: Initial and final dipole moments for the Hurd-Nit systems.

AX			**EQ**		
System	Initial (D)	Converged (D)	System	Initial (D)	Converged (D)
E-Et	5.6788	6.3848	Z-Et	4.8342	5.5191
E-CH_3	5.6122	6.288	Z-CH_3	5.0297	5.678
E-SProp	5.7014	6.4096	Z-SProp	4.7782	5.5168
E-TBut	5.5235	6.1713	Z-TBut	4.7502	5.4422
E-Ph	5.8605	6.5182	Z-Ph	4.5901	5.2213
E-NH_2Ph	6.9179	7.8611	Z-NH_2Ph	3.5564	3.974
E-NO_2Ph	3.3619	3.6541	Z-NO_2Ph	8.9043	9.9998

By analyzing the differences in bond length for the forming $C-C$ bond and the breaking $C-O$ bond, we observe variations of approximately 0.002 Å in both cases. These changes depend on the solvent configuration and can be either positive or negative. However, at the molecular scale, such variations are minimal and do not significantly impact the overall structural stability, as shown in Figure 5.31.

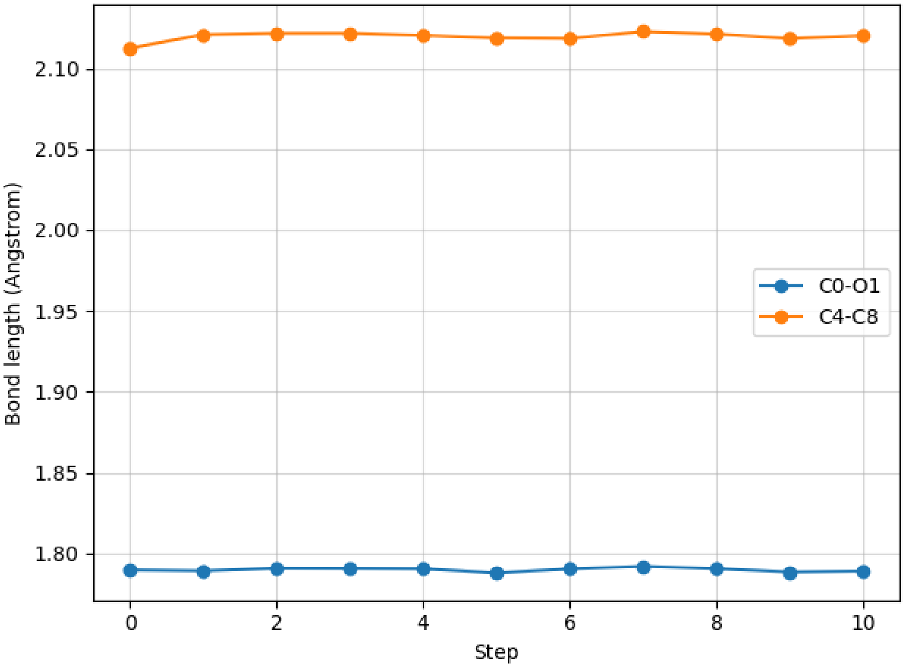

Figure 5.31: Convergence of the bond length of the $E-CH_3$ Hurd-Claisen rearrangement in EVE, with the S-QM/MM solvation protocol at 373 K and M062X/def2tzvpp level of theory. The $C0-O1$ bond is the breaking bond, while the $C4-C8$ bond is the forming bond. The values are shown in Å.

This kind of behavior is common on all studied systems, being then ester or nitrile containing. Figure 5.32 shows the root mean square deviation (RMSD) between consecutive geometries of the studied systems in EVE, with the S-QM/MM solvation protocol at 373 K and M062X/def2tzvpp level of theory. By calculating the RMSD, we observe that geometric changes are, in general, significantly more pronounced under the influence of a strong OEEF. While the RMSD induced by the OEEF is at 0.1 Å, the RMSD for the S-QM/MM solvation model is around 0.02 Å, as shown in Figure 5.32. This substantial difference suggests that the OEEF exerts a stronger perturbative effect on molecular geometry compared to solvent-induced structural changes in the S-QM/MM solvation model.

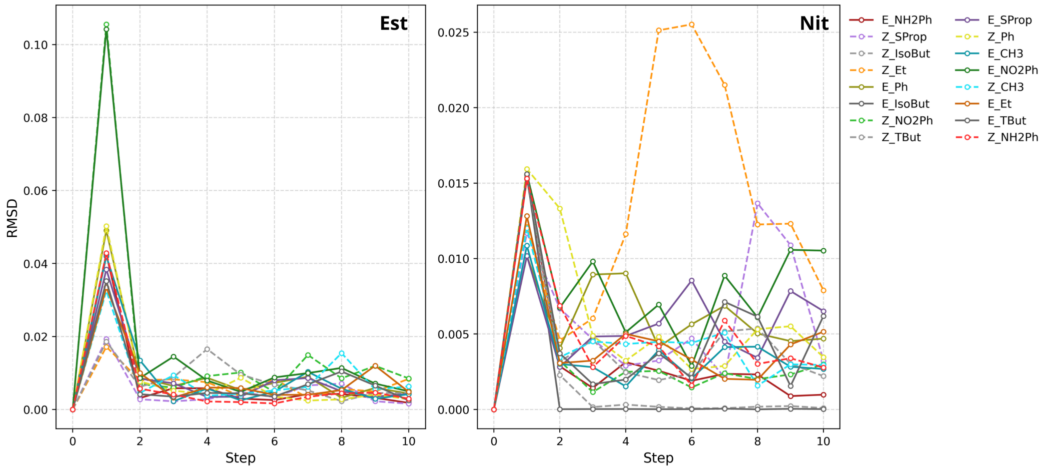

Figure 5.32: RMSD between consecutive geometries of the studied systems in EVE, with the S-QM/MM solvation protocol at 373 K and M062X/def2tzvpp level of theory.

Even with the exception — the ethyl system, which exhibits a higher RMSD at the fifth iteration step, the geometric efects on the nitrile containing systems are significantly less pronounced than those observed in the ester-containing systems. However, these geometric changes are insignificant when compared to the OEEF perturbation, or the electronic perturbation induced by the charge points, leading to the conclusion that, in the same way as the field perturbation, the bulk of the energetic changes provided by the S-QM/MM solvation protocol is electronic in nature.

under solvation — the geometric effects remain comparable in both cases. Notably, weaker fields produce similar geometric displacements because charge points are mathematically treated as perturbations to the one-electron integral. During optimizations, these charge-induced perturbations effectively mimic the behavior of an applied electric field, leading to comparable structural effects.

Table 5.6 and Figure 5.33 present the Gibbs free energy differentiation between the two isomers for the studied systems in EVE at 373 K, incorporating Grimme quasi-harmonic corrections computed using the GoodVibes package[100]. Additionally, the corresponding non-solvated values reported by Oliveira[19] are presented.

Table 5.6: Gibbs free energy of activation ($kcal \cdot mol^{-1}$) for the studied systems in EVE. The table is divided into two sections: Esters for the Hurd-Est rearrangement and Nitriles for the Hurd-Nit rearrangement. The values for the non-solvated systems are taken from Oliveira[19].

Esters			**Nitriles**		
System	$\Delta G^{\ddagger}_{EVE}$	$\Delta G^{\ddagger\,19}$	System	$\Delta G^{\ddagger}_{EVE}$	$\Delta G^{\ddagger\,19}$
CH_3	-2.946	0.126	CH_3	1.761	-2.636
Et	-1.684	0.314	Et	1.072	-0.063
NH_2Ph	3.865	5.396	NH_2Ph	-1.301	-0.314
NO_2Ph	-0.612	2.635	NO_2Ph	-1.531	-0.879
Ph	17.910	4.581	Ph	7.271	-0.251
SProp	-0.344	0.878	SProp	5.454	0.251
TBut	-1.263	0.126	TBut	1.798	-4.455

Focusing on the Hurd-Est rearrangement, the solvation methodology led to significant changes in stereoselectivity, with the E isomer being favored in most cases, except for the NH_2Ph and Ph rearrangements. These two exceptions exhibit greater stabilization of the Z transition state. In the first case, the charge point-induced dipole moment provides stronger stabilization for the Z isomer based on dipole-dipole interactions; nonetheless, the effect is not sufficient to overcome the already E-favored energetic barrier. This analysis can be extended to many of the reactions studied here, serving as a rule of thumb to predict the charge point interaction as a weak field. This finding suggests that charge points can significantly influence the stabilization provided by the OEEF, acting as a barrier to dipole moment changes and interactions. This behavior resembles the solvent screening effect described by Dubey[23].

Table 5.7: Dot product for normalized dipole moments of the studied Hurd-Est systems in EVE and the global S-QM/MM solvation charge points; calculations were made at 373 K and M062X/def2tzvpp level of theory.

E isomers	Dipole	Z isomers	Dipole	Preference
CH3	0.481	CH3	-0.677	Z
Et	0.166	Et	0.624	E
NH2Ph	-0.604	NH2Ph	-0.957	Z
NO2Ph	-0.299	NO2Ph	-0.934	Z
Ph	-0.208	Ph	-0.301	Z
SProp	0.382	SProp	-0.747	Z
TBut	-0.048	TBut	0.234	E

A similar behavior is observed for the Hurd-Nit rearrangement, where the *E* isomer is favored in most cases, except for the NH_2Ph and NO_2Ph systems. In the latter, the *Z* isomer is favored due to the charge point-induced dipole moment providing stronger stabilization for the *Z* transition state, based on dipole-dipole interactions. It is important to note that not all systems can be correctly evaluated by dipole-dipole interactions, as indicated by the red lines in Tables 5.7 and 5.8. For these cases, where geometric effects are minimal, localized solvent-solute interactions are the main cause of deviation.[106]

Table 5.8: Dot product for normalized dipole moments of the studied Hurd-Nit systems in EVE and the global S-QM/MM solvation charge points; calculations were made at 373 K and M062X/def2tzvpp level of theory.

E isomers	Dipole	Z isomers	Dipole	Preference
CH3	0.344	CH3	0.283	Z
Et	-0.646	Et	-0.657	E/Z
NH2Ph	-0.934	NH2Ph	0.551	E
NO2Ph	0.618	NO2Ph	-0.837	Z
Ph	0.294	Ph	0.761	E
SProp	-0.442	SProp	-0.092	E
TBut	-0.932	TBut	-0.893	E

Figure 5.33 illustrates the difference in Gibbs free energy of activation for the studied systems in EVE at 373 K, with Grimme quasi-harmonic corrections applied using the GoodVibes package[100]. The results in orange were taken from Oliveira[19,20].

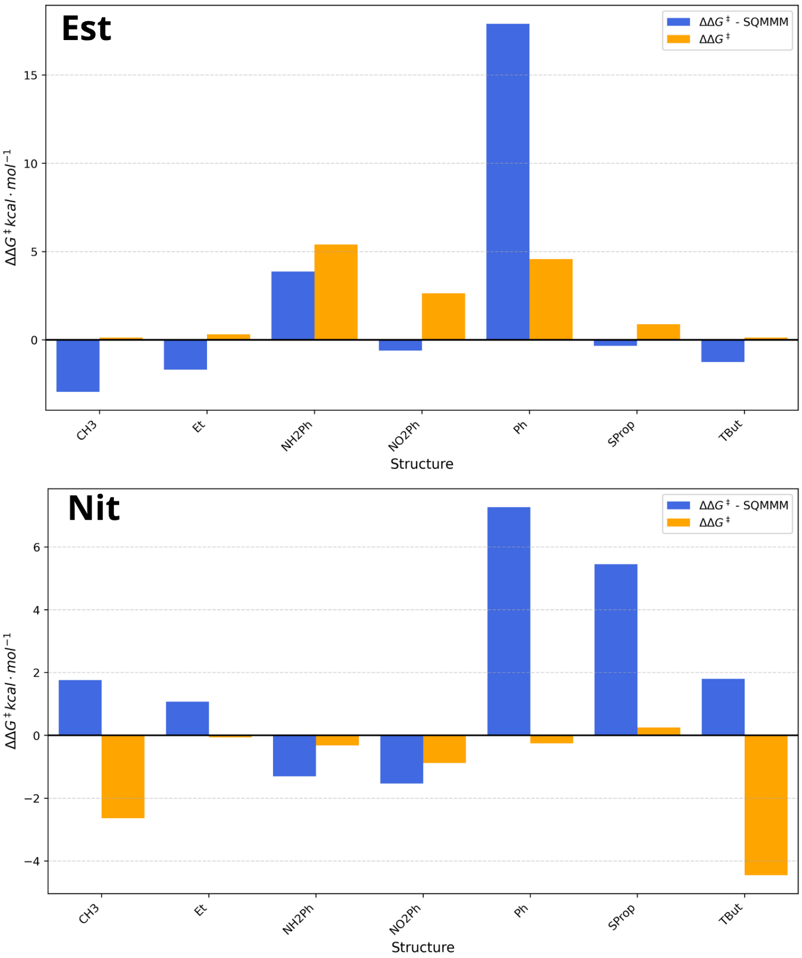

Figure 5.33: Difference in Gibbs free energy of activation for the studied systems in EVE at 373 K, with Grimme quasi-harmonic corrections applied using the GoodVibes package[100]. The results in orange were taken from Oliveira[19,20].

Novel studies on OEEF applications discuss the effect of solvent screening on the OEEF - solute interaction.[23,107,108] This effect, as explained by Dutta Dubey et al.[23], arises from the alignment of solvent molecules with the electric field, which in turn reduces the solute's ability to interact with the field via its dipole moment.

To better comprehend this effect, single-point field calculations at the $M062X/$def2tzvpp level of theory were performed for the E and Z isomers of the Hurd-Claisen systems in EVE. The transition states were aligned with the z-axis, following the reaction axis rule. The results, which illustrate the effective changes in stereoselectivity, are presented in Figure 5.34. The *MoleKing* package was essential for the geometric operations involving the thousands of charge points used in this study, once again highlighting the package's novelty in handling charge point configurations.

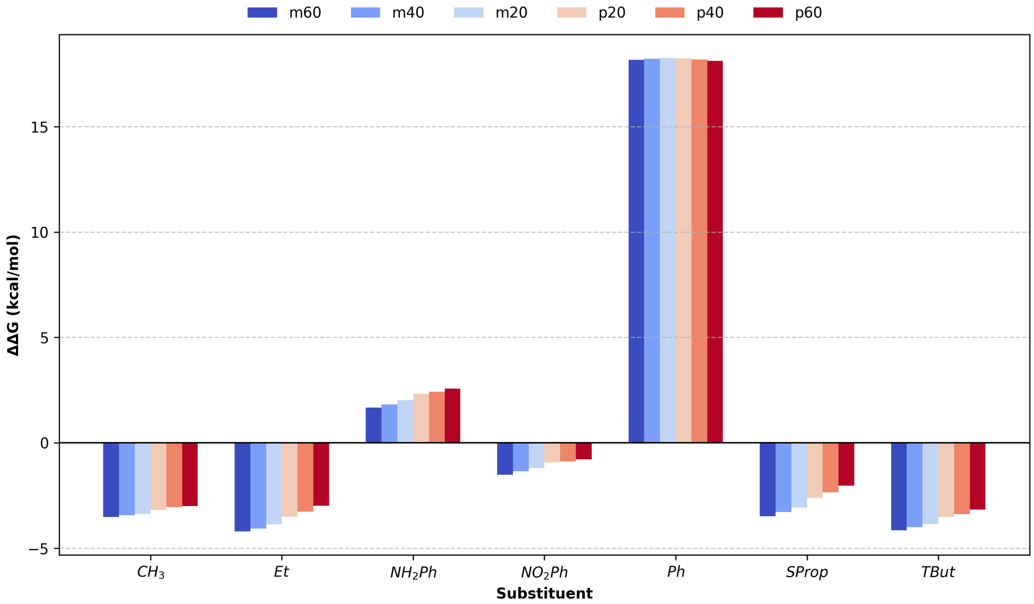

Figure 5.34: Single-point OEEF calculations for the solvated *E* and *Z* isomers of the of the ester containing Hurd-Claisen systems in EVE. The S-QM/MM solvation protocol with the ASEC-FEG approximation was employed at the M06-2X/def2tzvpp level of theory. The electric fields were applied from -6.00×10^{-4} to 6.00×10^{-4} a.u. according to the reaction axis rule.

The results show that, with the exception of the NH_2Ph and *Ph* systems, the *Z* isomer is favored in most cases of the Hurd–Est variation. As the magnitude of the electric field increases, the electronic stabilization of the *E* isomer also increases. However, unlike the trend observed in Figure 5.8, the CH_3 system does not exhibit stereoselectivity inversion under an OEEF. This is because the EVE charge points already provide greater stabilization for the *E* isomer, shifting the natural preference from the axial stereoisomer to an equatorial one, effectively tilting its previously "indecisive" barrier toward *Z*-selectivity. A similar description applies to all ester-containing systems, where the bulk of the energetic change arises from the charge point effects.

The phenyl-substituted reaction, as previously shown, favors the *E* isomer in the presence of solvent. Both positive and negative fields promote a slight stabilization of the *Z* isomer. Therefore, the presence of the electric field counteracts the aforementioned *E* stabilization by altering the overall interaction between the charge points and the solute. However, the effect is not strong enough to negate the CP-induced *E* stabilization, once again demonstrating the aptitude of the OEEF to modulate stereoselectivity only among closely related transition states.

Figure 5.35 presents the results for the Hurd-Nit rearrangement. A clear contrast is observed through the more prominent OEEF effect, with changes in $\Delta\Delta G^{\ddagger}$ reaching up to 1.0 kcal/mol more than in the Hurd-Est rearrangement. Nevertheless, the overall trend remains the same, with solvation dictating the preferred stereoisomer and the OEEF merely modulating the energetic barrier of the transition states. Interestingly, the *Et* rearrangement shows great promise for stereoinversion under highly positive fields.

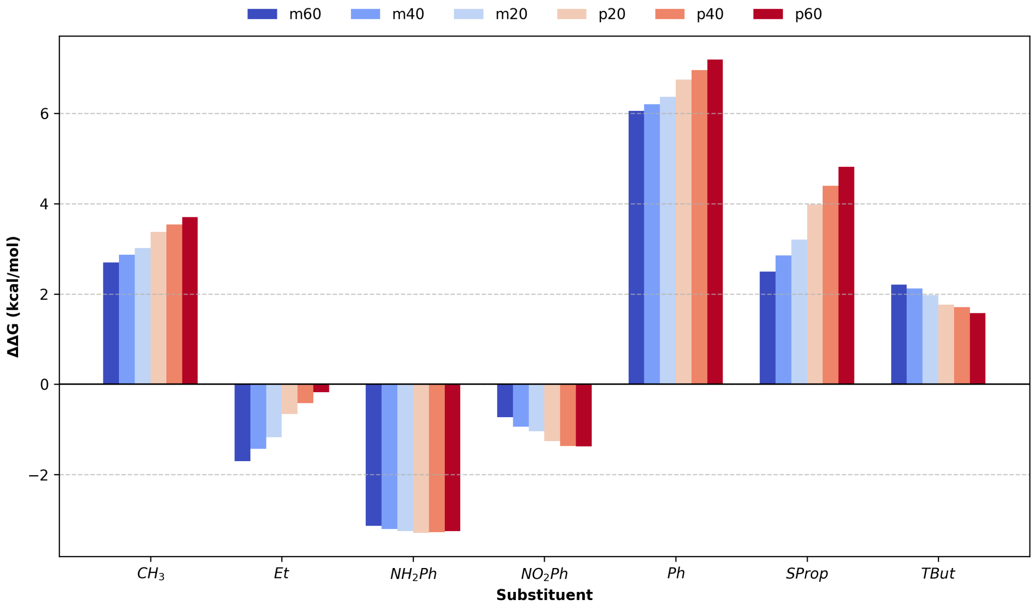

Figure 5.35: Single-point OEEF calculations for the solvated E and Z isomers of the nitrile containing Hurd-Claisen systems in EVE. The S-QM/MM solvation protocol with the ASEC-FEG approximation was employed at the M06-2X/def2tzvpp level of theory. The electric fields were applied from -6.00×10^{-4} to 6.00×10^{-4} a.u. according to the reaction axis rule.

The significant changes in atomic charges introduced by the S-QM/MM methodology exert a strong influence on the catalytic properties of the OEEF, effectively mimicking the solvent screening effect. Thus, the S-QM/MM solvation protocol proves to be a valuable tool for studying the OEEF in the Hurd-Claisen rearrangement at low computational cost.

These results demonstrate that the primary factor governing the interaction between transition states and electric fields is the dipole-field interaction. Consequently, employing a solvation method that accurately captures the system's dipole moment is essential for reliably studying the OEEF in the Hurd-Claisen rearrangement.

Chapter 6

Final Remarks

The effect of oriented external electric fields on the Hurd-Claisen rearrangement was evaluated through a series of computational chemistry simulations. Two orientation rules were applied: the Reaction Axis rule, which aligns the external electric field with the electron flow, and the Molecular Axis orientation, which aligns the two most distant atoms of the molecule along the Z-axis with the external electric field. The results showed that both axis rules effectively induced stereochemical changes in the reaction mechanism.

By applying a negative Z-oriented OEEF to the CH_3 substituent, the standard AX stereopreference was successfully shifted to an EQ preference due to stabilization of the transition state by the external electric field. The heavier isobutyl-substituted rearrangements also exhibited a shift in stereopreference under a positive field. The nitrile-containing Et and $SProp$ systems also underwent a shift in stereopreference, becoming E-dominant.

The molecular axis protocol proved, as expected, to be more reliable in stereocontrol, as many closely related reactions underwent a shift in the preferred isomer, with lower field strengths producing greater changes in the energy barriers—especially in the Hurd-Nit variant. The simulations demonstrated significant potential for stereocontrol in "indecisive" Hurd-Claisen rearrangements, defined as those with small differences in the stability of competing transition states.

The application of the OEEF led to significant changes in reaction rates, as evidenced by variations in the Gibbs free energy differences between the transition states and reactants for the $SProp$, Et, and CH_3 rearrangements. A negative reaction-axis-oriented electric field catalyzed all studied reactions, whereas a positively oriented field strongly inhibited them due to substantial stabilization of the reactants.

As a result of the simulations, the primary effect of the OEEF was the stabilization of transition states through dipole-field interactions, while geometric changes played a passive role. These structural adjustments primarily influenced the electronic distribution, ultimately modifying the molecular dipole moment.

The effect of the solvent on the geometry of the transition state was also evaluated. It was shown to be minimal, with the majority of the stabilization effect also arising from electronic changes in the one-electron integrals rather than significant geometric distortions.

By applying the reaction axis rule to the EVE-solvated systems, the solvent screening effect—which reduces the effective magnitude of the field—was observed. Previously indecisive transition states became Z-dominant. Nevertheless, the application of electric fields was capable of inducing noticeable changes in reaction proportions, with energy variations of up to 2 kcal/mol. However, the solvation effect led to a reduction in the effectiveness of the OEEF, as the solvent screening diminished the effective field strength.

Two additional computational protocols were envisioned to explore experimentally feasible OEEF applications. Firstly, a non-oriented (isotropic) external electric field showed great promise as a tool for controlling reaction mechanisms. Statistically inspired calculations demonstrated that this type of field was able to flip the stereopreference of three studied systems: the Hurd–Nit *Et* and *Ph* systems, and the CH_3-containing ester. By applying weighted means to the Gibbs free energy differences between the transition states and reactants, it was possible to observe a shift in the preferred isomer and emulate solute rotational freedom. While direct "modulation" of stereoselectivity is not achievable by this method, changes in the E/Z ratio are possible, depending on the electrostatic nature of the transition states.

Secondly, the well-discussed gold thiolate model was employed for the CH_3 and *Ph* Hurd–Est rearrangements, where a significant increase in the OEEF effect was observed, along with a flip in both selectivities. The results suggest that using a gold surface to anchor the rotational degrees of freedom of reactive structures can be a promising strategy to enhance the OEEF effect, potentially leading to more pronounced stereochemical control in reactions, with an already well-established experimental protocol.

These findings highlight the potential of OEEFs as versatile tools for controlling reaction mechanisms and stereoselectivity without relying on traditional catalysts. While the study focused on Hurd-Claisen rearrangements, the methodologies developed here can be extended to other pericyclic reactions, and even to complex biochemical systems where electric fields play a functional role, with a low computational cost the hybrid S-QM/MM OEEF method is a promising tool for the study of these systems.

A key methodological contribution of this thesis is the development of the *MoleKing* module, which enabled the automation of molecular manipulations, significantly simplifying the methodological challenges associated with theoretical studies involving OEEF calculations and QM/MM workflows, while enhancing computational efficiency and reducing the potential for human error.

6.1 Perspectives

- Apply the OEEF protocol to other Claisen-type rearrangements, such as the Echenmoser and Johnson variants, to evaluate the generalizability of electric-field-induced stereocontrol across mechanistically related systems.
- Generate reaction pathways for the Hurd-Claisen rearrangement with S-QM/ MM charge points and OEEF by performing Free Energy Gradient calculations with electric field perturbations on the rearrangement products.
- Employ machine learning techniques to predict the influence of non-oriented external electric fields on reaction stereoselectivity, enabling rapid screening of molecular systems based on their electrostatic responsiveness.
- Perform a comprehensive characterization of the solvent screening effect on the studied systems by applying more robust explicit solvation models, such as those derived from molecular dynamics simulations, where not only dispersion and induction interactions are accounted for, but also the simultaneous influence of the external electric field on the solvent environment is explicitly considered.

Bibliography

[1] Tamang, S. R.; Findlater, M. Iron Catalyzed Hydroboration of Aldehydes and Ketones. *The Journal of Organic Chemistry* **2017**, *82*, 12857–12862, PMID: 29083184.

[2] Tamang, S. R.; Bedi, D.; Shafiei-Haghighi, S.; Smith, C. R.; Crawford, C.; Findlater, M. Cobalt-Catalyzed Hydroboration of Alkenes, Aldehydes, and Ketones. *Organic Letters* **2018**, *20*, 6695–6700.

[3] Shegavi, M. L.; Baishya, A.; Geetharani, K.; Bose, S. K. Reusable Fe2O3-nanoparticle catalysed efficient and selective hydroboration of carbonyl compounds. *Org. Chem. Front.* **2018**, *5*, 3520–3525.

[4] Arévalo, R.; Vogels, C. M.; MacNeil, G. A.; Riera, L.; Pérez, J.; Westcott, S. A. Rhenium-catalysed hydroboration of aldehydes and aldimines. *Dalton Trans.* **2017**, *46*, 7750–7757.

[5] Newland, R. J.; Lynam, J. M.; Mansell, S. M. Small bite-angle 2-phosphinophosphinine ligands enable rhodium-catalysed hydroboration of carbonyls. *Chem. Commun.* **2018**, *54*, 5482–5485.

[6] Weidner, V. L.; Barger, C. J.; Delferro, M.; Lohr, T. L.; Marks, T. J. Rapid, Mild, and Selective Ketone and Aldehyde Hydroboration/Reduction Mediated by a Simple Lanthanide Catalyst. *ACS Catalysis* **2017**, *7*, 1244–1247.

[7] Yan, D.; Dai, P.; Chen, S.; Xue, M.; Yao, Y.; Shen, Q.; Bao, X. Highly efficient hydroboration of carbonyl compounds catalyzed by tris(methylcyclopentadienyl)lanthanide complexes. *Org. Biomol. Chem.* **2018**, *16*, 2787–2791.

[8] Ghatak, T.; Makarov, K.; Fridman, N.; Eisen, M. S. Catalytic regeneration of a Th–H bond from a Th–O bond through a mild and chemoselective carbonyl hydroboration. *Chem. Commun.* **2018**, *54*, 11001–11004.

[9] Osseili, H.; Mukherjee, D.; Spaniol, T. P.; Okuda, J. Ligand Influence on Carbonyl Hydroboration Catalysis by Alkali Metal Hydridotriphenylborates [(L)M][HBPh3] (M=Li, Na, K). *Chemistry - A European Journal* **2017**, *23*, 14292–14298.

[10] Robertson, J.; Coote, M.; Bissember, A. Synthetic applications of light, electricity, mechanical force and flow. *Nature Reviews Chemistry* **2019**, *3*, 290–304.

[11] Ciampi, S.; Darwish, N.; Aitken, H. M.; Díez-Pérez, I.; Coote, M. L. Harnessing electrostatic catalysis in single molecule, electrochemical and chemical systems: a rapidly growing experimental tool box. *Chem. Soc. Rev.* **2018**, *47*, 5146–5164.

[12] Aragonès, A. C.; Haworth, N. L.; Darwish, N.; Ciampi, S.; Mannix, E. J.; Wallace, G. G.; Diez-Perez, I.; Coote, M. L. Electrostatic catalysis of a Diels-Alder reaction. *Nature* **2016**, *531*, 88–91.

[13] Gorin, C. F.; Beh, E. S.; Bui, Q. M.; Dick, G. R.; Kanan, M. W. Interfacial Electric Field Effects on a Carbene Reaction Catalyzed by Rh Porphyrins. *Journal of the American Chemical Society* **2013**, *135*, 11257–11265, PMID: 23837635.

[14] Gorin, C. F.; Beh, E. S.; Kanan, M. W. An Electric Field–Induced Change in the Selectivity of a Metal Oxide–Catalyzed Epoxide Rearrangement. *Journal of the American Chemical Society* **2012**, *134*, 186–189, PMID: 22191979.

[15] Shaik, S. My Vision of Electric-Field-Aided Chemistry in 2050. *ACS Physical Chemistry Au* **2024**, *4*, 191–201.

[16] Wang, Z.; Danovich, D.; Ramanan, R.; Shaik, S. Oriented-External Electric Fields Create Absolute Enantioselectivity in Diels-Alder Reactions: Importance of the Molecular Dipole Moment. *Journal of the American Chemical Society* **2018**, *140*, 13350–13359.

[17] Silva, V. S.; Tolentino, T. A.; Rodrigues, T. C. A. F.; Santos, F. F. M.; Machado, D. F. S.; Silva, W. A.; Oliveira, H. C. B. d.; Machado, A. H. L. Unprecedented E-stereoselectivity on the sigmatropic Hurd-Claisen rearrangement of Morita-Baylis-Hillman adducts: a joint experimental-theoretical study. *Org. Biomol. Chem.* **2019**, *17*, 4498–4511.

[18] Basavaiah, D.; Pandiaraju, S.; Krishnamacharyulu, M. Unprecedented Stereochemical Reversal from Alkyl to Aryl Substituents in the Johnson-Claisen Rearrangement of Methyl 3-Hydroxy-2-methylenealkanoates. *Synlett* **1996**, *1996*, 747–748.

[19] Oliveira, A. G. C.; Barbosa, M. R.; Matias, P. H. F.; Silva, C. A. L.; Machado, D. F. S.; de Lira Machado, A. H.; Benedito de Oliveira, H. C. Deciphering Stereoselectivity in

Hurd-Claisen Rearrangements: A Comprehensive Study of Electrostatic Interactions from Shubin's Energy Decomposition Analysis. *ChemPhysChem* **2024**, *25*.

[20] Oliveira, A. G. C. Deciphering The Stereoselectivity of Claisen Rearrangements: Joint Density Functional Theory and Machine Learning Models. Ph.D. thesis, Universidade Fedral de Goiás, Goiânia, 2024.

[21] Shaik, S.; Ramanan, R.; Danovich, D.; Mandal, D. Structure and reactivity/selectivity control by oriented-external electric fields. *Chem. Soc. Rev.* **2018**, *47*, 5125–5145.

[22] Zhang, M.-X.; Xu, H.-L.; Su, Z.-M. The directions of an external electric field control the catalysis of the hydroboration of C–O unsaturated compounds. *RSC Adv.* **2019**, *9*, 29331–29336.

[23] Dutta Dubey, K.; Stuyver, T.; Kalita, S.; Shaik, S. Solvent Organization and Rate Regulation of a Menshutkin Reaction by Oriented External Electric Fields are Revealed by Combined MD and QM/MM Calculations. *Journal of the American Chemical Society* **2020**, *142*, 9955–9965, PMID: 32369357.

[24] Coutinho, K.; Canuto, S. DICE: A Monte Carlo Program for Molecular Liquid Simulation. 1997.

[25] Coutinho, K.; Canuto, S. In *Solvent Effects from a Sequential Monte Carlo - Quantum Mechanical Approach*; Löwdin, P.-O., Sabin, J. R., Zerner, M. C., Karwowski, J., Karelson, M., Eds.; Advances in Quantum Chemistry; Academic Press, 1997; Vol. 28; pp 89 – 105.

[26] Georg, H. C.; Coutinho, K.; Canuto, S. Converged electronic polarization of acetone in liquid water and the role in the n–pi transition. *Chemical Physics Letters* **2006**, *429*, 119 – 123.

[27] Coutinho, K.; Georg, H.; Fonseca, T.; Ludwig, V.; Canuto, S. An efficient statistically converged average configuration for solvent effects. *Chemical Physics Letters* **2007**, *437*, 148 – 152.

[28] Okuyama-Yoshida, N.; Kataoka, K.; Nagaoka, M.; Yamabe, T. Structure optimization via free energy gradient method: Application to glycine zwitterion in aqueous solution. *The Journal of Chemical Physics* **2000**, *113*, 3519–3524.

[29] Franco, L. R.; Brandão, I.; Fonseca, T. L.; Georg, H. C. Elucidating the structure of merocyanine dyes with the ASEC-FEG method. Phenol blue in solution. *The Journal of Chemical Physics* **2016**, *145*, 194301.

[30] Ramanan, R.; Danovich, D.; Mandal, D.; Shaik, S. Catalysis of Methyl Transfer Reactions by Oriented External Electric Fields: Are Gold–Thiolate Linkers Innocent? *Journal of the American Chemical Society* **2018**, *140*, 4354–4362, PMID: 29512385.

[31] Georg, H. C.; Canuto, S. DicePlayer. 2008.

[32] Lee, H.; Kim, K. T.; Kim, M.; Kim, C. Recent Advances in Catalytic [3,3]-Sigmatropic Rearrangements. *Catalysts* **2022**, *12*.

[33] IUPAC Golden Book Of Definitions. **2019**,

[34] Valverde, D.; Georg, H. C.; Canuto, S. Free-Energy Landscape of the SN2 Reaction CH3Br + Cl– → CH3Cl + Br– in Different Liquid Environments. *The Journal of Physical Chemistry B* **2022**, *126*, 3685–3692, PMID: 35543431.

[35] Anslyn, E.; Dougherty, D. *Modern Physical Organic Chemistry*; G - Reference,Information and Interdisciplinary Subjects Series; University Science Books, 2006.

[36] Peters, B. In *Reaction Rate Theory and Rare Events Simulations*; Peters, B., Ed.; Elsevier: Amsterdam, 2017; pp 227–271.

[37] Pelzer, H.; Wigner, E. P. In *Part I: Physical Chemistry. Part II: Solid State Physics*; Wightman, A. S., Ed.; Springer Berlin Heidelberg: Berlin, Heidelberg, 1997; pp 69–95.

[38] Evans, M. G.; Polanyi, M. Inertia and driving force of chemical reactions. *Trans. Faraday Soc.* **1938**, *34*, 11–24.

[39] Marsden, S. R.; Mestrom, L.; McMillan, D. G. G.; Hanefeld, U. Thermodynamically and Kinetically Controlled Reactions in Biocatalysis - from Concepts to Perspectives. *ChemCatChem* **2020**, *12*, 426–437.

[40] Carey, F.; Sundberg, R. *Advanced Organic Chemistry: Part B: Reaction and Synthesis*; Advanced Organic Chemistry; Springer US, 2007.

[41] Szabo, A.; Ostlund, N. *Modern Quantum Chemistry: Introduction to Advanced Electronic Structure Theory*; Dover Books on Chemistry; Dover Publications, 1996.

[42] Hartree, D. R. The Wave Mechanics of an Atom with a Non-Coulomb Central Field. Part I. Theory and Methods. *Mathematical Proceedings of the Cambridge Philosophical Society* **1928**, *24*, 89–110.

[43] Fock, V. Näherungsmethode zur Lösung des quantenmechanischen Mehrkörperproblems. *Zeitschrift für Physik A Hadrons and Nuclei* **1930**, *61*, 126–148.

[44] Lopes, T. O. Bond Ellipticity Alternation: An Accurate Descriptor of the Nonlinear Optical Properties of pi-Conjugated Chromophores. Ph.D. thesis, Universidade de Brasília, Brasília, 2017.

[45] Levine, I. *Quantum chemistry*; Allyn and Bacon chemistry series; Prentice Hall, 2006.

[46] Moller, C.; Plesset, M. S. Note on an Approximation Treatment for Many-Electron Systems. *Phys. Rev.* **1934**, *46*, 618–622.

[47] Thomas, L. H. The calculation of atomic fields. *Mathematical Proceedings of the Cambridge Philosophical Society* **1927**, *23*, 542–548.

[48] Un Metodo Statistico per la Determinazione di alcune Priopriatà dell'Atomo. *Accademia Nazionale dei Lincei* **1927**, *6*, 602–607.

[49] Tsuneda, T. *Density Functional Theory in Quantum Chemistry*; SpringerLink : Bücher; Springer Japan, 2014.

[50] Hohenberg, P.; Kohn, W. Inhomogeneous Electron Gas. *Phys. Rev.* **1964**, *136*, B864–B871.

[51] Tsuneda, T. Density Functional Theory in Quantum Chemistry. *Density Functional Theory in Quantum Chemistry* **2013**, 1–200.

[52] Machado, D. F. S. Desenvolvimento de métodos físicamente inspirados para cálculos de ótica não-linear e efeitos de solventes nas propriedades óticas não-lineares em derivados de azo-enaminonas. Ph.D. thesis, Universidade de Brasília, Brasília, 2017.

[53] Koch, W.; Holthausen, M. C. *A Chemist's Guide to Density Functional Theory*; Wiley - VCH: Weinheim - New York, 2nd edition, 2001.

[54] Kohn, W.; Sham, L. J. Self-Consistent Equations Including Exchange and Correlation Effects. *Phys. Rev.* **1965**, *140*, A1133–A1138.

[55] Cramer, C. *Essentials of Computational Chemistry: Theories and Models*; Wiley, 2005.

[56] Parr, R.; Weitao, Y. *Density-Functional Theory of Atoms and Molecules*; International Series of Monographs on Chemistry; Oxford University Press, 1994.

[57] Stephens, P. J.; Devlin, F. J.; Ashvar, C. S.; Chabalowski, C. F.; Frisch, M. J. Theoretical calculation of vibrational circular dichroism spectra. *Faraday Discuss.* **1994**, *99*, 103–119.

[58] Perdew, J. P.; Burke, K.; Ernzerhof, M. Generalized Gradient Approximation Made Simple. *Phys. Rev. Lett.* **1996**, *77*, 3865–3868.

[59] Besalú-Sala, P.; Sitkiewicz, S. P.; Salvador, P.; Matito, E.; Luis, J. M. A new tuned range-separated density functional for the accurate calculation of second hyperpolarizabilities. *Phys. Chem. Chem. Phys.* **2020**, *22*, 11871–11880.

[60] Yanai, T.; Tew, D. P.; Handy, N. C. A new hybrid exchange–correlation functional using the Coulomb-attenuating method (CAM-B3LYP). *Chemical Physics Letters* **2004**, *393*, 51–57.

[61] Koch, W. *A Chemist's Guide to Density Functional Theory*; Wiley VCH, 2001.

[62] Janak, J. F. Proof that $\frac{\partial E}{\partial n_i} = \varepsilon$ in density-functional theory. *Phys. Rev. B* **1978**, *18*, 7165–7168.

[63] Vianna, J.; Fazzio, A.; Canuto, S. *Teoria quântica de moléculas e sólidos: simulação computacional*; Livraria da Física, 2004.

[64] Matias, P. H. Enhancing accuracy in predicting optical properties of explicitly solvated systems: a comprehensive approach through long-range separated tuning of RSH functional and sequential QM/MM. Ph.D. thesis, Universidade Fedral de Goiás, Goiânia, 2023.

[65] Zhao, Y.; Truhlar, D. G. The M06 suite of density functionals for main group thermochemistry, thermochemical kinetics, noncovalent interactions, excited states, and transition elements: two new functionals and systematic testing of four M06-class

functionals and 12 other functionals. *Theoretical Chemistry Accounts* **2008**, *120*, 215–241.

[66] de Queiroz, T. B.; Kümmel, S. Charge-transfer excitations in low-gap systems under the influence of solvation and conformational disorder: Exploring range-separation tuning. *The Journal of Chemical Physics* **2014**, *141*, 084303.

[67] Georg, H. C.; Canuto, S. Electronic Properties of Water in Liquid Environment. A Sequential QM/MM Study Using the Free Energy Gradient Method. *The Journal of Physical Chemistry B* **2012**, *116*, 11247–11254, PMID: 22894550.

[68] Díaz, M. S.; Freile, M. L.; Gutiérrez, M. I. Solvent effect on the UV/Vis absorption and fluorescence spectroscopic properties of berberine. *Photochem. Photobiol. Sci.* **2009**, *8*, 970–974.

[69] Machado, D. F. S.; Lopes, T. O.; Lima, I. T.; da Silva Filho, D. A.; de Oliveira, H. C. B. Strong Solvent Effects on the Nonlinear Optical Properties of Z and E Isomers from Azo-Enaminone Derivatives. *The Journal of Physical Chemistry C* **2016**, *120*, 17660–17669.

[70] Tomasi, J.; Mennucci, B.; Cancès, E. The IEF version of the PCM solvation method: an overview of a new method addressed to study molecular solutes at the QM ab initio level. *Journal of Molecular Structure: THEOCHEM* **1999**, *464*, 211–226.

[71] Mennucci, B.; Tomasi, J.; Cammi, R.; Cheeseman, J. R.; Frisch, M. J.; Devlin, F. J.; Gabriel, S.; Stephens, P. J. Polarizable Continuum Model (PCM) Calculations of Solvent Effects on Optical Rotations of Chiral Molecules. *The Journal of Physical Chemistry A* **2002**, *106*, 6102–6113.

[72] Barbosa, M. R.; Costa, I. S. D.; Lopes, T. O.; Valverde, C.; Machado, D. F. S.; Oliveira, H. C. B. d. Theoretical Model of Polarization Effects on Third-Order NLO Properties of the Stilbazolium Derivative Crystal. *The Journal of Physical Chemistry A* **2022**, *126*, 8901–8909, PMID: 36441960.

[73] Valverde, C.; Osório, F. A.; Fonseca, T. L.; Baseia, B. DFT study of third-order nonlinear susceptibility of a chalcone crystal. *Chemical Physics Letters* **2018**, *706*, 170–174.

[74] Metropolis, N.; Rosenbluth, A. W.; Rosenbluth, M. N.; Teller, A. H.; Teller, E. Equation of State Calculations by Fast Computing Machines. *The Journal of Chemical Physics* **1953**, *21*, 1087–1092.

[75] Coutinho, K. *Metodo Monte Carlo Aplicado a Simulacao de Liquidos*; Livro de Resumos; VII Escola Brasileira de Estrutura Eletronica, 2000; pp 48–73.

[76] Torres, E.; Georg, H.; Fonseca, T.; Castro, M. First hyperpolarizability of isomers of pyridinium N-phenoxide betaine dye in solution using the ASEC-FEG method. *Chemical Physics Letters* **2018**, *699*, 261 – 266.

[77] Jaramillo, P.; Coutinho, K.; Canuto, S. Continuum, discrete, and explicit solvation models for describing the low-lying absorption spectrum of the pterin acid in aqueous environment. *International Journal of Quantum Chemistry* **2010**, *110*, 2371–2377.

[78] Canuto, S. *Solvation Effects on Molecules and Biomolecules: Computational Methods and Applications*; Challenges and Advances in Computational Chemistry and Physics; Springer Netherlands, 2010.

[79] Gester, R. M.; Georg, H. C.; Canuto, S.; Caputo, M. C.; Provasi, P. F. NMR Chemical Shielding and Spin-Spin Coupling Constants of Liquid NH3: A Systematic Investigation using the Sequential QM/MM Method. *The Journal of Physical Chemistry A* **2009**, *113*, 14936–14942, PMID: 19746949.

[80] Leszczynski, J.; Shukla, M. *Practical Aspects of Computational Chemistry III*; Springer US, 2016.

[81] Frisch, M. J. et al. Gaussian~16 Revision C.01. 2016; Gaussian Inc. Wallingford CT.

[82] Shaik, S.; de Visser, S. P.; Kumar, D. External Electric Field Will Control the Selectivity of Enzymatic-Like Bond Activations. *Journal of the American Chemical Society* **2004**, *126*, 11746–11749, PMID: 15366922.

[83] Lee, H.; Kim, K. T.; Kim, M.; Kim, C. Recent Advances in Catalytic [3,3]-Sigmatropic Rearrangements. *Catalysts* **2022**, *12*.

[84] Rodrigues, T.; Silva, W.; Machado, A. Recent Advances in the Asymmetric Claisen Rearrangement Promoted by Chiral Organometallic Lewis Acids or Organic Brønsted-Lowry Acids. *Current Organic Synthesis* **2015**, *12*, 795.

[85] Peng, Q.; Duarte, F.; Paton, R. S. Computing organic stereoselectivity - from concepts to quantitative calculations and predictions. *Chem. Soc. Rev.* **2016**, *45*, 6093–6107.

[86] Xu, X.; Alecu, I. M.; Truhlar, D. G. How Well Can Modern Density Functionals Predict Internuclear Distances at Transition States? *Journal of Chemical Theory and Computation* **2011**, *7*, 1667–1676, PMID: 26596431.

[87] Zhao, Y.; Truhlar, D. G. The M06 suite of density functionals for main group thermochemistry, thermochemical kinetics, noncovalent interactions, excited states, and transition elements: two new functionals and systematic testing of four M06-class functionals and 12 other function. *Theoretical Chemistry Accounts* **2008**, *120*, 215–241.

[88] Villard, J.; Rothlisberger, U. Structure and dynamics of liquid water from ab initio simulations: Adding Minnesota density functionals to Jacob's ladder. *ChemRxiv* **2023**, no–no.

[89] Liu, F.; Liu, M. An Intuitive Electric-field Contribution Decomposition Model for Chemical Processes and Its Applications on Diels-Alder Reactions. *Chemical Research in Chinese Universities* **2020**, *36*, 1241–1248.

[90] Cezar, H. M.; Coutinho, K.; Canuto, S. DICE version3.0: A Monte Carlo program for molecular liquid simulation. 2018.

[91] Jorgensen, W. L.; Tirado-Rives, J. Potential energy functions for atomic-level simulations of water and organic and biomolecular systems. *Proceedings of the National Academy of Sciences* **2005**, *102*, 6665–6670.

[92] Dodda, L. S.; Vilseck, J. Z.; Tirado-Rives, J.; Jorgensen, W. L. 1.14*CM1A-LBCC: Localized Bond-Charge Corrected CM1A Charges for Condensed-Phase Simulations. *The Journal of Physical Chemistry B* **2017**, *121*, 3864–3870, PMID: 28224794.

[93] Dodda, L. S.; Cabeza de Vaca, I.; Tirado-Rives, J.; Jorgensen, W. L. LigParGen web server: an automatic OPLS-AA parameter generator for organic ligands. *Nucleic Acids Research* **2017**, *45*, W331–W336.

[94] Parrish, R. M. et al. Psi4 1.1: An Open-Source Electronic Structure Program Emphasizing Automation, Advanced Libraries, and Interoperability. *Journal of Chemical Theory and Computation* **2017**, *13*, 3185–3197.

[95] Jensen, F. *Introduction to Computational Chemistry*; Wiley, 2013.

[96] Peng, C.; Ayala, P. Y.; Schlegel, H. B.; Frisch, M. J. Using redundant internal coordinates to optimize equilibrium geometries and transition states. *Journal of Computational Chemistry* **1996**, *17*, 49–56.

[97] Rodrigues, O. Des lois géométriques qui régissent les déplacements d'un système solide dans l'espace, et de la variation des coordonnées provenant de ces déplacements considérés indépendamment des causes qui peuvent les produire. *Journal de Mathématiques Pures et Appliquées* **1840**, *1e série, 5*, 380–440.

[98] Fraiture, L. A History of the Description of the Three-Dimensional Finite Rotation. *The Journal of the Astronautical Sciences* **2009**, *57*, 207–232.

[99] Wang, X.; Wang, H.; Zheng, L.; Zhu, C.; Liang, J.-X. Oriented external electric fields regulating the oxidation reaction of CH catalyzed by Mn-corrolazine. *International Journal of Quantum Chemistry* **2021**, *121*, e26443.

[100] Luchini, G.; Alegre-Requena, J.; Funes-Ardoiz, I.; Paton, R. GoodVibes: automated thermochemistry for heterogeneous computational chemistry data [version 1; peer review: 2 approved with reservations]. *F1000Research* **2020**, *9*.

[101] Truhlar, D. G.; Hase, W. L.; Hynes, J. T. Current status of transition-state theory. *J. Phys. Chem.; (United States)* **1983**, *87:15*.

[102] Bloomfield, V. A. Hydrodynamics in Biophysical Chemistry. *Annual Review of Physical Chemistry* **1977**, *28*, 233–259.

[103] Kurz, G.; Hanebeck, U. D. Stochastic sampling of the hyperspherical von mises–fisher distribution without rejection methods. 2015 Sensor Data Fusion: Trends, Solutions, Applications (SDF). 2015; pp 1–6.

[104] Fisher, R. A. Dispersion on a sphere. *Proceedings of the Royal Society of London. Series A. Mathematical and Physical Sciences* **1953**, *217*, 295–305.

[105] Han, Y.; Lu, K.; Zhang, Q.; Jiao, T.; Gao, Q. Density functional theory study of the effect of external electric field on the degradation of norfloxacin in water by hydroxyl radicals. *Journal of Water Process Engineering* **2025**, *70*, 107031.

[106] Barbosa, M. R. Tratamento explícito do efeito de solvente nas propriedades de óptica não-linear em derivados de chalconas utilizando a metodologia QM/MM sequencial. **2021**,

[107] Alvarado, O.; Alvarado, M.; Medina, F. E.; Cabrera-Pardo, J. R. Effect of oriented external electric fields on the Staudinger $[2+2]$ cycloaddition reaction: a computational study. *Theoretical Chemistry Accounts* **2024**, *144*, 5.

[108] Shaik, S.; Danovich, D.; Joy, J.; Wang, Z.; Stuyver, T. Electric-Field Mediated Chemistry: Uncovering and Exploiting the Potential of (Oriented) Electric Fields to Exert Chemical Catalysis and Reaction Control. *Journal of the American Chemical Society* **2020**, *142*, 12551–12562, PMID: 32551571.

[109] Veríssimo, R. F.; Matias, P. H. F.; Barbosa, M. R.; Neto, F. O. S.; Neto, B. A. D.; de Oliveira, H. C. B. Integrating Machine Learning and SHAP Analysis to Advance the Rational Design of Benzothiadiazole Derivatives with Tailored Photophysical Properties. *Journal of Chemical Information and Modeling* **0**, *0*, null, PMID: 40300554.

[110] Lemos Silva, R. A.; Barbosa, M. R.; Martins, C. R.; Scalabrini Machado, D. F.; Ribeiro, L.; de Oliveira, H. C. B.; da Silva Filho, D. A. (Ro)vibrational Spectroscopic Constants, Lifetime and QTAIM Evaluation of Fullerene Dimers Stability. *Molecules* **2023**, *28*.

Appendix A

Appendix

A.1 RMSD

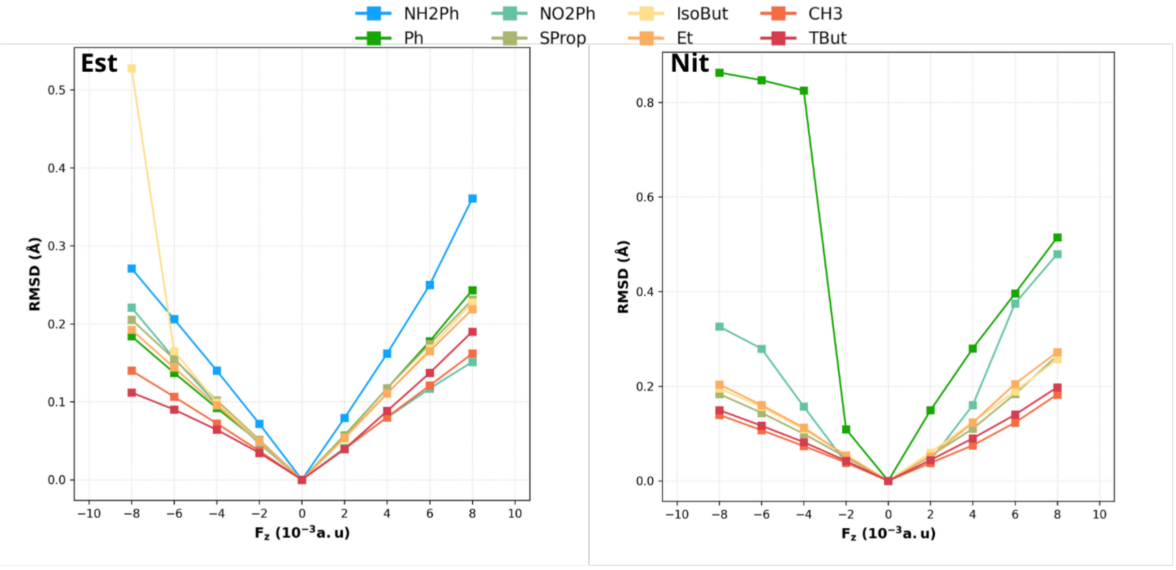

Figure A.1: RMSD of the Hurd-Est rearrangement Transition state, in function of the OEEF. The extremely high RMSD values for same of the bulkier molecues are due to the fact that the OEEF is not able to properly sample the conformational space of these molecules.

A.2 SQMMM Convergence

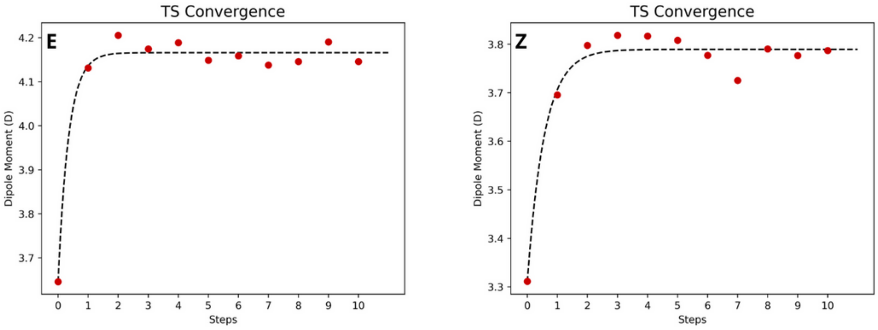

Figure A.2: Dipole convergence of the CH_3 Hurd-Est rearrangement Transition state, in EVE at 373K. This result were obtained at $M062x/def2tzvpp$ level of theory.

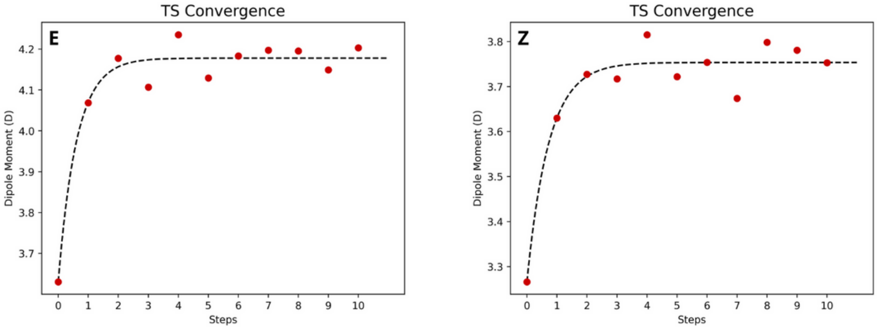

Figure A.3: Dipole convergence of the Et Hurd-Est rearrangement Transition state, in EVE at 373K. This result were obtained at $M062x/def2tzvpp$ level of theory.

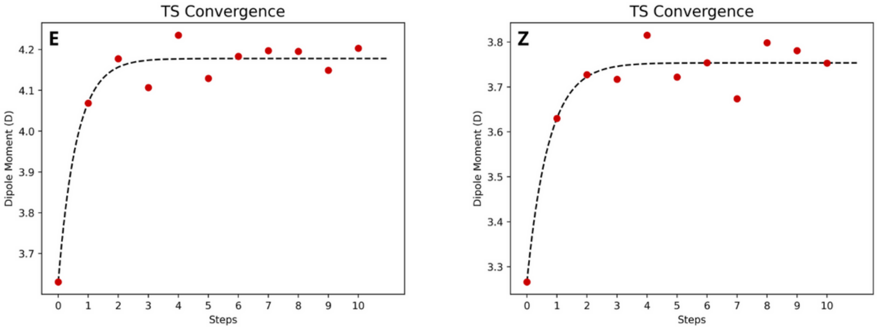

Figure A.4: Dipole convergence of the $SProp$ Hurd-Est rearrangement Transition state, in EVE at 373K. This result were obtained at $M062x/def2tzvpp$ level of theory.

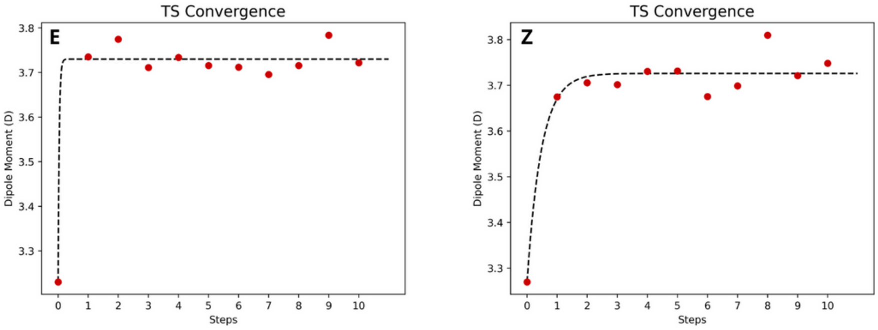

Figure A.5: Dipole convergence of the $TBut$ Hurd-Est rearrangement Transition state, in EVE at 373K. This result were obtained at $M062x/def2tzvpp$ level of theory.

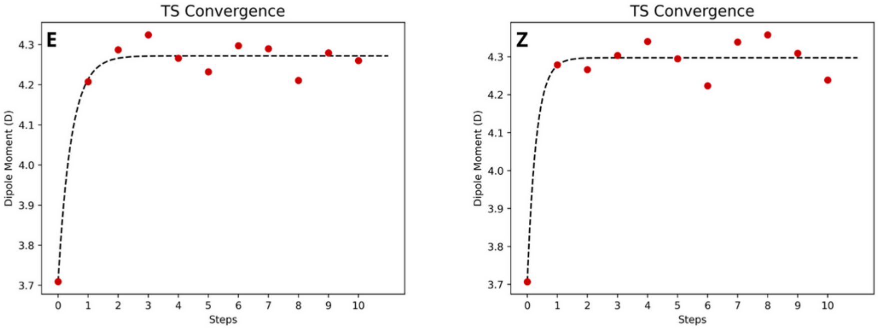

Figure A.6: Dipole convergence of the Ph Hurd-Est rearrangement Transition state, in EVE at 373K. This result were obtained at $M062x/def2tzvpp$ level of theory.

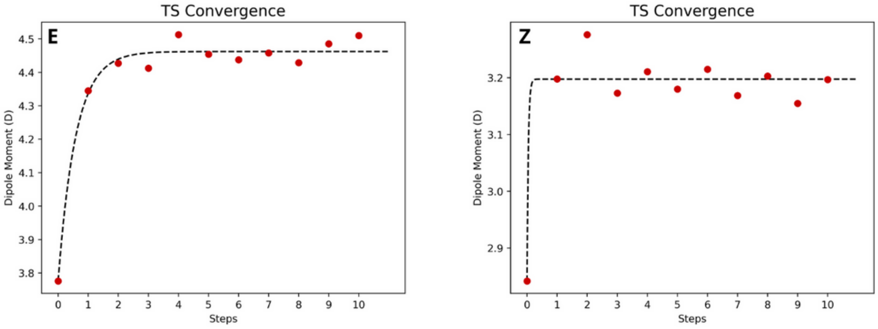

Figure A.7: Dipole convergence of the NH_2Ph Hurd-Est rearrangement Transition state, in EVE at 373K. This result were obtained at $M062x/def2tzvpp$ level of theory.

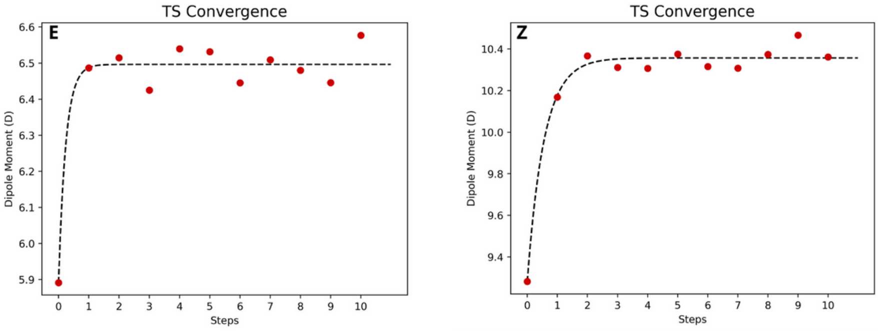

Figure A.8: Dipole convergence of the NO_2Ph Hurd-Est rearrangement Transition state, in EVE at 373K. This result were obtained at $M062x/def2tzvpp$ level of theory.

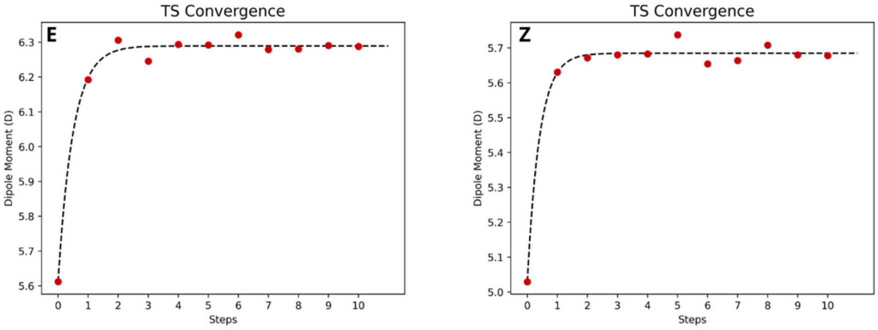

Figure A.9: Dipole convergence of the CH_3 Hurd-Nit rearrangement Transition state, in EVE at 373K. This result were obtained at $M062x/def2tzvpp$ level of theory.

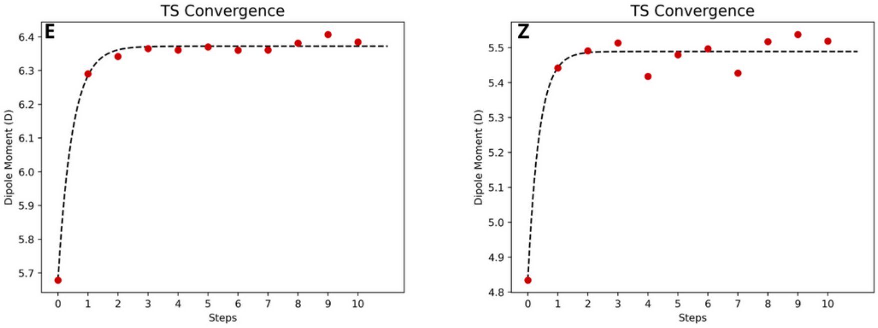

Figure A.10: Dipole convergence of the Et Hurd-Nit rearrangement Transition state, in EVE at 373K. This result were obtained at $M062x/def2tzvpp$ level of theory.

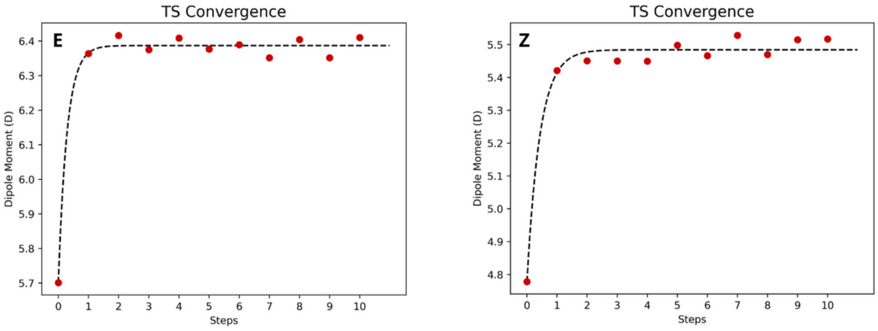

Figure A.11: Dipole convergence of the *Prop* Hurd-Nit rearrangement Transition state, in EVE at 373K. This result were obtained at $M062x/def2tzvpp$ level of theory.

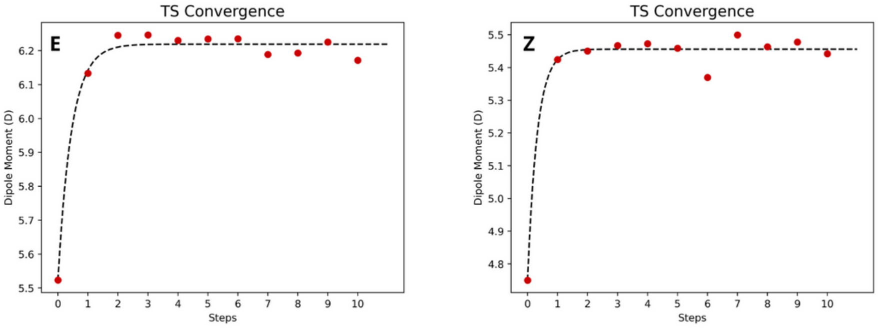

Figure A.12: Dipole convergence of the $TBut$ Hurd-Nit rearrangement Transition state, in EVE at 373K. This result were obtained at $M062x/def2tzvpp$ level of theory.

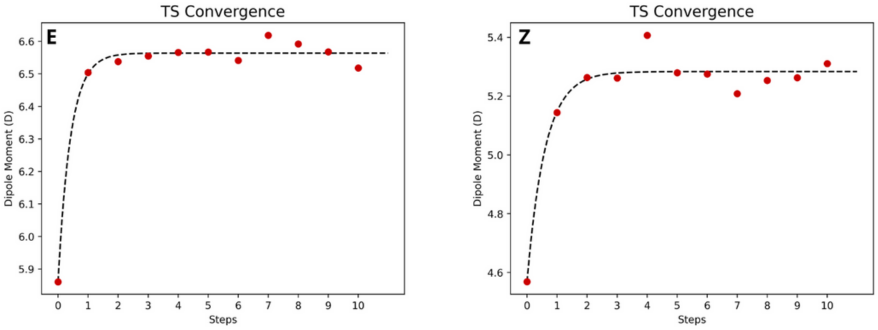

Figure A.13: Dipole convergence of the *Ph* Hurd-Nit rearrangement Transition state, in EVE at 373K. This result were obtained at $M062x/def2tzvpp$ level of theory.

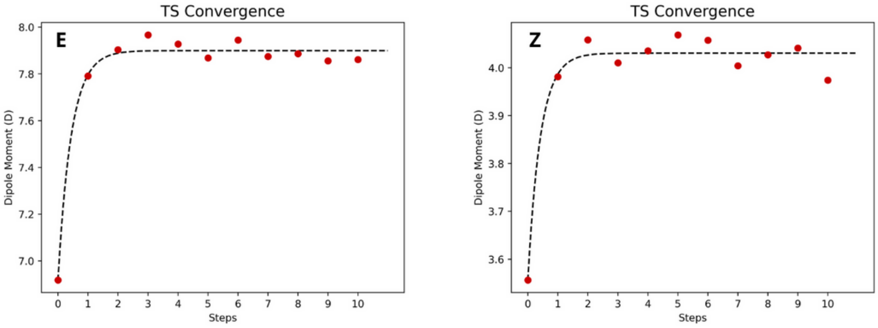

Figure A.14: Dipole convergence of the NH_2Ph Hurd-Nit rearrangement Transition state, in EVE at 373K. This result were obtained at $M062x/def2tzvpp$ level of theory.

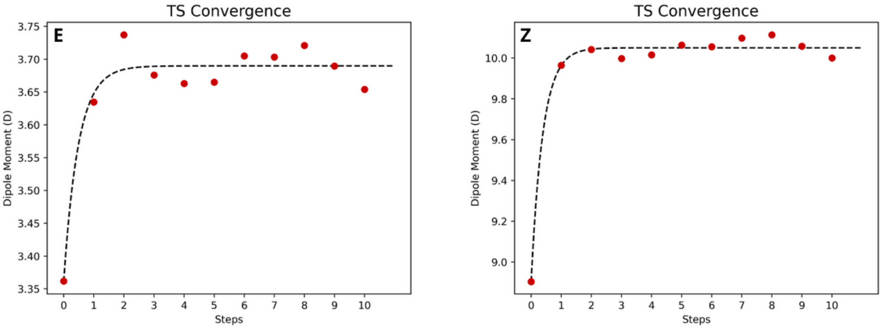

Figure A.15: Dipole convergence of the NO_2Ph Hurd-Nit rearrangement Transition state, in EVE at 373K. This result were obtained at $M062x/def2tzvpp$ level of theory.

A.3 Numeric Values of the Barriers

Table A.1: Thermodinamic Data for the Reaction Axis CH_3 Hurd-Est rearrangement with OEEF magnitude of -8.00×10^{-3} to 8.00×10^{-3} a.u. All units are atomic units.

Iso	Sub	Field	E	ZPE	H	qh-H	T.S	T.qh-S	G(T)	qh-G(T)
Z	CH3	0	-576.95877	0.21203	-576.72617	-576.72812	0.07442	0.07217	-576.80059	-576.80029
Z	CH3	m20	-576.95914	0.21209	-576.72647	-576.72849	0.07435	0.07210	-576.80083	-576.80058
Z	CH3	m40	-576.96012	0.21212	-576.72745	-576.72940	0.07425	0.07203	-576.80170	-576.80143
Z	CH3	m60	-576.96171	0.21211	-576.72911	-576.73106	0.07417	0.07198	-576.80328	-576.80305
Z	CH3	m80	-576.96393	0.21210	-576.73132	-576.73328	0.07409	0.07192	-576.80542	-576.80520
Z	CH3	p20	-576.95902	0.21199	-576.72642	-576.72843	0.07444	0.07221	-576.80085	-576.80064
Z	CH3	p40	-576.95989	0.21187	-576.72734	-576.72936	0.07462	0.07235	-576.80196	-576.80170
Z	CH3	p60	-576.96138	0.21166	-576.72896	-576.73104	0.07507	0.07262	-576.80403	-576.80366
Z	CH3	p80	-576.96352	0.21153	-576.73122	-576.73330	0.07529	0.07278	-576.80651	-576.80608
E	CH3	0	-576.95927	0.21213	-576.72660	-576.72849	0.07416	0.07209	-576.80076	-576.80058
E	CH3	m20	-576.95946	0.21218	-576.72680	-576.72863	0.07404	0.07201	-576.80083	-576.80064
E	CH3	m40	-576.96028	0.21220	-576.72761	-576.72944	0.07397	0.07196	-576.80158	-576.80140
E	CH3	m60	-576.96172	0.21218	-576.72905	-576.73095	0.07397	0.07194	-576.80302	-576.80289
E	CH3	m80	-576.96379	0.21218	-576.73113	-576.73302	0.07392	0.07190	-576.80505	-576.80492
E	CH3	p20	-576.95970	0.21204	-576.72709	-576.72899	0.07434	0.07221	-576.80144	-576.80119
E	CH3	p40	-576.96075	0.21195	-576.72821	-576.73016	0.07448	0.07230	-576.80269	-576.80246
E	CH3	p60	-576.96244	0.21183	-576.72995	-576.73191	0.07461	0.07241	-576.80456	-576.80431
E	CH3	p80	-576.96475	0.21167	-576.73239	-576.73434	0.07478	0.07255	-576.80718	-576.80689

Table A.2: Thermodinamic Data for the Reaction Axis Et Hurd-Est rearrangement with OEEF magnitude of -8.00×10^{-3} to 8.00×10^{-3} a.u. All units are atomic units.

Iso	Sub	Field	E	ZPE	H	qh-H	T.S	T.qh-S	G(T)	qh-G(T)
Z	Et	0	-616.26693	0.23978	-616.00454	-616.00686	0.07914	0.07661	-616.08368	-616.08348
Z	Et	m20	-616.26731	0.23976	-616.00492	-616.00724	0.07928	0.07664	-616.08419	-616.08388
Z	Et	m40	-616.26834	0.23978	-616.00595	-616.00827	0.07919	0.07658	-616.08515	-616.08485
Z	Et	m60	-616.27005	0.23984	-616.00766	-616.00992	0.07888	0.07642	-616.08653	-616.08633
Z	Et	m80	-616.27242	0.23978	-616.01009	-616.01235	0.07889	0.07641	-616.08898	-616.08876
Z	Et	p20	-616.26722	0.23964	-616.00489	-616.00727	0.07938	0.07677	-616.08427	-616.08404
Z	Et	p40	-616.26819	0.23945	-616.00598	-616.00842	0.07991	0.07707	-616.08589	-616.08549
Z	Et	p60	-616.26986	0.23939	-616.00765	-616.01009	0.07974	0.07705	-616.08739	-616.08714
Z	Et	p80	-616.27223	0.23926	-616.01014	-616.01258	0.07998	0.07720	-616.09012	-616.08978
E	Et	0	-616.26752	0.23988	-616.00500	-616.00751	0.07920	0.07647	-616.08420	-616.08398
E	Et	m20	-616.26774	0.23993	-616.00523	-616.00767	0.07904	0.07639	-616.08427	-616.08406
E	Et	m40	-616.26864	0.23994	-616.00613	-616.00857	0.07899	0.07634	-616.08512	-616.08491
E	Et	m60	-616.27021	0.23991	-616.00776	-616.01020	0.07905	0.07635	-616.08680	-616.08655
E	Et	m80	-616.27246	0.23991	-616.01001	-616.01245	0.07896	0.07630	-616.08896	-616.08874
E	Et	p20	-616.26796	0.23982	-616.00551	-616.00802	0.07942	0.07658	-616.08493	-616.08460
E	Et	p40	-616.26909	0.23976	-616.00664	-616.00914	0.07952	0.07667	-616.08615	-616.08581
E	Et	p60	-616.27090	0.23963	-616.00857	-616.01107	0.07961	0.07678	-616.08818	-616.08785
E	Et	p80	-616.27339	0.23945	-616.01119	-616.01369	0.07978	0.07693	-616.09096	-616.09062

Table A.3: Thermodinamic Data for the Reaction Axis *SProp* Hurd-Est rearrangement with OEEF magnitude of -8.00×10^{-3} to 8.00×10^{-3} a.u. All units are atomic units.

Iso	Sub	Field	E	ZPE	H	qh-H	T.S	T.qh-S	G(T)	qh-G(T)
E	SProp	0	-655.57728	0.26728	-655.28529	-655.28804	0.08368	0.08061	-655.36897	-655.36864
E	SProp	m20	-655.57755	0.26728	-655.28556	-655.28831	0.08358	0.08054	-655.36914	-655.36885
E	SProp	m40	-655.57858	0.26724	-655.28665	-655.28933	0.08370	0.08058	-655.37035	-655.36991
E	SProp	m60	-655.58037	0.26719	-655.28850	-655.29118	0.08372	0.08057	-655.37222	-655.37176
E	SProp	m80	-655.58293	0.26718	-655.29106	-655.29380	0.08365	0.08052	-655.37471	-655.37433
E	SProp	p20	-655.57777	0.26721	-655.28584	-655.28852	0.08384	0.08072	-655.36968	-655.36924
E	SProp	p40	-655.57901	0.26714	-655.28708	-655.28983	0.08394	0.08081	-655.37102	-655.37064
E	SProp	p60	-655.58102	0.26704	-655.28915	-655.29190	0.08400	0.08089	-655.37316	-655.37278
E	SProp	p80	-655.58379	0.26686	-655.29204	-655.29485	0.08420	0.08104	-655.37624	-655.37590
Z	SProp	0	-655.57650	0.26733	-655.28451	-655.28689	0.08316	0.08056	-655.36767	-655.36745
Z	SProp	m20	-655.57694	0.26736	-655.28494	-655.28732	0.08309	0.08048	-655.36803	-655.36781
Z	SProp	m40	-655.57809	0.26737	-655.28610	-655.28854	0.08306	0.08043	-655.36916	-655.36897
Z	SProp	m60	-655.57997	0.26733	-655.28804	-655.29042	0.08293	0.08036	-655.37096	-655.37078
Z	SProp	m80	-655.58255	0.26730	-655.29068	-655.29306	0.08274	0.08026	-655.37342	-655.37333
Z	SProp	p20	-655.57678	0.26727	-655.28485	-655.28723	0.08330	0.08065	-655.36815	-655.36788
Z	SProp	p40	-655.57779	0.26714	-655.28592	-655.28836	0.08354	0.08082	-655.36946	-655.36918
Z	SProp	p60	-655.57956	0.26698	-655.28775	-655.29025	0.08377	0.08100	-655.37152	-655.37125
Z	SProp	p80	-655.58209	0.26681	-655.29040	-655.29297	0.08416	0.08123	-655.37457	-655.37420

Table A.4: Thermodinamic Data for the Reaction Axis *Tbut* Hurd-Est rearrangement with OEEF magnitude of -8.00×10^{-3} to 8.00×10^{-3} a.u. All units are atomic units.

Iso	Sub	Field	E	ZPE	H	qh-H	T.S	T.qh-S	G(T)	qh-G(T)
Z	TBut	0	-694.88014	0.29452	-694.55886	-694.56136	0.08717	0.08436	-694.64603	-694.64572
Z	TBut	m20	-694.88088	0.29453	-694.55959	-694.56209	0.08718	0.08434	-694.64677	-694.64643
Z	TBut	m40	-694.88234	0.29455	-694.56106	-694.56356	0.08705	0.08424	-694.64810	-694.64780
Z	TBut	m60	-694.88454	0.29453	-694.56331	-694.56581	0.08697	0.08418	-694.65028	-694.64999
Z	TBut	m80	-694.88746	0.29448	-694.56629	-694.56879	0.08693	0.08414	-694.65322	-694.65293
Z	TBut	p20	-694.88014	0.29447	-694.55885	-694.56142	0.08728	0.08445	-694.64614	-694.64587
Z	TBut	p40	-694.88088	0.29442	-694.55965	-694.56216	0.08734	0.08452	-694.64700	-694.64668
Z	TBut	p60	-694.88237	0.29432	-694.56120	-694.56371	0.08752	0.08465	-694.64872	-694.64836
Z	TBut	p80	-694.88462	0.29417	-694.56351	-694.56608	0.08774	0.08481	-694.65126	-694.65089
E	TBut	0	-694.88150	0.29511	-694.55997	-694.56259	0.08660	0.08338	-694.64657	-694.64597
E	TBut	m20	-694.88218	0.29511	-694.56064	-694.56333	0.08657	0.08334	-694.64721	-694.64667
E	TBut	m40	-694.88368	0.29508	-694.56220	-694.56483	0.08655	0.08330	-694.64876	-694.64813
E	TBut	m60	-694.88600	0.29498	-694.56459	-694.56733	0.08680	0.08339	-694.65138	-694.65072
E	TBut	m80	-694.88916	0.29486	-694.56780	-694.57061	0.08731	0.08360	-694.65511	-694.65421
E	TBut	p20	-694.88164	0.29502	-694.56011	-694.56280	0.08689	0.08356	-694.64700	-694.64636
E	TBut	p40	-694.88262	0.29488	-694.56115	-694.56389	0.08713	0.08374	-694.64828	-694.64764
E	TBut	p60	-694.88444	0.29476	-694.56309	-694.56577	0.08721	0.08385	-694.65030	-694.64963
E	TBut	p80	-694.88711	0.29456	-694.56588	-694.56857	0.08746	0.08405	-694.65334	-694.65262

Table A.5: Thermodinamic Data for the Reaction Axis *IsoBut* Hurd-Est rearrangement with OEEF magnitude of -8.00×10^{-3} to 8.00×10^{-3} a.u. All units are atomic units.

Iso	Sub	Field	E	ZPE	H	qh-H	T.S	T.qh-S	G(T)	qh-G(T)
E	IsoBut	0	-694.88339	0.29515	-694.56174	-694.56479	0.08799	0.08420	-694.64973	-694.64899
E	IsoBut	m20	-694.88369	0.29514	-694.56204	-694.56515	0.08802	0.08417	-694.65006	-694.64932
E	IsoBut	m40	-694.88477	0.29509	-694.56312	-694.56629	0.08834	0.08429	-694.65145	-694.65058
E	IsoBut	m60	-694.88666	0.29506	-694.56506	-694.56818	0.08932	0.08475	-694.65438	-694.65293
E	IsoBut	m80	-694.89038	0.29539	-694.56861	-694.57160	0.08764	0.08387	-694.65625	-694.65547
E	IsoBut	p20	-694.88387	0.29510	-694.56222	-694.56533	0.08812	0.08430	-694.65033	-694.64963
E	IsoBut	p40z	-694.88513	0.29500	-694.56354	-694.56665	0.08832	0.08443	-694.65185	-694.65108
E	IsoBut	p60z	-694.88717	0.29491	-694.56564	-694.56875	0.08833	0.08449	-694.65397	-694.65324
E	IsoBut	p80	-694.89000	0.29472	-694.56858	-694.57176	0.08859	0.08467	-694.65717	-694.65643
Z	IsoBut	0	-694.88282	0.29510	-694.56116	-694.56427	0.08786	0.08428	-694.64902	-694.64855
Z	IsoBut	m20	-694.88295	0.29507	-694.56135	-694.56441	0.08795	0.08430	-694.64930	-694.64871
Z	IsoBut	m40	-694.88386	0.29515	-694.56227	-694.56526	0.08773	0.08415	-694.64999	-694.64940
Z	IsoBut	m60	-694.88555	0.29520	-694.56396	-694.56695	0.08745	0.08397	-694.65141	-694.65092
Z	IsoBut	m80	-694.88803	0.29522	-694.56643	-694.56936	0.08728	0.08386	-694.65371	-694.65322
Z	IsoBut	p20	-694.88348	0.29495	-694.56195	-694.56506	0.08814	0.08447	-694.65009	-694.64953
Z	IsoBut	p40	-694.88494	0.29483	-694.56347	-694.56658	0.08834	0.08463	-694.65180	-694.65121
Z	IsoBut	p60	-694.88720	0.29467	-694.56579	-694.56902	0.08856	0.08479	-694.65435	-694.65381
Z	IsoBut	p80	-694.89027	0.29444	-694.56904	-694.57228	0.08890	0.08501	-694.65794	-694.65729

Table A.6: Thermodinamic Data for the Reaction Axis *Ph* Hurd-Est rearrangement with OEEF magnitude of -8.00×10^{-3} to 8.00×10^{-3} a.u. All units are atomic units.

Iso	Sub	Field	E	ZPE	H	qh-H	T.S	T.qh-S	G(T)	qh-G(T)
E	Ph	0	-768.69021	0.26387	-768.40078	-768.40377	0.08655	0.08276	-768.48733	-768.48652
E	Ph	m20	-768.69062	0.26393	-768.40113	-768.40412	0.08636	0.08264	-768.48748	-768.48676
E	Ph	m40	-768.69185	0.26389	-768.40242	-768.40542	0.08639	0.08263	-768.48881	-768.48805
E	Ph	m60	-768.69392	0.26383	-768.40456	-768.40755	0.08646	0.08265	-768.49102	-768.49020
E	Ph	m80	-768.69685	0.26378	-768.40754	-768.41053	0.08653	0.08266	-768.49407	-768.49319
E	Ph	p20	-768.69063	0.26374	-768.40126	-768.40431	0.08682	0.08292	-768.48807	-768.48722
E	Ph	p40	-768.69188	0.26367	-768.40258	-768.40563	0.08688	0.08299	-768.48946	-768.48862
E	Ph	p60	-768.69398	0.26356	-768.40474	-768.40779	0.08698	0.08309	-768.49171	-768.49088
E	Ph	p80	-768.69694	0.26339	-768.40776	-768.41087	0.08723	0.08327	-768.49499	-768.49414
Z	Ph	0	-768.68220	0.26351	-768.39295	-768.39613	0.08813	0.08357	-768.48108	-768.47970
Z	Ph	m20	-768.68265	0.26356	-768.39334	-768.39652	0.08830	0.08358	-768.48165	-768.48010
Z	Ph	m40	-768.68490	0.26332	-768.39578	-768.39901	0.08779	0.08338	-768.48356	-768.48239
Z	Ph	m60	-768.68719	0.26335	-768.39807	-768.40124	0.08752	0.08323	-768.48559	-768.48448
Z	Ph	m80	-768.69022	0.26334	-768.40116	-768.40434	0.08748	0.08319	-768.48865	-768.48753
Z	Ph	p20	-768.68270	0.26349	-768.39345	-768.39656	0.08771	0.08344	-768.48117	-768.48000
Z	Ph	p40	-768.68411	0.26333	-768.39499	-768.39810	0.08817	0.08375	-768.48316	-768.48185
Z	Ph	p60	-768.68646	0.26319	-768.39740	-768.40057	0.08820	0.08383	-768.48560	-768.48440
Z	Ph	p80	-768.68974	0.26296	-768.40087	-768.40398	0.08829	0.08398	-768.48916	-768.48796

Table A.7: Thermodinamic Data for the Reaction Axis NH_2Ph Hurd-Est rearrangement with OEEF magnitude of -8.00×10^{-3} to 8.00×10^{-3} a.u. All units are atomic units.

Iso	Sub	Field	E	ZPE	H	qh-H	T.S	T.qh-S	G(T)	qh-G(T)
E	NH2	0	-824.05252	0.27995	-823.74465	-823.74789	0.09144	0.08731	-823.83609	-823.83520
E	NH2	m20	-824.05211	0.27993	-823.74425	-823.74749	0.09141	0.08731	-823.83566	-823.83479
E	NH2	m40	-824.05266	0.27992	-823.74486	-823.74803	0.09143	0.08728	-823.83629	-823.83531
E	NH2	m60	-824.05416	0.27982	-823.74642	-823.74966	0.09156	0.08737	-823.83798	-823.83702
E	NH2	m80	-824.05665	0.27980	-823.74891	-823.75215	0.09159	0.08736	-823.84050	-823.83951
E	NH2	p20	-824.05386	0.27991	-823.74600	-823.74924	0.09162	0.08742	-823.83762	-823.83666
E	NH2	p40	-824.05618	0.27986	-823.74831	-823.75161	0.09167	0.08748	-823.83998	-823.83909
E	NH2	p60	-824.05948	0.27971	-823.75174	-823.75504	0.09198	0.08768	-823.84372	-823.84272
E	NH2	p80	-824.06386	0.27949	-823.75624	-823.75960	0.09227	0.08792	-823.84852	-823.84752
Z	NH2	0	-824.04345	0.28828	-823.72777	-823.73112	0.09146	0.08681	-823.81923	-823.81793
Z	NH2	m20	-824.04318	0.28840	-823.72744	-823.73076	0.09085	0.08645	-823.81830	-823.81721
Z	NH2	m40	-824.04407	0.28829	-823.72841	-823.73177	0.09126	0.08662	-823.81968	-823.81838
Z	NH2	m60	-824.04604	0.28834	-823.73085	-823.73378	0.08820	0.08498	-823.81905	-823.81877
Z	NH2	m80	-824.04879	0.28826	-823.73364	-823.73660	0.08831	0.08506	-823.82196	-823.82165
Z	NH2	p20	-824.04493	0.28818	-823.72931	-823.73266	0.09142	0.08688	-823.82073	-823.81954
Z	NH2	p40	-824.04759	0.28801	-823.73206	-823.73544	0.09167	0.08707	-823.82374	-823.82251
Z	NH2	p60	-824.05144	0.28782	-823.73603	-823.73946	0.09199	0.08728	-823.82802	-823.82674
Z	NH2	p80	-824.05665	0.28752	-823.74139	-823.74488	0.09270	0.08778	-823.83409	-823.83267

Table A.8: Thermodinamic Data for the Reaction Axis NO_2Ph Hurd-Est rearrangement with OEEF magnitude of -8.00×10^{-3} to 8.00×10^{-3} a.u. All units are atomic units.

Iso	Sub	Field	E	ZPE	H	qh-H	T.S	T.qh-S	G(T)	qh-G(T)
Z	NO2	0	-973.20001	0.26617	-972.90436	-972.90857	0.09836	0.09197	-973.00272	-973.00054
Z	NO2	m20	-973.20188	0.26620	-972.90622	-972.91044	0.09844	0.09198	-973.00466	-973.00242
Z	NO2	m40	-973.20465	0.26622	-972.90899	-972.91320	0.09848	0.09199	-973.00747	-973.00520
Z	NO2	m60	-973.20835	0.26625	-972.91270	-972.91685	0.09798	0.09175	-973.01068	-973.00860
Z	NO2	m80	-973.21302	0.26621	-972.91742	-972.92157	0.09802	0.09177	-973.01545	-973.01334
Z	NO2	p20	-973.19903	0.26612	-972.90338	-972.90765	0.09841	0.09202	-973.00179	-972.99967
Z	NO2	p40	-973.19897	0.26598	-972.90338	-972.90765	0.09960	0.09262	-973.00298	-973.00027
Z	NO2	p60	-973.19995	0.26608	-972.90436	-972.90857	0.09804	0.09196	-973.00240	-973.00052
Z	NO2	p80	-973.20198	0.26585	-972.90651	-972.91078	0.09813	0.09209	-973.00464	-973.00287
E	NO2	0	-973.20518	0.26656	-972.90934	-972.91331	0.09667	0.09112	-973.00601	-973.00443
E	NO2	m20	-973.20680	0.26655	-972.91096	-972.91499	0.09665	0.09111	-973.00761	-973.00610
E	NO2	m40	-973.20940	0.26652	-972.91362	-972.91765	0.09660	0.09109	-973.01021	-973.00873
E	NO2	m60	-973.21300	0.26645	-972.91728	-972.92131	0.09668	0.09113	-973.01397	-973.01245
E	NO2	m80	-973.21767	0.26642	-972.92202	-972.92605	0.09661	0.09111	-973.01863	-973.01716
E	NO2	p20	-973.20449	0.26650	-972.90872	-972.91268	0.09672	0.09116	-973.00543	-973.00385
E	NO2	p40	-973.20473	0.26638	-972.90902	-972.91304	0.09703	0.09134	-973.00604	-973.00438
E	NO2	p60	-973.20588	0.26629	-972.91022	-972.91425	0.09714	0.09142	-973.00736	-973.00567
E	NO2	p80	-973.20793	0.26617	-972.91234	-972.91637	0.09720	0.09147	-973.00953	-973.00784

Table A.9: Thermodinamic Data for the Reaction Axis CH_3 Hurd-Nit rearrangement with OEEF magnitude of -8.00×10^{-3} to 8.00×10^{-3} a.u. All units are atomic units.

Iso	Sub	Field	E	ZPE	H	qh-H	T.S	T.qh-S	G(T)	qh-G(T)
Z	CH3	0	-402.01002	0.14080	-401.85444	-401.85514	0.05989	0.05944	-401.91433	-401.91458
Z	CH3	m20	-402.01062	0.14085	-401.85505	-401.85572	0.05979	0.05935	-401.91483	-401.91507
Z	CH3	m40	-402.01177	0.14090	-401.85616	-401.85684	0.05973	0.05929	-401.91589	-401.91613
Z	CH3	m60	-402.01346	0.14093	-401.85785	-401.85852	0.05967	0.05924	-401.91752	-401.91776
Z	CH3	m80	-402.01570	0.14095	-401.86010	-401.86077	0.05962	0.05919	-401.91972	-401.91996
Z	CH3	p20	-402.00992	0.14076	-401.85440	-401.85507	0.05986	0.05943	-401.91426	-401.91450
Z	CH3	p40	-402.01036	0.14069	-401.85487	-401.85554	0.05988	0.05946	-401.91475	-401.91500
Z	CH3	p60	-402.01132	0.14061	-401.85589	-401.85656	0.05992	0.05950	-401.91581	-401.91606
Z	CH3	p80	-402.01280	0.14050	-401.85744	-401.85811	0.05998	0.05957	-401.91741	-401.91768
E	CH3	0	-402.00646	0.14107	-401.85076	-401.85137	0.05945	0.05907	-401.91021	-401.91044
E	CH3	m20	-402.00690	0.14111	-401.85120	-401.85178	0.05937	0.05900	-401.91057	-401.91078
E	CH3	m40	-402.00787	0.14114	-401.85214	-401.85275	0.05935	0.05898	-401.91149	-401.91173
E	CH3	m60	-402.00937	0.14114	-401.85367	-401.85428	0.05934	0.05896	-401.91302	-401.91325
E	CH3	m80	-402.01142	0.14112	-401.85572	-401.85636	0.05936	0.05897	-401.91507	-401.91532
E	CH3	p20	-402.00652	0.14101	-401.85085	-401.85149	0.05947	0.05910	-401.91032	-401.91059
E	CH3	p40	-402.00709	0.14094	-401.85148	-401.85210	0.05953	0.05915	-401.91101	-401.91125
E	CH3	p60	-402.00817	0.14085	-401.85263	-401.85324	0.05958	0.05921	-401.91220	-401.91244
E	CH3	p80	-402.00976	0.14075	-401.85428	-401.85488	0.05963	0.05927	-401.91391	-401.91416

Table A.10: Thermodinamic Data for the Reaction Axis Et Hurd-Nit rearrangement with OEEF magnitude of -8.00×10^{-3} to 8.00×10^{-3} a.u. All units are atomic units.

Iso	Sub	Field	E	ZPE	H	qh-H	T.S	T.qh-S	G(T)	qh-G(T)
Z	Et	0	-441.31439	0.16880	-441.12872	-441.13009	0.06636	0.06434	-441.19508	-441.19443
Z	Et	m20	-441.31543	0.16896	-441.12974	-441.13102	0.06491	0.06365	-441.19464	-441.19467
Z	Et	m40	-441.31717	0.16900	-441.13147	-441.13269	0.06458	0.06356	-441.19605	-441.19624
Z	Et	m60	-441.31950	0.16903	-441.13383	-441.13496	0.06433	0.06346	-441.19816	-441.19842
Z	Et	m80	-441.32248	0.16900	-441.13681	-441.13800	0.06444	0.06351	-441.20125	-441.20152
Z	Et	p20	-441.31428	0.16887	-441.12865	-441.12990	0.06498	0.06371	-441.19363	-441.19360
Z	Et	p40	-441.31488	0.16885	-441.12930	-441.13046	0.06462	0.06355	-441.19392	-441.19401
Z	Et	p60	-441.31613	0.16880	-441.13062	-441.13175	0.06460	0.06351	-441.19521	-441.19526
Z	Et	p80	-441.31805	0.16870	-441.13262	-441.13375	0.06473	0.06357	-441.19735	-441.19732
E	Et	0	-441.31472	0.16885	-441.12921	-441.13037	0.06456	0.06358	-441.19377	-441.19395
E	Et	m20	-441.31514	0.16890	-441.12960	-441.13072	0.06440	0.06349	-441.19400	-441.19422
E	Et	m40	-441.31614	0.16892	-441.13059	-441.13172	0.06441	0.06349	-441.19500	-441.19522
E	Et	m60	-441.31770	0.16892	-441.13216	-441.13328	0.06441	0.06349	-441.19656	-441.19678
E	Et	m80	-441.31985	0.16887	-441.13437	-441.13553	0.06448	0.06352	-441.19884	-441.19905
E	Et	p20	-441.31484	0.16880	-441.12936	-441.13052	0.06457	0.06360	-441.19392	-441.19412
E	Et	p40	-441.31551	0.16874	-441.13006	-441.13122	0.06458	0.06364	-441.19464	-441.19485
E	Et	p60	-441.31671	0.16867	-441.13132	-441.13244	0.06455	0.06365	-441.19587	-441.19610
E	Et	p80	-441.31847	0.16856	-441.13313	-441.13426	0.06466	0.06375	-441.19779	-441.19802

Table A.11: Thermodinamic Data for the Reaction Axis *SProp* Hurd-Nit rearrangement with OEEF magnitude of -8.00×10^{-3} to 8.00×10^{-3} a.u. All units are atomic units.

Iso	Sub	Field	E	ZPE	H	qh-H	T.S	T.qh-S	G(T)	qh-G(T)
E	SProp	0	-480.62455	0.19627	-480.40952	-480.41092	0.06900	0.06773	-480.47852	-480.47866
E	SProp	m20	-480.62500	0.19628	-480.40997	-480.41137	0.06901	0.06772	-480.47898	-480.47909
E	SProp	m40	-480.62614	0.19627	-480.41115	-480.41255	0.06900	0.06770	-480.48015	-480.48024
E	SProp	m60	-480.62801	0.19623	-480.41304	-480.41448	0.06905	0.06770	-480.48209	-480.48217
E	SProp	m80	-480.63063	0.19615	-480.41572	-480.41719	0.06922	0.06777	-480.48494	-480.48496
E	SProp	p20	-480.62476	0.19622	-480.40977	-480.41117	0.06898	0.06775	-480.47874	-480.47892
E	SProp	p40	-480.62564	0.19615	-480.41070	-480.41208	0.06901	0.06781	-480.47972	-480.47988
E	SProp	p60	-480.62716	0.19607	-480.41225	-480.41363	0.06904	0.06787	-480.48130	-480.48150
E	SProp	p80	-480.62931	0.19597	-480.41450	-480.41584	0.06908	0.06794	-480.48358	-480.48378
Z	SProp	0	-480.62414	0.19620	-480.40908	-480.41051	0.06939	0.06794	-480.47847	-480.47846
Z	SProp	m20	-480.62514	0.19624	-480.41008	-480.41152	0.06918	0.06781	-480.47927	-480.47933
Z	SProp	m40	-480.62680	0.19624	-480.41177	-480.41320	0.06911	0.06778	-480.48088	-480.48099
Z	SProp	m60	-480.62908	0.19622	-480.41409	-480.41552	0.06897	0.06770	-480.48306	-480.48322
Z	SProp	m80	-480.63205	0.19619	-480.41709	-480.41852	0.06901	0.06772	-480.48609	-480.48624
Z	SProp	p20	-480.62379	0.19616	-480.40876	-480.41020	0.06957	0.06803	-480.47834	-480.47823
Z	SProp	p40	-480.62434	0.19610	-480.40931	-480.41072	0.07001	0.06828	-480.47932	-480.47899
Z	SProp	p60	-480.62592	0.19616	-480.41092	-480.41224	0.06928	0.06788	-480.48020	-480.48012
Z	SProp	p80	-480.62825	0.19611	-480.41332	-480.41463	0.06926	0.06785	-480.48258	-480.48248

Table A.12: Thermodinamic Data for the Reaction Axis *Tbut* Hurd-Nit rearrangement with OEEF magnitude of -8.00×10^{-3} to 8.00×10^{-3} a.u. All units are atomic units.

Iso	Sub	Field	E	ZPE	H	qh-H	T.S	T.qh-S	G(T)	qh-G(T)
Z	TBut	0	-519.93498	0.22338	-519.69072	-519.69212	0.07294	0.07168	-519.76366	-519.76380
Z	TBut	m20	-519.93586	0.22343	-519.69160	-519.69294	0.07274	0.07158	-519.76433	-519.76452
Z	TBut	m40	-519.93743	0.22347	-519.69317	-519.69445	0.07246	0.07143	-519.76563	-519.76588
Z	TBut	m60	-519.93974	0.22346	-519.69548	-519.69682	0.07246	0.07144	-519.76794	-519.76826
Z	TBut	m80	-519.94275	0.22347	-519.69855	-519.69977	0.07235	0.07137	-519.77090	-519.77114
Z	TBut	p20	-519.93484	0.22329	-519.69064	-519.69204	0.07319	0.07179	-519.76383	-519.76383
Z	TBut	p40	-519.93552	0.22317	-519.69138	-519.69278	0.07357	0.07199	-519.76494	-519.76477
Z	TBut	p60	-519.93719	0.22316	-519.69305	-519.69445	0.07346	0.07193	-519.76651	-519.76638
Z	TBut	p80	-519.93977	0.22314	-519.69569	-519.69703	0.07341	0.07190	-519.76910	-519.76893
E	TBut	0	-519.92884	0.22392	-519.68434	-519.68574	0.07236	0.07100	-519.75670	-519.75674
E	TBut	m20	-519.92991	0.22393	-519.68540	-519.68681	0.07231	0.07094	-519.75771	-519.75775
E	TBut	m40	-519.93175	0.22389	-519.68731	-519.68871	0.07239	0.07096	-519.75970	-519.75967
E	TBut	m60	-519.93441	0.22377	-519.69003	-519.69156	0.07267	0.07107	-519.76270	-519.76263
E	TBut	m80	-519.93888	0.22427	-519.69419	-519.69578	0.07246	0.07076	-519.76665	-519.76654
E	TBut	p20	-519.92854	0.22388	-519.68404	-519.68544	0.07242	0.07105	-519.75645	-519.75649
E	TBut	p40	-519.92898	0.22377	-519.68454	-519.68594	0.07255	0.07116	-519.75709	-519.75710
E	TBut	p60	-519.93017	0.22364	-519.68578	-519.68719	0.07275	0.07132	-519.75854	-519.75851
E	TBut	p80	-519.93209	0.22346	-519.68782	-519.68923	0.07291	0.07146	-519.76073	-519.76068

Table A.13: Thermodinamic Data for the Reaction Axis *IsoBut* Hurd-Nit rearrangement with OEEF magnitude of -8.00×10^{-3} to 8.00×10^{-3} a.u. All units are atomic units.

Iso	Sub	Field	E	ZPE	H	qh-H	T.S	T.qh-S	G(T)	qh-G(T)
E	IsoBut	0	-519.93042	0.22400	-519.68573	-519.68756	0.07376	0.07187	-519.75949	-519.75943
E	IsoBut	m20	-519.93080	0.22396	-519.68610	-519.68800	0.07396	0.07195	-519.76007	-519.75995
E	IsoBut	m40	-519.93195	0.22391	-519.68732	-519.68922	0.07452	0.07220	-519.76184	-519.76141
E	IsoBut	p20	-519.93075	0.22399	-519.68606	-519.68789	0.07366	0.07182	-519.75972	-519.75972
E	IsoBut	p40	-519.93177	0.22394	-519.68714	-519.68897	0.07364	0.07183	-519.76078	-519.76081
E	IsoBut	p60	-519.93346	0.22388	-519.68890	-519.69067	0.07361	0.07184	-519.76250	-519.76251
E	IsoBut	p80	-519.93582	0.22378	-519.69131	-519.69308	0.07358	0.07186	-519.76488	-519.76494
Z	IsoBut	0	-519.93584	0.22394	-519.69109	-519.69304	0.07426	0.07219	-519.76535	-519.76524
Z	IsoBut	m20	-519.93639	0.22401	-519.69158	-519.69353	0.07407	0.07211	-519.76565	-519.76564
Z	IsoBut	m40	-519.93769	0.22404	-519.69288	-519.69483	0.07398	0.07206	-519.76686	-519.76689
Z	IsoBut	m60	-519.93976	0.22405	-519.69495	-519.69684	0.07391	0.07203	-519.76886	-519.76887
Z	IsoBut	m80	-519.94259	0.22405	-519.69784	-519.69967	0.07382	0.07199	-519.77167	-519.77166
Z	IsoBut	p20	-519.93605	0.22387	-519.69130	-519.69331	0.07442	0.07226	-519.76572	-519.76558
Z	IsoBut	p40	-519.93703	0.22382	-519.69234	-519.69436	0.07454	0.07232	-519.76688	-519.76668
Z	IsoBut	p60	-519.93881	0.22370	-519.69418	-519.69626	0.07487	0.07249	-519.76905	-519.76875
Z	IsoBut	p80	-519.94143	0.22350	-519.69692	-519.69900	0.07560	0.07290	-519.77252	-519.77190

Table A.14: Thermodinamic Data for the Reaction Axis *Ph* Hurd-Nit rearrangement with OEEF magnitude of -8.00×10^{-3} to 8.00×10^{-3} a.u. All units are atomic units.

Iso	Sub	Field	E	ZPE	H	qh-H	T.S	T.qh-S	G(T)	qh-G(T)
E	Ph	0	-593.73719	0.19290	-593.52472	-593.52637	0.07176	0.06995	-593.59648	-593.59632
E	Ph	m20	-593.73775	0.19294	-593.52523	-593.52694	0.07171	0.06990	-593.59693	-593.59684
E	Ph	m40	-593.73911	0.19291	-593.52665	-593.52836	0.07172	0.06989	-593.59836	-593.59825
E	Ph	m60	-593.74129	0.19287	-593.52889	-593.53060	0.07176	0.06990	-593.60065	-593.60050
E	Ph	m80	-593.74435	0.19283	-593.53195	-593.53366	0.07179	0.06990	-593.60374	-593.60356
E	Ph	p20	-593.73737	0.19282	-593.52491	-593.52662	0.07183	0.07001	-593.59674	-593.59663
E	Ph	p40	-593.73830	0.19272	-593.52590	-593.52761	0.07189	0.07008	-593.59779	-593.59769
E	Ph	p60	-593.73996	0.19266	-593.52761	-593.52932	0.07192	0.07013	-593.59954	-593.59945
E	Ph	p80	-593.74233	0.19259	-593.53005	-593.53170	0.07196	0.07018	-593.60200	-593.60188
Z	Ph	0	-593.73736	0.19253	-593.52502	-593.52685	0.07244	0.07047	-593.59747	-593.59732
Z	Ph	m20	-593.73805	0.19255	-593.52577	-593.52754	0.07229	0.07037	-593.59806	-593.59790
Z	Ph	m40	-593.73954	0.19254	-593.52726	-593.52910	0.07240	0.07037	-593.59966	-593.59947
Z	Ph	m60	-593.74184	0.19250	-593.52956	-593.53145	0.07258	0.07041	-593.60214	-593.60186
Z	Ph	m80	-593.74502	0.19245	-593.53280	-593.53470	0.07312	0.07060	-593.60592	-593.60530
Z	Ph	p20	-593.73744	0.19252	-593.52510	-593.52693	0.07249	0.07051	-593.59758	-593.59744
Z	Ph	p40	-593.73832	0.19244	-593.52604	-593.52787	0.07268	0.07064	-593.59872	-593.59851
Z	Ph	p60	-593.74001	0.19236	-593.52772	-593.52956	0.07303	0.07085	-593.60076	-593.60040
Z	Ph	p80	-593.74258	0.19227	-593.53036	-593.53220	0.07365	0.07120	-593.60402	-593.60340

Table A.15: Thermodinamic Data for the Reaction Axis NH_2Ph Hurd-Nit rearrangement with OEEF magnitude of -8.00×10^{-3} to 8.00×10^{-3} a.u. All units are atomic units.

Iso	Sub	Field	E	ZPE	H	qh-H	T.S	T.qh-S	G(T)	qh-G(T)
E	NH2	0	-649.10008	0.20894	-648.86918	-648.87114	0.07668	0.07455	-648.94587	-648.94568
E	NH2	m20	-649.09980	0.20893	-648.86891	-648.87086	0.07673	0.07457	-648.94564	-648.94543
E	NH2	m40	-649.10042	0.20902	-648.86952	-648.87142	0.07655	0.07441	-648.94608	-648.94583
E	NH2	m60	-649.10199	0.20888	-648.87116	-648.87311	0.07688	0.07465	-648.94803	-648.94776
E	NH2	m80	-649.10457	0.20884	-648.87380	-648.87575	0.07697	0.07471	-648.95076	-648.95046
E	NH2	p20	-649.10119	0.20894	-648.87030	-648.87225	0.07665	0.07454	-648.94695	-648.94680
E	NH2	p40	-649.10314	0.20894	-648.87224	-648.87413	0.07665	0.07457	-648.94889	-648.94871
E	NH2	p60	-649.10589	0.20890	-648.87500	-648.87695	0.07672	0.07462	-648.95171	-648.95157
E	NH2	p80	-649.10945	0.20881	-648.87862	-648.88057	0.07682	0.07470	-648.95544	-648.95527
Z	NH2	0	-649.10029	0.20855	-648.86958	-648.87165	0.07749	0.07512	-648.94707	-648.94678
Z	NH2	m20	-649.10003	0.20848	-648.86938	-648.87146	0.07752	0.07517	-648.94690	-648.94662
Z	NH2	m40	-649.10071	0.20841	-648.87006	-648.87219	0.07756	0.07518	-648.94762	-648.94737
Z	NH2	m60	-649.10233	0.20838	-648.87174	-648.87381	0.07767	0.07521	-648.94941	-648.94902
Z	NH2	m80	-649.10492	0.20824	-648.87445	-648.87659	0.07815	0.07538	-648.95260	-648.95197
Z	NH2	p20	-649.10150	0.20858	-648.87073	-648.87280	0.07759	0.07518	-648.94831	-648.94798
Z	NH2	p40	-649.10373	0.20861	-648.87296	-648.87497	0.07775	0.07527	-648.95071	-648.95024

Table A.16: Thermodinamic Data for the Reaction Axis NO_2Ph Hurd-Nit rearrangement with OEEF magnitude of -8.00×10^{-3} to 8.00×10^{-3} a.u. All units are atomic units.

Iso	Sub	Field	E	ZPE	H	qh-H	T.S	T.qh-S	G(T)	qh-G(T)
Z	NO2	0	-798.25187	0.19529	-798.03312	-798.03592	0.08245	0.07884	-798.11556	-798.11477
Z	NO2	m20	-798.25366	0.19528	-798.03490	-798.03771	0.08243	0.07880	-798.11734	-798.11651
Z	NO2	m40	-798.25632	0.19522	-798.03763	-798.04050	0.08269	0.07887	-798.12032	-798.11936
Z	NO2	p20	-798.25091	0.19525	-798.03216	-798.03497	0.08254	0.07892	-798.11470	-798.11389
Z	NO2	p40	-798.25076	0.19521	-798.03207	-798.03482	0.08265	0.07901	-798.11473	-798.11382
Z	NO2	p60	-798.25143	0.19508	-798.03281	-798.03555	0.08290	0.07916	-798.11571	-798.11472
Z	NO2	p80	-798.25296	0.19498	-798.03433	-798.03714	0.08330	0.07940	-798.11763	-798.11654
E	NO2	0	-798.25068	0.19555	-798.03187	-798.03449	0.08195	0.07844	-798.11382	-798.11294
E	NO2	m20	-798.25255	0.19554	-798.03374	-798.03642	0.08193	0.07843	-798.11567	-798.11486
E	NO2	m40	-798.25541	0.19549	-798.03666	-798.03935	0.08194	0.07843	-798.11860	-798.11778
E	NO2	m60	-798.25932	0.19547	-798.04057	-798.04332	0.08199	0.07845	-798.12256	-798.12176
E	NO2	m80	-798.26434	0.19541	-798.04565	-798.04840	0.08216	0.07853	-798.12781	-798.12693
E	NO2	p20	-798.24977	0.19550	-798.03096	-798.03364	0.08182	0.07840	-798.11278	-798.11205
E	NO2	p40	-798.24979	0.19544	-798.03104	-798.03367	0.08195	0.07848	-798.11299	-798.11215
E	NO2	p60	-798.25074	0.19541	-798.03199	-798.03461	0.08190	0.07848	-798.11389	-798.11308
E	NO2	p80	-798.25259	0.19532	-798.03390	-798.03653	0.08208	0.07858	-798.11599	-798.11511

A.4 Principal Contributions of the Thesis

This section summarizes the main contributions of the thesis. There were two publicantions, one 72 as the first author and another 19 as a contributor author. Both publications were made in international journals of relevance in the field of theoretical Chemistry. The first page of each article is included in this section. Additionally, as one of the main objectives of the thesis was the development of the python package `MoleKing`, the registration of the package under *Instituto Nacional de Propriedades Intelectuais* (INPI) was made, and is included in this section.

THE JOURNAL OF PHYSICAL CHEMISTRY A
A JOURNAL OF THE AMERICAN CHEMICAL SOCIETY

Theoretical Model of Polarization Effects on Third-Order NLO Properties of the Stilbazolium Derivative Crystal

Mateus R. Barbosa, Igor S. Duarte Costa, Thiago O. Lopes, Clodoaldo Valverde,
Daniel F. Scalabrini Machado,* and Heibbe Cristhian B. de Oliveira*

Cite This: J. Phys. Chem. A 2022, 126, 8901−8909

Read Online

ACCESS | Metrics & More | Article Recommendations | Supporting Information

ABSTRACT: The linear and nonlinear properties of the stilbazolium derivative, 2-[2-(3-hydroxy-4-methoxy-phenyl)-vinyl]-1-methyl-pyridinium naphthalene-2-sulfonate dihydrate crystal (VSNS), were investigated using an iterative electrostatic embedding scheme and density functional theory (DFT). The dipole moment and second hyperpolarizability of the VSNS molecule are sharply influenced by its crystalline phase. Standard DFT global hybrids such as B3LYP and M06 are strongly benefited by the effects of crystalline polarization. The performance can be further improved by making small changes in the amount of Hartree−Fock exchange included in the hybrid, delivering good hyperpolarizability and spectroscopy.

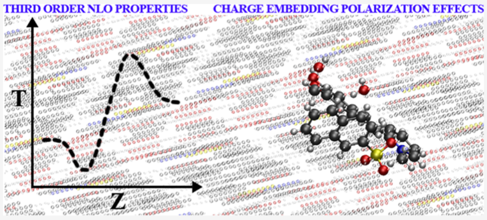

1. INTRODUCTION

Nonlinear optics (NLO) is the field of science devoted to studying the interactions of intense electromagnetic fields with matter. The outputs of these interactions are electromagnetic fields with a different frequency, phase, and polarization to those of the input field. Originally, the NLO targets were inorganic-based salts, but in modern applications, organic-based architectures are particularly interesting because of their idiosyncrasies such as an ultrafast response time (due to the delocalized nature of the π-extended electrons), photothermal stability, and greater synthetic flexibility.[1] As a result, these organic "NLO-phores" find potential applications in various technological domains including light emission transistors composed of charge-transfer polymers,[2] organic photodiodes for imaging,[3] photon microscopy,[4] second harmonic generation,[5] and two-photon absorption.[6]

Organic single crystals are now common when investigating new materials with broad applicability in the realm of NLO devices.[7] The π-electronic delocalization in, for example, aromatic fragments, of these organic NLO-phores, can give rise to specific strong noncovalent interactions such as π-stacking, thus greatly increasing their packing density and ultimately leading to large nonlinear responses.[7−9] One family of these organic crystals, which are highly studied, are the stilbazolium derivatives, mainly due to their good crystal growth, satisfactory performance in NLO, and crystal transparency in the vis−NIR region, in most cases, very desirable for applications in optoelectronics.[9−11] Therefore, theoretical approaches aiming at describing the electronic features responsible for good NLO properties of stilbazolium derivatives can be an invaluable tool both to predict and/or understand practical experimental investigations in the realm of NLO and photonics.

From a theoretical standpoint, the microscopic quantity related to the third-order NLO properties measured experimentally is the molecular second hyperpolarizability, γ, which measures the nonlinear distortion of the electronic distribution resulting from the perturbation of an external electric field. Single-molecule quantum-mechanical (QM) calculations may not generate results comparable to the experimentally observed quantities when the measurements are performed in condensed phases. In these cases, the explicit inclusion of the surrounding environment would benefit such calculations. However, this added complexity of the QM calculations has a high computational cost, meaning low-cost alternatives are imperative.

One such alternative has been successfully employed for molecular crystals, taking advantage of the periodicity of the molecular packing. It is the so-called self-consistent or iterative supermolecular point charge embedding scheme.[12−14] Using this iterative process, the effects of the polarized medium on the electrical properties of the molecular crystals are properly described. The point charge embedding approach is used to better simulate the crystal environment by generating the correct crystalline electrostatic Coulomb potential in the region with quantum-mechanical treatment. The electrostatic crystal potential that is experienced by each atom in a molecule in the infinite crystal lattice is simulated with a finite self-consistently derived array of point charges.[15] This polarization

Received: June 17, 2022
Revised: October 21, 2022
Published: November 28, 2022

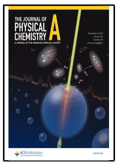

https://doi.org/10.1021/acs.jpca.2c04214
J. Phys. Chem. A 2022, 126, 8901−8909

ChemPhysChem

Research Article
doi.org/10.1002/cphc.202400565

Chemistry Europe
European Chemical Societies Publishing

www.chemphyschem.org

Deciphering Stereoselectivity in Hurd-Claisen Rearrangements: A Comprehensive Study of Electrostatic Interactions from Shubin's Energy Decomposition Analysis

Ana Gabriela Coelho Oliveira[+],[a] Mateus Rodrigues Barbosa[+],[a]
Pedro Henrique Ferreira Matias[+],[b] Charlley Anchieta Lourenço Silva[+],[b]
Daniel Francisco Scalabrini Machado[+],[b] Ângelo Henrique de Lira Machado[+],*[b] and
Heibbe Cristhian Benedito de Oliveira[+]*[a]

In this study, we explore the stereoselectivity of Hurd-Claisen Rearrangements, focusing on the influence of two electron-withdrawing groups and eight diverse substituents. Utilizing the Curtin-Hammett principle, we performed energy calculations for reactions, products, and transition states using the M062X/def2TZVPP compound model. Our analysis reveals that kinetic factors predominantly dictate the reaction equilibrium. A key aspect of our research is the application of Shubin's energy decomposition analysis to optimized transition states, highlighting the significant role of electrostatic interactions in determining stereoselectivity. We further dissected each transition state into four fragments: the electron-withdrawing groups (*CO_2Et*, *CN*), the Hurd group (*H*), various substituents (*CH_3*, *Et*, *SProp*, *TBut*, *IsoBut*, *NH_2Ph*, *NO_2Ph*, *Ph*), and the central fragment. This fragmentation approach enabled an in-depth analysis of group dipole moments, providing insights into the electrostatic forces at play. Our findings shed light on the intricate mechanisms driving stereoselectivity in Hurd-Claisen Rearrangements and enhance the understanding of molecular interactions, offering valuable implications for organic synthesis.

Introduction

The Claisen rearrangement is a powerful tool in organic synthesis to build new *C*–*C* bonds.[1–4] Due to the concerted pericyclic mechanism of this reaction, a new *C*=*C* bond is stereoselectively installed in the product. Its Hurd variant is a two-step reaction in which an allylic alcohol is converted *in situ* to its allyl enol ether, that sequentially rearranges to the product. Recently, we reported the unprecedented *E*-stereoselectivity on the Hurd-Claisen rearrangement of Morita–Baylis–Hillman (MBH) adducts prepared from aldehydes and alkyl acrylates.[5] To explore the scope of this stereoselective way of preparing trisubstituted *C*=*C* bonds, we employed the Hurd-Claisen reaction with the MBH adduct prepared from benzaldehyde and acrylonitrile. In contrast to the results obtained from the reaction with ester-containing adducts, the Hurd-Claisen with the nitrile-containing adduct yielded the rearrangement product in high stereoselectivity of *Z*/*E* = 99 : 1 (Scheme 1). Similar results have been reported to the Johnson-Claisen and the Eschenmoser-Claisen rearrangements of the nitrile-containing MBH adducts.[6,7] These results suggest that the origin of this change in the stereochemical outcome of the Claisen-like rearrangements of MBH adducts is closely related to structural properties of the electron-withdrawing group of the MBH adducts.

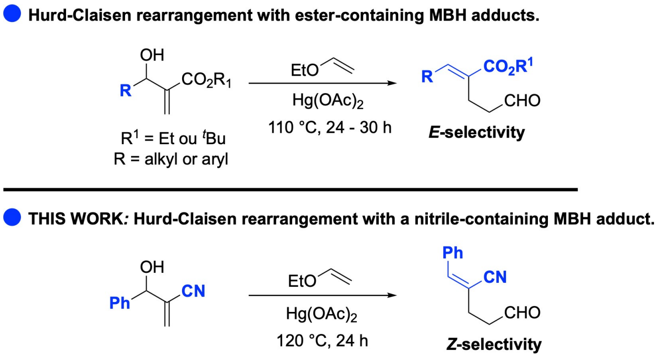

Scheme 1. Hurd-Claisen rearrangement of Morita–Baylis–Hillman (MBH) adducts.

It is critical to note that there is no significant influence of the catalyst, mercury acetate, on the diastereomeric TS's responsible for the formation of products in the Hurd-Claisen rearrangement of MBH adducts. This observation was assessed by adding excess metallic mercury to the reaction. Monitoring the reaction's progress revealed a curve consistent with the reaction trend observed in the absence of metallic mercury.[5] These observations suggest that, despite the Lewis base sites

---

[a] A. G. C. Oliveira,[+] M. R. Barbosa,[+] Dr. H. C. Benedito de Oliveira[+]
Laboratório de Estrutura Eletrônica e Dinâmica Molecular (LEEDMOL), Instituto de Química, Universidade Federal de Goiás, Campus Samambaia, 74690-900 – Goiânia, GO, Brazil
E-mail: heibbe@ufg.br

[b] P. H. F. Matias,[+] C. A. L. Silva,[+] Dr. D. F. S. Machado,[+]
Dr. Â. H. de Lira Machado[+]
Instituto de Química, Universidade de Brasília,
Campus Darcy Ribeiro, 70910-900 – Brasília, DF, Brazil
E-mail: nagelo@unb.br

[+] *These authors contributed equally.*

Supporting information for this article is available on the WWW under https://doi.org/10.1002/cphc.202400565

REPÚBLICA FEDERATIVA DO BRASIL
MINISTÉRIO DO DESENVOLVIMENTO, INDÚSTRIA, COMÉRCIO E SERVIÇOS
INSTITUTO NACIONAL DA PROPRIEDADE INDUSTRIAL
DIRETORIA DE PATENTES, PROGRAMAS DE COMPUTADOR E TOPOGRAFIAS DE CIRCUITOS

Certificado de Registro de Programa de Computador

Processo Nº: **BR512025001601-8**

O Instituto Nacional da Propriedade Industrial expede o presente certificado de registro de programa de computador, válido por 50 anos a partir de 1° de janeiro subsequente à data de 10/03/2025, em conformidade com o §2°, art. 2° da Lei 9.609, de 19 de Fevereiro de 1998.

Título: MoleKing: A Python Module for Theoretical Chemistry

Data de publicação: 10/03/2025

Data de criação: 07/02/2022

Titular(es): UNIVERSIDADE FEDERAL DE GOIÁS

Autor(es): MATEUS RODRIGUES BARBOSA; PEDRO HENRIQUE FERREIRA MATIAS; THIAGO OLIVEIRA LOPES; HEIBBE CRISTHIAN BENEDITO DE OLIVEIRA; RAFAEL FERREIRA VERISSIMO

Linguagem: C++; PYTHON

Campo de aplicação: CO-02; FQ-08

Tipo de programa: DS-05; DS-06; SM-01

Algoritmo hash: SHA-512

Resumo digital hash:
20abf90d4304bf51f6581bebe15afd7cf06810999efb4b69bf73b74d4e816f0cf40fc2f18639bfc39356c371bbb87c3cecd88aa09ce59d88c4ef1d2edbbbf7f6

Expedido em: 29/04/2025

Aprovado por:
Carlos Alexandre Fernandes Silva
Chefe da DIPTO

A.5 Parallel Contributions of the Thesis

During the development of the thesis, some parallel contributions were made. These contributions are not directly related to the main objectives of the thesis, but they are relevant in the field of theoretical Chemistry. Both contributions are publications 109 and 110 as a contributor author. The first page of each article is included in this section.

JCIM JOURNAL OF CHEMICAL INFORMATION AND MODELING

pubs.acs.org/jcim

Article

Integrating Machine Learning and SHAP Analysis to Advance the Rational Design of Benzothiadiazole Derivatives with Tailored Photophysical Properties

Rafael F. Veríssimo, Pedro H. F. Matias, Mateus R. Barbosa, Flávio O. S. Neto,* Brenno A. D. Neto, and Heibbe C. B. de Oliveira*

Cite This: https://doi.org/10.1021/acs.jcim.4c02414

Read Online

ACCESS | Metrics & More | Article Recommendations | Supporting Information

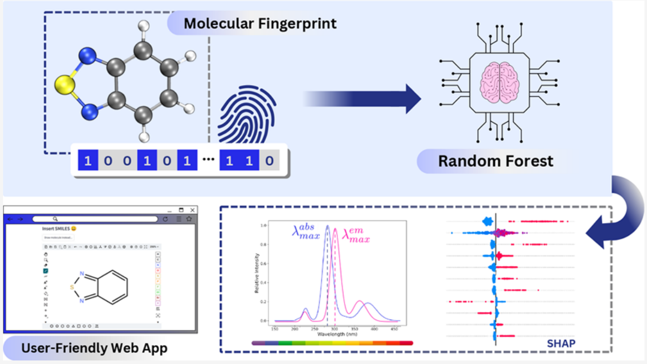

ABSTRACT: 2,1,3-Benzothiadiazole (BTD) derivatives show promise in advanced photophysical applications, but designing molecules with optimal desired properties remains challenging due to complex structure−property relationships. Existing computational methods have a high cost when predicting precise photophysical characteristics. Machine learning with Morgan fingerprints was employed to forecast BTD derivative maximum absorption and emission wavelengths. Three flavors of machine learning models were applied, namely, Random Forest, LigthGBM, and XGBoost. Random forest achieved R^2 values of 0.92 for absorption and 0.89 for emission, validated internally with 10-fold cross-validations and externally with recent experimental data. SHapley Additive exPlanations (SHAP) analysis revealed critical design insights, highlighting the tertiary amine presence and solvent polarity as key drivers of red-shifted emissions. By the development of a web-based predictive tool, the potential of machine learning to accelerate molecular design is demonstrated, providing researchers a powerful approach to engineer BTD derivatives with enhanced photophysical properties.

■ INTRODUCTION

2,1,3-Benzothiadiazole (BTD) derivatives have attracted significant attention due to their versatile photophysical properties and potential applications across various scientific and technological domains. These heterocyclic systems, featuring a fused thiadiazole ring and strong electron-withdrawing capacity,[1−3] have been widely explored in organic photovoltaics,[4] optoelectronics,[5] and as fluorescent probes in bioimaging,[6,7] among other applications (Figure 1). BTD-based fluorophores, known for their brightness,[8] large Stokes shifts,[9,10] and strong intramolecular charge transfer (ICT) interactions,[11−13] have demonstrated remarkable utility in fields where precise photophysical behavior is paramount. These derivatives often form ordered crystalline packings and can be tuned structurally to achieve the desired optical outputs. Such adaptability has led to their incorporation in devices requiring finely controlled emission spectra,[14] as well as their application in advanced fluorescence imaging, including the selective staining of mitochondria in cancer cell lines.[15−17]

Despite the promise of BTD analogues, identifying optimal candidates with target photophysical characteristics frequently relies on iterative synthetic efforts, extensive experimental screenings, or high-level computational chemistry. Traditional quantum chemical protocols, although insightful, can be expensive and time-consuming,[14,15] limiting their routine use for rapid compound discovery. This challenge is compounded by the subtle interplay of substituents, solvent polarity, and molecular conformation on the electronic transitions governing absorption and emission.[18] Consequently, there is a need for more accessible, efficient, and systematic strategies to predict photophysical properties without relying exclusively on expensive or specialized computational tools.

In recent years, machine learning (ML) methodologies have emerged as powerful alternatives for predicting molecular properties with reduced computational demands.[19] By leveraging large data sets and pattern recognition capabilities, ML models can correlate structural features with observed properties, bypassing the necessity for explicit quantum chemical descriptor calculations.[20,21] A particularly successful approach involves representing molecules through molecular fingerprints (e.g., Morgan or MACCS), which encode the presence or absence of specific substructures as binary

Received: January 14, 2025
Revised: March 27, 2025
Accepted: April 7, 2025

molecules

MDPI

Article

(Ro)vibrational Spectroscopic Constants, Lifetime and QTAIM Evaluation of Fullerene Dimers Stability

Rodrigo A. Lemos Silva [1,2], Mateus R. Barbosa [3], Caio R. Martins [2], Daniel F. Scalabrini Machado [4], Luciano Ribeiro [2,*], Heibbe C. B. de Oliveira [3,*] and Demétrio A. da Silva Filho [5]

[1] Instituto Federal de Educação, Ciência e Tecnologia de Goiás (IFG), Câmpus Jataí, Jataí 75804-714, GO, Brazil; rodrigo.aparecido@ifg.edu.br
[2] Grupo de Química Teórica e Estrutural de Anápolis (GQTEA), Campus Central Anápolis de Ciências Exatas e Tecnológicas Henrique Santillo, Universidade Estadual de Goiás, CP 459, Anápolis 75132-903, GO, Brazil; caiorodriguesmartins@hotmail.com
[3] Laboratório de Estrutura Eletrônica e Dinâmica Molecular (LEEDMOL), Instituto de Química, Universidade Federal de Goiás, CP 131, Goiânia 74001-970, GO, Brazil; mateusrodriguesbarbosa@gmail.com
[4] Laboratório de Modelagem Molecular de Sistemas Complexos (LMSC), Instituto de Química, Universidade de Brasília, CP 4478, Brasília 70919-970, DF, Brazil
[5] Grupo de Semicondutores Orgânicos, Instituto de Física, Campus Darcy Ribeiro, Universidade de Brasília, CP 4478, Brasília 70919-970, DF, Brazil; dasf@unb.br
* Correspondence: lribeiro@ueg.br (L.R.); heibbe@ufg.br (H.C.B.d.O.)

Abstract: The iconic caged shape of fullerenes gives rise to a series of unique chemical and physical properties; hence a deeper understanding of the attractive and repulsive forces between two buckyballs can bring detrimental information about the structural stability of such complexes, providing significant data applicable for several studies. The potential energy curves for the interaction of multiple van der Waals buckyball complexes with increasing mass were theoretically obtained within the DFT framework at ωB97xD/6−31G(d) compound model. These potential energy curves were employed to estimate the spectroscopic constants and the lifetime of the fullerene complexes with the Discrete Variable Representation and with the Dunham approaches. It was revealed that both methods are compatible in determining the rovibrational structure of the dimers and that they are genuinely stable, i.e., long-lived complexes. To further inquire into the nature of such interaction, Bader's QTAIM approach was applied. QTAIM descriptors indicate that the interactions of these closed-shell systems are dominated by weak van der Waals forces. This non-covalent interaction character was confirmed by the RDG analysis scheme. Indirectly, QTAIM also allowed us to confirm the stability of the non-covalent bonded fullerene dimers. Our lifetime calculations have shown that the studied dimers are stable for more than 1 ps, which increases accordingly with the number of carbon atoms.

Keywords: fullerene dimers; spectroscopic properties; Dunham; DVR; QTAIM; lifetime

check for updates

Citation: Lemos Silva, R.A.; Barbosa, M.R.; Martins, C.R.; Scalabrini Machado, D.F.; Ribeiro, L.; de Oliveira, H.C.B.; da Silva Filho, D.A. (Ro)vibrational Spectroscopic Constants, Lifetime and QTAIM Evaluation of Fullerene Dimers Stability. *Molecules* **2023**, *28*, 5023. https://doi.org/10.3390/molecules28135023

Academic Editor: Federico Totti

Received: 2 May 2023
Revised: 23 May 2023
Accepted: 25 May 2023
Published: 27 June 2023

1. Introduction

Fullerenes, also known as buckyballs, are hollow polyhedral molecules constituted of sp2-hybridized covalently bonded carbon atoms, with the faces made up of a combination between pentagons and hexagons [1–3]. They were originally predicted by Osawa in 1970 [1] and first synthesized in 1985 by Kroto and co-workers [2]. The iconic caged shape of buckyballs gives rise to interesting chemical properties, such as trapping small molecules inside fullerenes [4,5], organometallic fullerenes acting as hydrogen adsorbents [6], and endohedral doping with metals resulting in high electrical conductivity [7]. The unique physical and chemical properties of fullerenes attracted a lot of attention aimed at their possible applications to organic electronics. For example, as components of photovoltaic cells [8,9], for the development of sensors employed for the capture of pollutants [10,11], or for electron transport through self-assembled monolayers of functionalized fullerenes [12,13]. In